

**FIRST PRINCIPLES CALCULATIONS OF X-RAY
MEASUREMENTS ON SELECTED MATERIALS**



Nuchalee Schwertfager

A Thesis Submitted in Partial Fulfillment of the Requirements for the

Degree of Doctor of Philosophy in Physics

Suranaree University of Technology

Academic Year 2016

การคำนวณการวัดด้วยรังสีเอกซ์ของสารที่เลือกศึกษาโดยวิธีเฟสตัดพรินซิเพิล



วิทยานิพนธ์นี้เป็นส่วนหนึ่งของการศึกษาตามหลักสูตรปริญญาวิทยาศาสตรดุษฎีบัณฑิต

สาขาวิชาฟิสิกส์

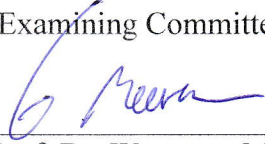
มหาวิทยาลัยเทคโนโลยีสุรนารี

ปีการศึกษา 2559

**FIRST PRINCIPLES CALCULATIONS OF X-RAY
MEASUREMENTS ON SELECTED MATERIALS**

Suranaree University of Technology has approved this thesis submitted in partial fulfillment of the requirements for the Degree of Doctor of Philosophy.

Thesis Examining Committee



(Asst. Prof. Dr. Worawat Meevasana)

Chairperson



(Prof. Dr. Sukit Limpijumnong)

Member (Thesis Advisor)



(Prof. Dr. Supa Hannongbua)

Member



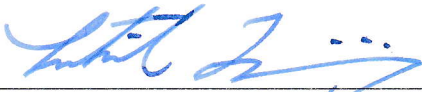
(Assoc. Prof. Dr. Sirichok Jungthawan)

Member



(Dr. Chanan Euaruksakul)

Member



(Prof. Dr. Sukit Limpijumnong)

Vice Rector of Academic Affairs
and Innovation



(Prof. Dr. Santi Maensiri)

Dean of Institute of Science

NUCHALEE SCHWERTFAGER : FIRST PRINCIPLES CALCULATIONS
OF X-RAY MEASUREMENTS ON SELECTED MATERIALS. THESIS
ADVISOR : PROF. SUKIT LIMPIJUMNONG, Ph.D. 101 PP.

XANES/RXES/FIRST PRINCIPLES CALCULATION/ELECTRONIC BAND
STRUCTURE/GRAPHENE/INDIUM NITRIDE/ $\text{Bi}(\text{Mg}_{0.5}\text{Ti}_{0.5})\text{O}_3$

Synchrotron light source is the origin of various highly effective x-ray techniques for studying properties of materials. This thesis involves two well-known techniques including RXES which is highly appropriate for studying electronic band structures of materials and XANES technique which is widely used for probing physical properties of materials. However, the experiments alone are generally not sufficient to gain a deep understanding of material properties. Therefore, in this thesis first principle calculation, which is unbiased and well accepted, is employed to help gaining a deeper and more accurate understanding of material properties. Three materials were chosen as follows. 1) Graphene, its electronic band structures were calculated along with RXES spectra employing first principle calculation as implemented in the FP-LMTO code. The calculated spectra were analyzed and compared with the experiments. The corehole effects on the spectra shifting were also taken into account for more accurate analysis, which has never been done before. Good agreements between the calculation and the experiment were obtained. 2) Indium Nitride, its electronic band structures were calculated with first principles calculation based on QSGW approximation as implemented in FP-LMTO code. The calculated band gap was highly accurate and agree well with previous experiment. The RXES

spectra were calculated at near grazing and near normal angles of incidence in order to probe different parts of the electronic band structures. The calculated spectra were compared to the experimental ones and help to explain the electronic band structure of this material in more detailed. 3) $\text{Bi}(\text{Mg}_{0.5}\text{Ti}_{0.5})\text{O}_3$, first principles calculation as implemented in VASP was employed to find the actual structure of this material and XANES spectra for the possible structures were calculated with FEFF code in order to find the cation off-centering features in the spectra. The results can be used to determine the actual structure of the material for the future experiments. In summary, first principles calculation is a very powerful method to be used to study the electronic band structure and physical structure of materials. The RXES technique is suitable to study electronic band structure, while XANES is good for the study of local structure of materials. When first principles calculation is used incorporated with the X-ray techniques, a much deeper understanding of materials can be obtained which is crucial to the development of better materials for electronic devices.

School of Physics

Academic Year 2016

Student's Signature _____

Advisor's Signature _____

นุชลี ชวีร์ตเฟเกอร์ : การคำนวณการวัดด้วยรังสีเอ็กซ์ของสารที่เลือกศึกษาโดยวิธีเฟิสต์
พริન્ซิเพิล (FIRST PRINCIPLES CALCULATIONS OF X-RAY MEASUREMENTS ON
SELECTED MATERIALS) อาจารย์ที่ปรึกษา : ศาสตราจารย์ ดร.ชูกิจ ลิมปิจำนงค์,
101 หน้า

เครื่องกำเนิดแสงซินโครตรอนนับว่าเป็นแหล่งกำเนิดของเทคนิคเอ็กซ์เรย์ ที่มีประสิทธิภาพ
ในการศึกษาคุณสมบัติของสารมากมาย โดยในวิทยานิพนธ์นี้ ได้มีการศึกษาเกี่ยวข้องกับเทคนิคสอง
ชนิด คือ RXES ซึ่งมีประสิทธิภาพสูงในการศึกษาแถบอิเล็กทรอนิกส์ของสารและ XANES ซึ่งใช้
ในการศึกษาโครงสร้างทางกายภาพของสาร อย่างไรก็ตาม การทดลองเพียงอย่างเดียวไม่สามารถทำ
ให้เกิดความเข้าใจในเชิงลึกในสารที่ศึกษาได้ดีเท่าที่ควร ในวิทยานิพนธ์นี้การคำนวณแบบเฟิร์สพริ
นซิเพิลซึ่งมีความแม่นยำและเป็นที่ยอมรับอย่างดีมาช่วยในการทำความเข้าใจคุณสมบัติของสารให้
แม่นยำและลึกซึ้งมากขึ้น โดยได้เลือกศึกษาสาร 3 ชนิด ดังนี้ 1) กราฟีน คำนวณแถบอิเล็กทรอนิกส์
ด้วยวิธีเฟิร์สพรินซิเพิลพร้อมทั้งคำนวณสเปกตรัม RXES ด้วยโปรแกรมที่ถูกสร้างไว้ใน FP-LMTO
ตลอดจนวิเคราะห์เปรียบเทียบกับผลการทดลองโดยมีการนำเสนอวิธีการพิจารณาผลของที่ว่างที่เกิด
ขึ้นในชั้นพลังงานต่ำสุด ที่มีต่อการเลื่อนตำแหน่งของสเปกตรัม RXES เพื่อการเปรียบเทียบที่แม่นยำ
ซึ่งไม่เคยมีใครทำมาก่อน ผลการคำนวณและผลการทดลองตรงกันอย่างมาก 2) อินเดียมไนไตรด์
คำนวณแถบอิเล็กทรอนิกส์ด้วยวิธีเฟิร์ส พรินซิเพิลและใช้การประมาณแบบ QSGW ซึ่งได้ถูกสร้าง
ไว้ในโปรแกรม FP-LMTO ซึ่งทำให้ได้ค่าช่องว่างระหว่างแถบพลังงานที่แม่นยำใกล้เคียงกับผลการ
ทดลอง พร้อมทั้งคำนวณสเปกตรัม RXES ที่มุมตกกระทบเกือบขนานและเกือบตั้งฉากกับระนาบ
ของผลึก เพื่อที่จะศึกษาแถบพลังงานที่ต่างกันแถบอิเล็กทรอนิกส์ของสาร ผลการคำนวณได้ถูก
นำไปเปรียบเทียบกับผลการทดลอง และทำให้สามารถอธิบายแถบอิเล็กทรอนิกส์ของสารนี้ได้ชัดเจน
มากขึ้น 3) $\text{Bi}(\text{Mg}_{0.5}\text{Ti}_{0.5})\text{O}_3$ โดยสารนี้ได้ใช้การคำนวณแบบเฟิร์ส พรินซิเพิลด้วย VASP เพื่อ
คำนวณหาโครงสร้างที่น่าจะเป็นของสารและทำการคำนวณสเปกตรัม XANES ของสารด้วยชุด
โปรแกรม FEFF เพื่อศึกษาลักษณะของสเปกตรัมที่เป็นตัวบ่งชี้ถึงการเลื่อนออกจากศูนย์กลางของ
ไอออนบวกในสารนี้ ซึ่งจะสามารถใช้เป็นแนวทางในการตรวจสอบโครงสร้างที่แท้จริงของสาร
ด้วยการทดลองวัดสเปกตรัม XANES ในอนาคต โดยสรุป การคำนวณแบบเฟิร์สพรินซิเพิลเป็น
เทคนิคที่มีประสิทธิภาพสูงในการคำนวณโครงสร้างอิเล็กทรอนิกส์และคุณสมบัติเชิงกายภาพของ
สาร เทคนิค RXES เป็นเทคนิคที่เหมาะสมสำหรับใช้ในการศึกษาโครงสร้างอิเล็กทรอนิกส์ของสาร
ในขณะที่เทคนิค XANES เหมาะสำหรับการศึกษาโครงสร้างทางกายภาพของสาร การคำนวณแบบ
เฟิร์สพรินซิเพิลร่วมกับการทดลองด้วยเทคนิคเอ็กซ์เรย์จะสามารถทำให้เกิดความเข้าใจในสารนั้นๆ

ที่ลึกซึ้งยิ่งขึ้น ซึ่งนับว่ามีความสำคัญอย่างยิ่งต่อการพัฒนาวัสดุที่ดีขึ้นสำหรับอุปกรณ์อิเล็กทรอนิกส์



สาขาวิชาฟิสิกส์
ปีการศึกษา 2559

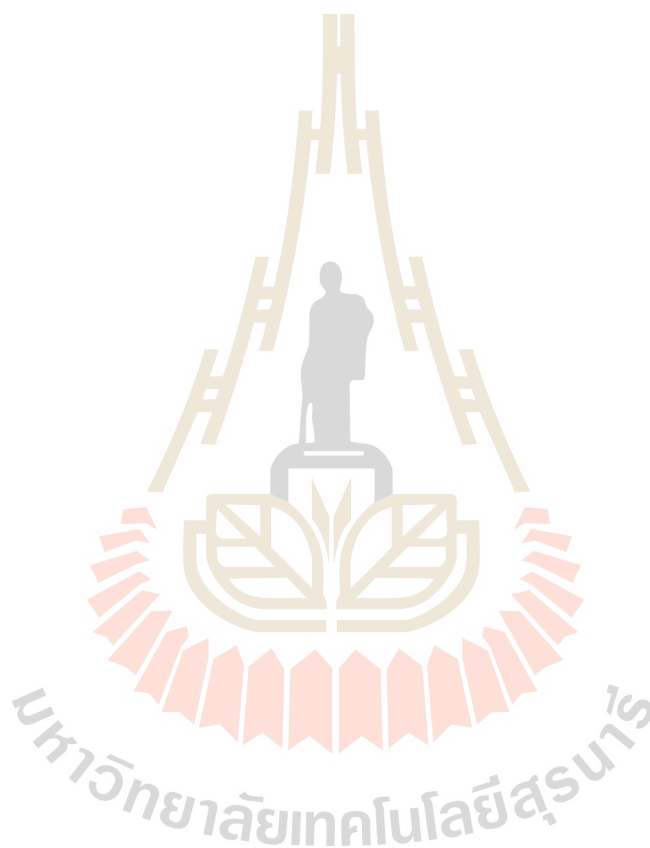
ลายมือชื่อนักศึกษา _____
ลายมือชื่ออาจารย์ที่ปรึกษา _____

ACKNOWLEDGEMENTS

This thesis could have not been completed without the help and support of many people and organizations. First of all, I would like to express my appreciation to my thesis advisor, Prof. Sukit Limpijumnong, and my thesis co-advisor, Prof. Walter Lambrecht, for their kind mentorship during my entire program - for guiding and supporting me throughout my PhD. experience. I would like to thank our collaborators, Dr. Malliga Suewattana, Dr. Lizeng Zhang, Dr. Jinghua Guo, and Assoc. Prof. Louis Piper for providing me with all of the needed experimental data, and for their fruitful collaborations over many years. I would like to thank the thesis committee for all of their fruitful discussions, reviews, and comments which helped me to finalize my thesis. I am very grateful to the SUT physics department, and SUT physics faculty members for providing me physics knowledge, useful discussions, and a motivated learning environment. I would like to thank all of SUT physics graduate students for giving me wonderful, and memorable friendships, support, and experiences while at SUT, all the members of SUT-CMT research group for all their help, discussions, friendships, and support throughout the years. I would like to thank Dr. Adisak Boonchun, Dr. Tawinan Chiewcharnchamnanakit, and Dr. Atchara Punya for all their help and support during my research visit at Case Western Reserve University, and through-out my PhD. program. I would like to acknowledge the Thailand Research Fund (TRF) for the financial support through the Royal Golden Jubilee PhD. Program (PHD/0089/2551), Suranaree University of Technology (SUT), and Synchrotron Light Research Institute for providing me with necessary resources during my studies. I would like to greatly thank my husband for his belief in me, and his encouragement and support throughout the hardship of completing this PhD. program. I would like to give thanks to both of our families for their

loving support, encouragement, and belief in the values of my education. Last, but not the least, I would like to devote part of this thesis to the memory of my beloved mother who raised me to become whom I am today, and to see the importance of education throughout ones' entire life.

Nuchalee Schwertfager



CONTENTS

	Page
ABSTRACT IN THAI	I
ABSTRACT IN ENGLISH.....	III
ACKNOWLEDGEMENTS	V
CONTENTS	VII
LIST OF FIGURES.....	X
LIST OF ABBREVIATIONS.....	XII
CHAPTER	
I INTRODUCTION	1
1.1 Overview of the calculation approaches.....	1
1.2 Research objectives.....	2
1.3 Scope and limitation of the study.....	2
II BASIC THEORIES OF X-RAY TECHNIQUES.....	4
2.1 X-Ray absorption near edge structure.....	4
2.1.1 Basic principle of x-ray absorption	4
2.1.2 Absorption fine structure.....	5
2.1.3 Multiple scattering theory and XANES	8
2.2 Resonant X-Ray Emission Spectroscopy.....	12
2.2.1 Introduction	12
2.2.2 Theory of resonant x-ray emission spectroscopy.....	14
2.2.3 Extracting band structure information from RXES experiments.....	17
2.2.4 RXES experiments	20

CONTENTS (Continued)

	Page
2.2.5 Angular dependence and experimental geometry.....	22
III CALCULATION METHODS	26
3.1 First - Principles calculation.....	26
3.2 Density functional theory (DFT).....	27
3.2.1 Local Density Approximation (LDA).....	29
3.2.2 Generalized Gradient Approximation (GGA).....	30
3.3 GW Approximation (GWA).....	31
3.2.1 Green's function.....	31
3.2.2 GW correction to LDA energy.....	34
3.4 Quasiparticle Self-consistent GW Approximation (QSGW).....	36
3.5 Full-Potential Linear Muffin-Tin Orbital Method (FP-LMTO).....	37
3.6 Plane wave basis sets and Bloch's theorem.....	41
3.7 k-point sampling in VASP code.....	42
3.8 Pseudo potential in VASP code.....	42
3.9 The Hellmann-Feynman theorem.....	44
3.10 Electronic Ground State Calculations Implemented in VASP code.....	44
IV RXES OF GRAPHENE	47
4.1 Introduction.....	47
4.2 Experimental methods.....	49
4.3 Computational methods.....	49
4.4 Results and discussions.....	50
4.5 Conclusion.....	56

CONTENTS (Continued)

	Page
V	RXES OF INDIUM NITRIDE.....57
5.1	Introduction.....57
5.2	Experimental methods.....58
5.3	Computational methods.....58
5.4	Results and discussions.....59
5.4.1	Band structures and partial density of states (PDOS).....59
5.4.2	CRXES measurement and calculation.....62
5.4.3	Extracting band-structure information from CRXES.....70
5.5	Conclusion.....71
VI	XANES OF Bi(Mg_{0.5}Ti_{0.5})O₃72
6.1.	Introduction.....72
6.2	Calculation methods.....73
6.3	Results and discussion.....76
6.4	Conclusion.....82
VII	CONCLUSION.....83
	REFERENCES.....85
	APPENDICES.....96
	APPENDIX A PUBLICATIONS.....97
	APPENDIX B PRESENTATIONS.....99
	CURRICULUM VITAE.....101

LIST OF FIGURES

Figure		Page
2.1	a) Schematic of incident and transmitted X-ray beam and b) absorption Coefficient $\mu(E)$	5
2.2	a) Schematic of the absorption process and b) absorption coefficient $\mu(E)$ versus photon energy E including the fine structure above the edge divided into the XANES and EXAFS regions.....	6
2.3	Schematic showing the absorbing atom (yellow) and its first nearest Neighbors.....	7
2.4	Schematic Examples of scattering paths. Path 1 is a single scattering path. Paths 2 and 3 are examples of double scattering paths. Paths 4 and 5 are examples of triple scattering paths.....	11
2.5	Resonant x-ray emission spectroscopy. The first figure, the incoming x-ray with energy E_{in} excites a core electron into an empty valence state. The middle figure, explains the resonant elastic x-ray emission, the excited electron decays and emits the same amount of energy as the excited energy, $E_{out} = E_{in}$. The last figure on the right explains the resonant inelastic x-ray emission where the electron from a lower valence or core state decay and emits the energy less than the excited energy, $E_{out} < E_{in}$	14
2.6	Initial, intermediate and final state of an inelastic x-ray scattering process in a single electron picture.	15
2.7	Illustration of the connection between the band structure and the experimental RIXS spectrum.	18
2.8	RXES experimental geometry.	25

LIST OF FIGURES (Continued)

Figure	Page
3.1	A schematic plot between the pseudo potential and pseudo wave function with respect to the distance, r , from the ionic nucleus.47
3.2	Self consistency scheme used in the VASP codes51
4.1	XAS and XES spectra compared to theory.55
4.2	Carbon p-like PDOS in graphene; core-hole effect.56
4.3	Band structure and DOS of graphene.58
4.4	Coherent RXES spectra compared to theory.60
5.1	a) N - p_{xy} PDOS and Intensity map of the calculated band structure.66
5.1	b) N- p_z PDOS and Intensity map of the calculated band structure.66
5.2	Calculated and measured InN (0001) CRXES at (a) near normal (20 degree) and (b) near grazing (70 degree) incidence.68
5.3	a) Near-grazing incident x-ray is polarized in z' direction which is nearly parallel to z axis of the crystal while the emitted x-ray isn't filtered and hence has its polarization in $x'y'$ plane which is nearly perpendicular to z axis of the crystal. b) Near normal incident x-ray is polarized in y' direction which is nearly normal to z axis of the crystal.....70
5.4	a) Intensity map of the calculated band structures used for the interpretation of RXES near-grazing (NG) spectra.71
6.1	Structural models of BMT used in our calculation to calculate XANES spectra....81
6.2	Bi L_3 -edge XANES spectra of four different structural models of BMT.86
6.3	Ti K-edge XANES spectra of four different structural models of BMT.88
6.4	Mg K-edge XANES spectra of four different structural models of BMT.90

LIST OF ABBREVIATIONS

PX	Protein X-ray Diffraction Techniques
SAXS	Small Angle X-ray Scattering Technique
WAXS	Wide Angle X-ray Scattering technique
PES	Photoemission Spectroscopy
XAS	X-ray Absorption Spectroscopy
XANES	X-ray Absorption Near Edge Structure
EXAFS	X-ray Absorption Fine Structure
ARPES	Angle-Resolved Photoemission Spectroscopy
RXES	Resonant X-ray Emission Spectroscopy
CRXES	Coherent Resonant X-ray Emission Spectroscopy
BZ	Brillouin Zone
DFT	Density Functional Theory
VASP	Vienna Ab-initio Simulation Package
FP-LMTO	Full Potential – Linear Muffin-Tin Orbital Method
NRXES	Normal X-ray Emission Spectroscopy
RIXS	Resonant Inelastic X-ray Scattering
LAPW	Linearized Augmented Plane Wave
CB	Conduction Band
VB	Valence Band
LPDOS	Local Partial Density of States
PDOS	Partial Density of States
LDA	Local Density Approximation

LIST OF ABBREVIATIONS (Continued)

GGA	Generalized Gradient Approximation
QSGW	Quasiparticle Self-consistent GW Approximation
MTO	Muffin-Tin Orbital
KS	Kohn-Sham
US-PP	Ultra-Soft Pseudo Potentials Method
PAW	Projector Augmented Wave Method
PDOS	Partial Density of States
XES	X-Ray Emission Spectroscopy
WZ	Wurtzite
NN	Near Normal Incident
NG	Near Grazing Incident
BMT	$\text{Bi}(\text{Mg}_{0.5}\text{Ti}_{0.5})\text{O}_3$
XRD	X-Ray Diffraction

CHAPTER I

INTRODUCTION

1.1 Overview of the calculation approaches

Advanced light sources based on the synchrotron techniques generate full spectrum of x-ray with unprecedented high brilliance of up to billions fold of natural light sources. This makes several measurement techniques that probe the structures of materials possible. These include a wide range of popularly used x-ray techniques such as protein x-ray diffraction techniques (PX), small and wide angle x-ray scattering techniques (SAXS & WAXS), photoelectron spectroscopy (PES), x-ray absorption spectroscopy (XAS), angle-resolved photoemission spectroscopy (ARPES), and resonant x-ray emission spectroscopy (RXES). These techniques are well suited for different scales, systems and the properties of interest. However, interpreting the results from the real materials to try to understand their properties can be difficult. First principle or “ab initio” calculation can be an effective method to solve the issue. First principles calculations are based on quantum level calculations of the electronic structures and density functional theory (J. Als-Nielsen, 2001) which allow one to model materials without taking any information from the measurements except the fundamental information about each element, i.e., the number of protons and electrons. Hence, the approach is highly unbiased. In our studies of selected crystalline compounds, we will focus our attentions on the XAS and RXES techniques. Note that we will not focus on the measurement as part of the graduation but rather focus on the computations to predict or to interpret measured results, as well as, forming the frameworks to properly compare computational results with the experiments. Most of the measured

results shall be obtained from literatures or collaborators.

RXES technique is one of the powerful techniques to probe electronic band structure of materials while XAS is suitable tool for probing local structures of materials. This thesis work will use RXES to study perfect crystalline with interesting features in their electronic band structures and XAS to study the local structure of the selected material.

1.2 Research objectives

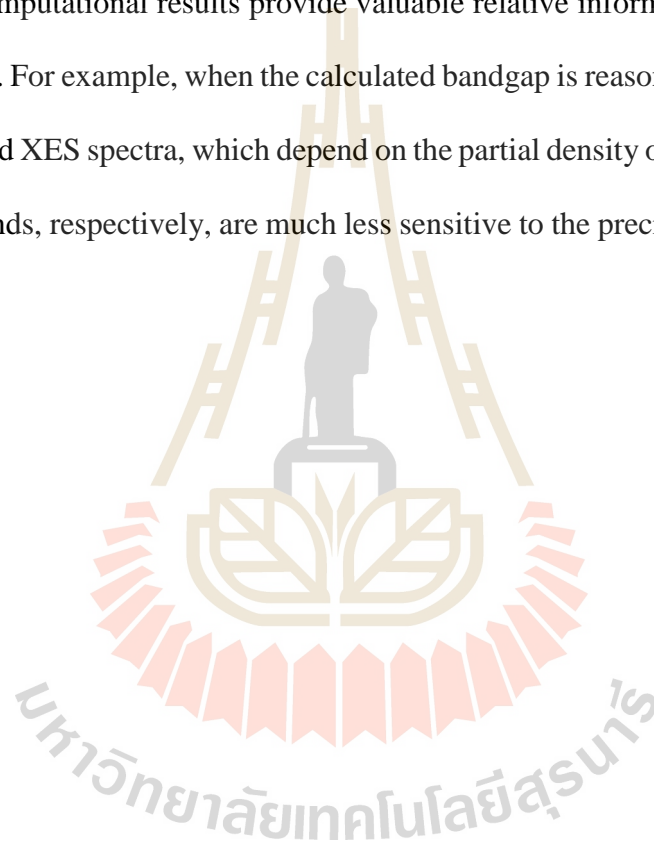
This research is divided into two parts. The first part aims to study and verify electronic band structures of interested materials by first-principle calculations as well as forming the proper framework to compare the calculated results with the experimental ones from RXES technique. The second aims to study the off-centering defects of cations in a selected perovskite structure in order to find probable structure of the material. To confirm the proposed local structure model the simulation of x-ray absorption spectroscopy and/or x-ray emission spectroscopy are generated on the predicted-to-exist defects and compared with actual measurements if possible.

1.3 Scope and limitation of the study

Scope: This thesis covers, first, the study of electronic band structures of Graphene and InN by RXES technique. The RXES spectra from available experiments are compared to the calculated ones in order to verify the electronic band structure of these materials. Second, the study of probable local structure of $\text{Bi}(\text{Mg}_{0.5}\text{Ti}_{0.5})\text{O}_3$ (BMT) and the suggestion on how to probe its cations' off centering by using XAS technique. The calculated spectra are performed based on first principle calculations for future experiments to verify its actual

structure. The RXES spectra are calculated through LMTO code while the XAS ones are done through FEFF code.

Limitations: Generally, DFT leads to the band gaps that are too small, preventing direct comparisons of electronic levels with experiments. However, there are various available band gap correction schemes that can be used reasonably well in many cases. In many cases, computational results provide valuable relative information even without band gap corrections. For example, when the calculated bandgap is reasonably large the calculated XAS spectra and XES spectra, which depend on the partial density of states of the conduction and valence bands, respectively, are much less sensitive to the precise value of the band gap.



CHAPTER II

BASIC THEORIES OF X-RAY TECHNIQUES

In this thesis study only two types of x-ray techniques are used and will be discussed in this chapter, the x-ray absorption near edge structure (XANES) and resonant x-ray emission spectroscopy (RXES).

2.1 X-ray absorption near edge structure

2.1.1 Basic principle of x-ray absorption

X-ray absorption spectroscopy (XAS) is a widely popular used technique due to its easy accessibility from synchrotron facilities around the world. It is a very powerful technique for structural analysis of materials. In XAS, an x-ray beam with sufficient energy ejects a core electron from an atom. Each core energy level has a distinct binding energy and thus when the x-ray energy is scanned through the binding energy of a core level the absorption cross-section increases abruptly. This gives rise to a so called absorption edge. Each absorption edge represents a different core-electron binding energy. The edges are named according to the principle quantum number of the excited electron: K for $n = 1$, L for $n = 2$ M for $n = 3$, and so on.

If x-ray of Intensity I_0 are incident on a sample as schematically shown in Figure 2.1a the extent of absorption depends on the photon energy E and sample thickness t .

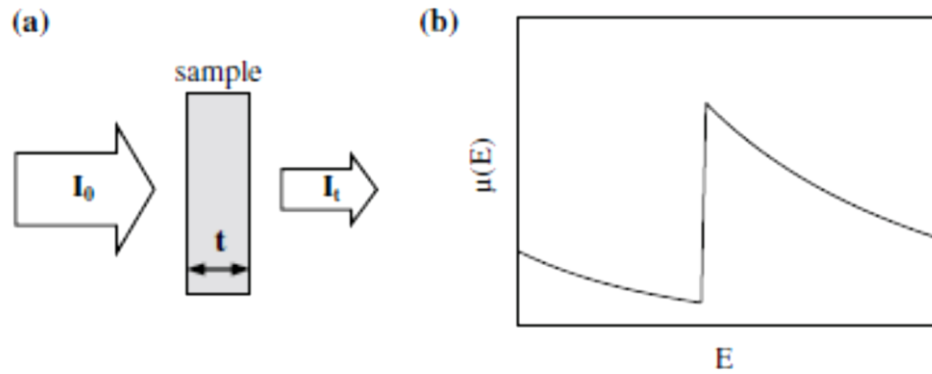


Figure 2.1 (a) Schematic of incident and transmitted X-ray beam and (b) absorption coefficient $\mu(E)$ (Schnohr et al., 2015).

According to Beer's Law, the transmitted intensity I_t is defined by

$$I_t(t) = I_0 e^{-\mu(E)t}, \quad (2.1)$$

where $\mu(E)$ is the energy-dependent X-ray absorption coefficient. Over large energy regions, $\mu(E)$ is a smooth function of the photon energy, varying approximately as $\mu(E) \sim dZ^4/mE^3$ (Kelly, 2008). Here d denotes the target density, Z the atomic number and m the atomic mass. Therefore, $\mu(E)$ decreases with increasing photon energy. If the energy equals or exceeds the binding energy of a core electron, a new absorption channel occurs in which the photon is annihilated thereby creating a photoelectron and a core-hole. This leads to a sharp increase in absorption coefficient as shown schematically in Figure 1.1(b). Above the absorption edge, the difference between the photon energy and the binding energy, left-over energy, is then converted into kinetic energy of the photoelectron while $\mu(E)$ continues to decrease with increasing photon energy. The core-hole life time is approximately 10^{-15} s, the core-hole is filled by an electron from a higher energy state. The corresponding energy difference is then released mostly via fluorescence X-ray or Auger electron emission (Kelly, 2008).

2.1.2 Absorption fine structure

According to quantum mechanical perturbation theory, the probability of a deep core electron from state $|i\rangle$ of an absorbing atom transitioning into some unoccupied

state $|f\rangle$ is described by Fermi's Golden Rule:

$$\mu(E) \propto \sum_f^{E_f > E_F} |\langle f | \hat{\epsilon} \cdot \mathbf{r} | i \rangle|^2 \delta(E - E_f), \quad (2.2)$$

where $\hat{\epsilon} \cdot \mathbf{r}$ the dipole operator for the incident electromagnetic wave interacting with the material. $\mu(E)$ is the absorption coefficient, which is the sum over all energies above the Fermi energy. The core state is typically a 1s, 2s, or 2p state. The dipole operator and delta function factors both cause a modulation of the absorption coefficient thus creating the X-ray absorption fine structure (XAFS). X-ray energies for which the photon can be absorbed, the photoelectron will be excited to unoccupied bound states of the absorbing atom as shown schematically in Figure 2.2(a) This can lead to a strong increase of the absorption coefficient at particular X-ray energies corresponding to the energy difference between the core level and the unoccupied states.

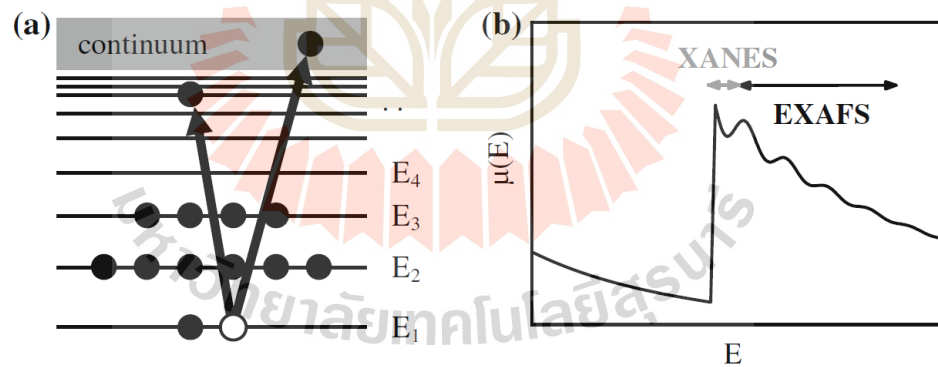


Figure 2.2 (a) Schematic of the absorption process and (b) absorption coefficient $\mu(E)$ versus photon energy E including the fine structure above the edge divided into the XANES and EXAFS regions (Schnohr et al., 2015).

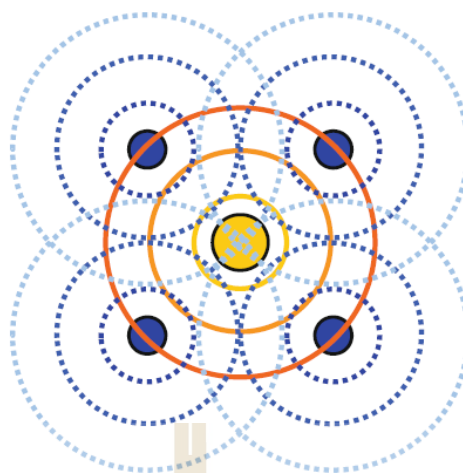


Figure 2.3 Schematic showing the absorbing atom (yellow) and its first nearest Neighbors (blue). An interference pattern is created by the outgoing (solid orange lines) and reflected (dashed blue lines) photoelectron waves.

At the higher energies of incident, the photoelectron is excited to a continuum state. The created wave propagates outwards and is scattered by neighboring atoms (Rehr et al., 2000) as shown in Figure 2.3. The interference of outgoing and scattered waves depends on the photoelectron wavelength and geometry of the absorber environment. The former is inversely proportional to the photoelectron momentum and therefore changes with photon energy. Thus, the final state is an energy-dependent superposition of outgoing and scattered waves. Because the initial state is highly localized at the absorbing atom, the matrix element M in Eq. (2.2) depends on the magnitude of the final state wave function at the site of the absorbing atom. Constructive or destructive interference of outgoing and scattered waves thus increases or decreases the absorption probability, creating an energy-dependent fine structure of the absorption coefficient. Figure 2.2(b) schematically shows the $\mu(E)$ fine structure as a function of photon energy. The fine structure typically consists of two regions, namely the X-ray absorption near edge structure (XANES) for the region very close to the absorption edge and the extended X-ray absorption fine structure (EXAFS) for the photon

energies higher than ~ 30 eV above the edge. XANES is characterized by transitions of the photoelectron to unoccupied bands, thus, it is sensitive to the valence states and bandwidth, chemical bonding and oxidation states of the absorbing atom (Kelly, 2008). The XANES features are also influenced by multiple scattering effects which depend on the geometry of the crystal structures. Therefore it is a good technique to distinguish between crystal phases or structures which will be one of the main focused points in this thesis. On the other hand, EXAFS yields information about the interatomic distances, near neighbor coordination numbers, and lattice dynamics.

2.1.3 Multiple scattering theory and XANES

Generally, there are two approaches in solving for the absorbing coefficient in Eq. (2.2) (Ravel, 2005). The first one is based on the molecular orbital theories and the second, multiple scattering theory. Although both methods are computationally distinct from each other, it is important to understand that they are formally equivalent, only the choice of approximation being used in solving Eq. (2.2) will differentiate them. The detail of each approach shall be discussed as follows:

(1) *Molecular Orbital Theories:*

The summation in Eq. (2.2) can be evaluated after representing the accurate initial and final states (Cowan, 1981). The initial and final states of the system can be obtained by solving the Schrodinger's equation and the absorption coefficient can be calculated directly from Eq. (2.2). This can be done by various quantum computational solid states physics codes, for examples, LMTO (Cabaret, 1999), Wein2k (Blaha, 2014), VASP (Kresse et al., 1994; Kresse et al., 1996) and Siesta (José et al., 2002) VASP and Siesta use pseudopotential which do not include core electrons in the calculations, thus the accurate initial states $|i\rangle$ are not available. However, by assuming that the distortion of core states of an atom in a material is very small and negligible. The core state of the isolate atom can be used as $|i\rangle$ for that of the material. The only caution to this approach is that the absolute

absorption energy may not be accurate due to the slightly difference in the core state energy between the isolate atom and the one in the material. By considering the Fermi's Golden Rule in Eq. (2.2), the initial and final states must have different parities (odd/even). For example, the allowed final states for the transition of a 1s (even) state are the p states (odd) only. By this assumption, one can use site-projected partial density of states of the absorbing atom to describe the absorption coefficient $\mu(E)$. This approach was previously performed by using VASP code (Limpijumnong et al., 2006).

(2) *Multiple Scattering Theory* (Ravel, 2005):

In this approach, the Eq. (2.2) will be rewritten using a Green's function. A system consists of ions and electrons which create a flat interstitial potential V_{int} . The ions can be considered as scattering sites of potential δV . Therefore, the potential of the system can be written as $H = H_0 + V_{int} + \delta V$ and the one-particle Green's function as $G(E) = 1/(E - H + i\zeta)$. Eq. (2.2) can now be rewritten as:

$$\mu(E) \propto -\frac{1}{\pi} \text{Im} \langle i | \hat{\epsilon}^* \cdot \mathbf{r} G(E) \hat{\epsilon} \cdot \mathbf{r} | i \rangle \Theta(E - E_f), \quad (2.3)$$

where Θ is the Heaviside step function which assures that the cross section is non-zero only above the Fermi energy, E_f . G is the full one-electron propagator in the presence of the scattering potential which can be written in a series by using Dyson equation as $\mathbf{G} = \mathbf{G}^0 + \mathbf{G}^0 \mathbf{T} \mathbf{G}^0$, where \mathbf{G}^0 is the free-electron propagator which is a function that describes how an electron propagates between two points in a free space, $\mathbf{G}^0 = 1/(E - H_0 + i\zeta)$, and $\mathbf{T} = \mathbf{V} + \mathbf{V} \mathbf{G} \mathbf{T}$ is the full atomic scattering matrix (Beeby, 1967; Lloyd et al., 1972). \mathbf{T} can be written in terms of the single site scattering matrices t as

$$\mathbf{T} = t + t \mathbf{G}^0 t + t \mathbf{G}^0 t \mathbf{G}^0 t + \dots \quad (2.4)$$

By substituting \mathbf{T} from Eq. (2.4) into the Dyson equation, it can be rewritten and recognized as a Taylor expansion:

$$\mathbf{G} = \mathbf{G}^0 + \mathbf{G}^0 \mathbf{t} \mathbf{G}^0 + \mathbf{G}^0 \mathbf{t} \mathbf{G}^0 \mathbf{t} \mathbf{G}^0 + \dots \quad (2.5)$$

$$\mathbf{G} = (\mathbf{I} - \mathbf{G}^0 \mathbf{t})^{-1} \mathbf{G}^0 \quad (2.6)$$

Eq. (2.4) and (2.5) are the basis of how XANES and EXAFS spectra are generated in FEFF. XANES spectra are computed by directly inverting the matrix $(\mathbf{I} - \mathbf{G}^0 \mathbf{t})$ in Eq. (2.6) while Eq. (2.5) is used as the basis for EXAFS analysis.

It is worthwhile to explain the physical interpretation of these equations. First of all, after the incident X-ray is absorbed by the absorbing atom and the photoelectron is ejected, \mathbf{G} describes all the possible ways that the photoelectron scatters from the surrounding atoms before the core-hole is refilled. \mathbf{G}^0 describes how an electron travels between two points in space (Rehr et al., 1990). \mathbf{t} describes how a photoelectron scatters from a single atom. Now consider each term in Eq. (2.5). $\mathbf{G}^0 \mathbf{t} \mathbf{G}^0$, $\mathbf{G}^0 \mathbf{t} \mathbf{G}^0 \mathbf{t} \mathbf{G}^0$ describes all the possible ways that a photoelectron can scatter off a neighboring atom only one time, and two times respectively, and the next terms describe the possible ways that the photoelectron can scatter three, four, five times and so on. In the multi scattering theory, only closed scattering paths of the photoelectron are considered in the summation for XAS. Examples of the scattering paths are schematically shown in Figure 2.4. Path #1 is an example of a single scattering paths #2 and 3 are examples of double scattering paths while paths #4 and 5 are examples of triple scattering paths. However, the scattering paths that are further away from the absorbing atom have very little effect, therefore only a few scattering paths from the few closest neighboring atoms are considered. This scheme is adopted in FEFF codes which is widely used for XAS calculations.

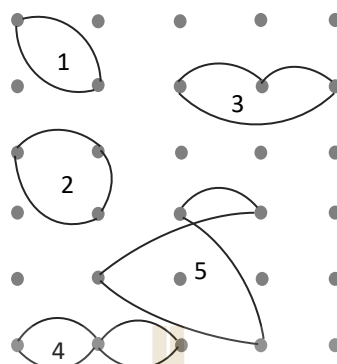


Figure 2.4 Schematic Examples of scattering paths. Path 1 is a single scattering path. Paths 2 and 3 are examples of double scattering paths. Paths 4 and 5 are examples of triple scattering paths.

In this thesis we use FEFF 8 which implements self-consistent potentials. The calculation begins with atoms placed at the positions specified in an input with the electronic configurations of free atoms. The potential is then calculated with the muffin-tin potential scheme (Mustre de Leon et al., 1991) which is the big improvement in this version of FEFF. This gives more accurate results for XANES.

XANES calculation can be very useful in the research problems where the real structure of the material is not known. In this case, the computational experiments can be performed by modifying the input data for FEFF. The calculated XANES from different possible model structures can give the hints to the experimental trends and the insights to the interpretation of the experimental XANES spectra. In Chapter V, we use FEFF code to generate XANES spectra for proposed models of $\text{Bi}(\text{Mg}_{0.5}\text{Ti}_{0.5})\text{O}_3$ in order to find the off-centering features of this material which can be used to identify the actual structure of materials when comparing to future experiments.

2.2 Resonant x-ray emission spectroscopy

2.2.1 Introduction

X-ray emission spectroscopy (XES) is a powerful experimental technique to probe electronic band structure of crystal systems. The technique is based on atom-specific projection. In XES a core electron excited by an incident x-ray and leave behind a core hole which is then recombined with an a valence electron. During the transition process a photon of matching energy is emitted. Experiments can be achieved by varying the excitation energy in various small steps throughout the core-hole excitation region and measure the emission spectra. This technique is made possible because of the development of the third generation synchrotron facilities with high brilliance beam based on undulators radiation, new high-resolution spectrometers and inserting devices which eliminate drawbacks and the low signal rates problem that existed at the early stage of the development. While the widely established technique of Angle Resolved Photoelectron Spectroscopy (ARPES) is good for determining electronic band structures of surfaces, RXES is good for buried interfaces and bulk systems which are not accessible for ARPES.

XES can be broadly classified into two categories. The first one is called “resonant x-ray spectroscopy” (RXES), which is the main focus of this thesis and will be discussed again in chapter IV. For RXES, the incident x-ray energy resonates with the excitation threshold of the core electron. The second one is called “normal x-ray emission spectroscopy” (NXES) or “ordinary x-ray emission”. For NXES, the incident x-ray energy is at high enough to ionize the core electron or to excite it to a high energy continuum well. By considering the emission energy RXES is further divided into two subcategories, resonant elastic and inelastic RXES, also often referred to as resonant inelastic x-ray scattering (RIXS). This is explained by Figure 2.5, the schematic representation of the two categories of RXES. For the elastic x-ray emission spectroscopy, the initial and final states of the two-

steps process are the same which means that the excitation energy (E_{in}) and the emitted energy (E_{out}) from the electronic relaxation are the same, therefore, no energy loss during the process. On the other hand, the final state is not the same as the initial state for RIXS. After the core electron is excited, the decay occurs from a valence state or a higher core state and emits the energy (E_{out}) corresponding to the energy differences between the valence and core states involved in the decay.

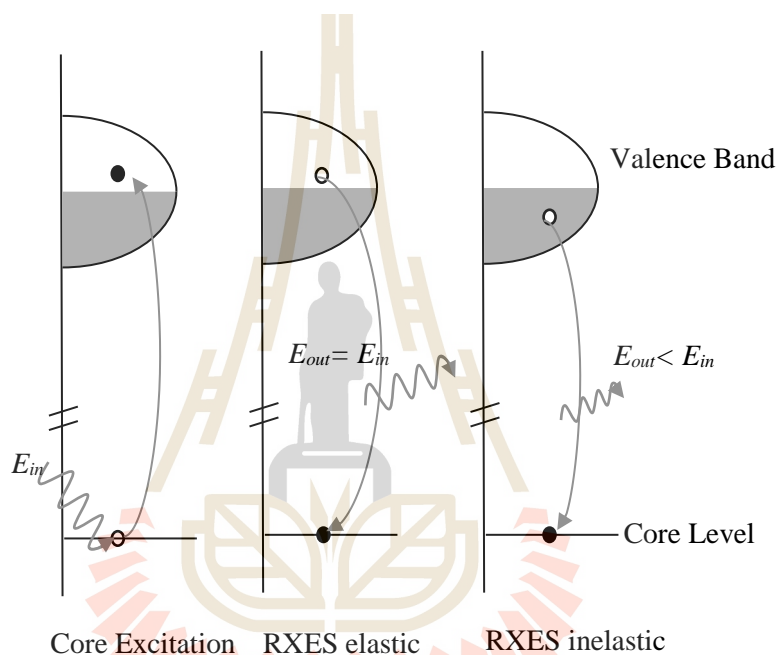


Figure 2.5 Resonant x-ray emission spectroscopy. The first figure, the incoming x-ray with energy E_{in} excites a core electron into an empty valence state. The middle figure, explains the resonant elastic x-ray emission, the excited electron decays and emits the same amount of energy as the excited energy, $E_{out} = E_{in}$. The last figure on the right explains the resonant inelastic x-ray emission where the electron from a lower valence or core state decay and emits the energy less than the excited energy, $E_{out} < E_{in}$.

RXES can be applied to surface adsorbates which can provide an atom-specific projection of the electronic structure in samples that has different type of bonding (Nilsson et al., 2004). Combining with theoretical calculations, RXES is a very powerful method to obtain more extensive mapping of the bands in crystalline anisotropy such as

found in the case of ZnO (Preston et al., 2008). RXES can also be used in the cases of highly oriented system such as N₂ molecules on Ni (100) surface. The angular dependent RXES makes it possible to identify the separation of states of different symmetry of the involved orbitals.

2.2.2 Theory of resonant x-ray emission spectroscopy

In the RXES process, the whole process should be described as a single event rather than two independent, XAS and XES, processes as described in Figure 2.6 for the case of RIXS. The whole process involves the absorption of one photon and the emission of one photon. In the case that the life time of the intermediate state $|m\rangle$ is very short comparing to the interaction time between photon and the atom, the absorption and emission processes are not independent and cannot be treated separately but as a single scattering event. In the early work on theory of broad band solids by (Gel'mukhanov et al., 1997), the important part in the whole process is the conservation of momentum. As described in Figure 2.6.

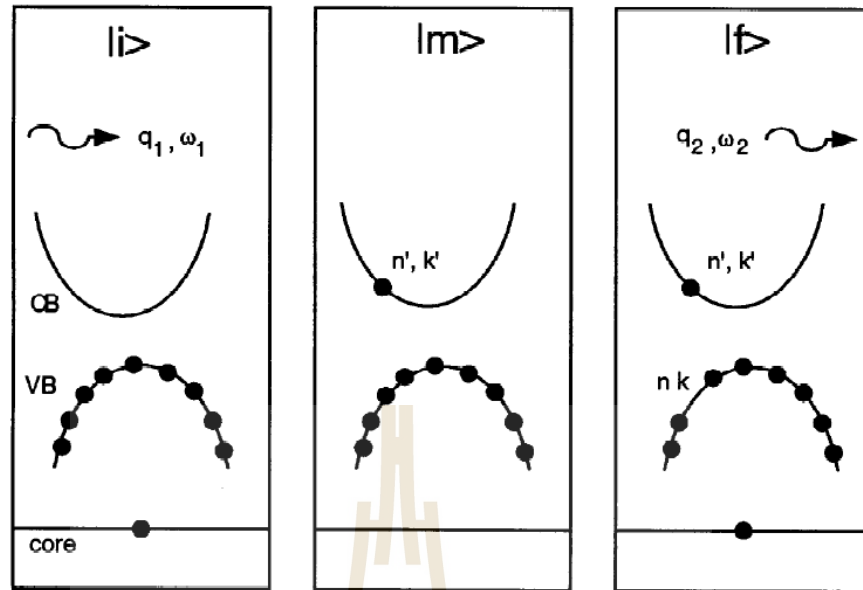


Figure 2.6 Initial ($|i\rangle$), intermediate ($|m\rangle$) and final ($|f\rangle$) state of an inelastic x-ray scattering process in a single electron picture. In the initial state, a photon with angular frequency ω_1 and momentum q_1 is present. In the solid, all conduction band states are unoccupied, including in particular the core level n_c located on atom R_j . In the intermediate state, the absorption of the photon has prompted the electron from the core level n_c at R_j into conduction band state characterized by n' (band index) and k' (wave vector). In the final state, a former valence electron with the quantum number n, k has filled the core vacancy. An electron in the conduction band state n'', k'' and a photon with angular frequency ω_2 and momentum q_2 are present.

If we consider the whole process of translations as a single event, the only difference between the initial and final state is the additional of the electron-hole pair in the final state while the core electron still exists in both states, thus, this does not break the translational symmetry. Therefore the momentum is conserved throughout the scattering process. The RXES spectra cross section is calculated based on the transition probabilities as described by Kramers-Heisenberg formula (Eisebitt, 2000; Kotani et al., 2001):

$$\left[\frac{d\sigma}{d\Omega d\omega_2} \right] \propto \sum_{k \in BZ} \sum_{c,v} \left| \frac{\langle s | p_\alpha | ck \rangle \langle vk | p_\beta | s \rangle}{\epsilon_{ck} - \epsilon_s - \omega_1 - i\Gamma_m/2} \right|^2 \times \delta(\omega_1 - \omega_2 - \epsilon_{ck} + \epsilon_{vk}), \quad (2.7)$$

where $\epsilon_{ck}, \epsilon_{vk}$ represent the single – particle band energies of a conduction and valence band respectively. ω_1 represents the incident photon (x-ray absorption) energy corresponding to the energy that excites a dipole transition, p_α , from a core state $|s\rangle$ with energy ϵ_s onto a conduction band state $|ck\rangle$. ω_2 represents the photon energy of the x – ray emission when a valence electron from the same wave vector recombines with the core hole. α and β denote the polarizations of the absorption and emission respectively. The sum is calculated over the full Brillouin Zone (BZ). In this formula, we use units with $\hbar = 1$. Γ_m represents the life time broadening factor of the core hole, which m denotes the intermediate state of the event. The last term with δ function indicate that energy conservation is valid, indicating that the absorbed and emitted photon energies must equal that of the (constant wave vector) interband transitions. In other words, at each incident photon energy, ω_1 , we make a horizontal slice or a constant energy line through the band-structure energies and then we obtain the k points in the bands which contributes to the vertical interband transitions. For those bands, the matrix elements are nonzero by the selection rules. Thus, the calculation requirement for this situation is essentially the same as that of an interband optical dielectric function except that now the matrix elements involve the resonant factor that contains a product of two momentum matrix elements coupling both the conduction and valence band states to the same core state. We then plot it as function of the x-ray emission energy, ω_2 .

The optical matrix elements between core and band states are calculated in an all – electron method based on a muffin – tin type augmentation method such as the muffin – tin orbital method (LMTO) or the linearized augmented plane wave (LAPW). In this thesis we use the full potential FP - LMTO as will be discussed later in chapter IV. The contribution

from each eigenstate to partial waves in the muffin-tin sphere are readily obtained from the eigenvectors of the band-structure problem and the augmentation properties of the basis functions to radial solutions inside each sphere. The integration over the Brillouin zone is similar to that used in the calculation of the optical joint density of states.

It is important to mention that in our current implementation of CRXES, the key approximation is that the wave vector of the x-ray is negligible compared to the size of the BZ and the two band states involved with the process occur at the same k points. In other word, the overall crystal momentum is conserved and the intermediate state with the core hole does not break the crystal periodicity.

2.2.3 Extracting band structure information from RXES experiments

2.2.3.1 Recipe for RXES

The general procedure of RXES experiment is to record an x-ray absorption spectrum at the absorption energy of interest. The recorded absorption spectrum gives the information about localize features in the unoccupied states. This can be explained, as an example, in Figure 2.7. A series of spectra, RIXS spectra, are then recorded for particular excitation energies and this requires a high resolution in the emission channel in order to detect small changes in the spectrum as a function of excitation energy. How selectively the core electron can be excited into certain region of BZ depends on the resolution of the incoming photons and the band structure of the unoccupied states of the crystal. This transition probability is described by the Kramers – Heisenberg formula as mentioned in section 2.2.2.

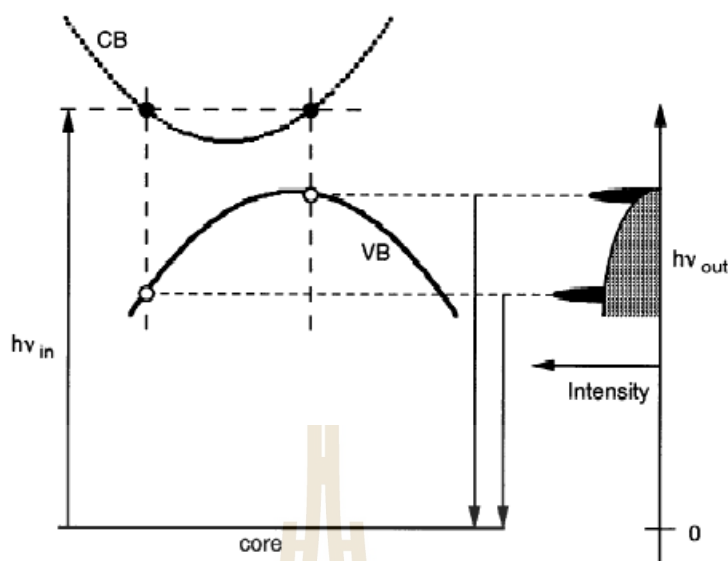


Figure 2.7 Illustration of the connection between the band structure and the experimental RIXS spectrum. A core electron is promoted into the CB by a dipole transition. The excitation energy $h\nu_{in}$ determines via the resonance condition of the Kramers–Heisenberg formula the energy and of the CB electron, which in turn restricts the CB electron to certain wave vectors. VB electrons with the same wave vector will contribute preferentially to the emission. $h\nu_{in}$ and $h\nu_{out}$ are both measured relative to the same core level. The involvement of the core level makes RIXS a local probe. Dipole selection rules give additional symmetry information. The broad background in the RIXS spectrum is caused by k -unselective processes (Eisebitt, 2000).

The connection between RXES (or RIXS) spectrum and the structure is illustrated in Figure 2.7. According to Kramers – Heisenberg formula, the strongest contribution, when the resonance occurs, to the scattering process is obtained when the incident x-ray energy is high enough to excite a core hole to a formerly unoccupied state at the energy $E_{core} + h\nu_{in}$. The choice of which core state will be excited and which CB states the core electron will transition is governed by the dipole selection rule. With the assumption that the photon momentum is very small compared to the crystal momentum, the momentum

is conserved for the overall process. This means that only the VB electrons with the same wave vector as the excited electron in the CB will fill the core hole and contribute to the RXES spectrum. How much the contribution from a state will be depends on its transition matrix element with the core state. According to Figure 2.7, the energy of certain CB states are determined from the RXES spectra (as indicated by horizontal lines), while the momentum is determined by the wave vector of the electron in the CB in the final state of the scattering (as indicated by the vertical lines). Therefore, the emission spectra are dependent on the x-ray excitation energy, as different excitation energies probe different parts of the BZ.

Generally, the intensity in the RXES spectrum from experiments are not only contributed from the model mentioned above (the “coherent” component) but, in fact, RXES spectra are also contributed from the k – unselective transitions according to LPDOS. For example, a previous RXES study on diamond by Ma et al. showed that the energy dependent LPDOS component, which is called “incoherent” part, is responsible for approximately 60% of the RXES intensity.

2.2.3.2 Experimental difficulties

There are a few experimental difficulties dealing with RXES that we will discuss in this section as follows (Eisebitt, 2000):

- *Determination of Absorption Threshold*

In RXES, it is more convenient to express excitation energy relative to the CB minimum than the absolute excitation energy. Hence it is crucial to determine the absorption threshold with very high resolution. In practice, the real process of the determination involves a lot of difficulties such as phonon broadening, the core hole life time, experimental resolution or other broadening mechanisms. However, the band structure calculation can be used to assist in analyzing the data. The absorption threshold can be determined by broadening the unoccupied LPDOS and comparing it to the absorption spectrum.

- *Reflection*

In RXES, the excitation energies are usually measured close to the absorption threshold. If the material bandgap is small the excitation energy is close to the x-ray emission features at the VB maximum. Diffusely or specularly reflected radiation can be contributed to the RXES spectra depending on the reflectivity and the geometry of the sample as in InN which only has a narrow band gap of 0.7 eV.

- *k – unselective Contribution*

If we use high excitation energy far above the excitation threshold, the RXES spectrum generally represents the LPDOS (if no correlation satellites are present). This recorded spectrum is important because it represents the shape of the k-unselective contribution to the RXES that can be subtracted from the raw data to give the k-selective contribution. This can be seen more clearly in our study of Graphene in chapter III. However, this approach is not possible for the material that its core level has other close levels at the lower binding energy, such as spin-orbit split partner. In this case, the spectrum at high emission energy will not represent the LPDOS but the superposition of the transitions to these different levels.

2.2.4 RXES experiments (Eisebitt, 2000)

RXES is considered as a new method with young history comparing to a well-established ARPES. The way to look at its history is to characterize by the band structure information gained from the experimental data. The very first experiments showed the connection between RXES spectra and the dispersion relations $E(k)$ of the unoccupied and occupied states. Energy dependent features of RXES spectra were assigned to high symmetry points in the band structure by comparing with calculated band structures from first principle calculations. The next step was toward a more quantitative understanding by simulating the spectra based on band structure calculations. Later RXES data in conjunction with first principle calculations were used to map band structure in a similar way to that of ARPES.

The first time excitation energy dependent features in RXES spectra have been observed was in the vicinity of the 2p absorption threshold in crystalline silicon by (Rubensson et al., 1990). However, the connection of the spectral changes to electron wave vector was not explained at the time. The explicit explanation of the momentum conservation in such experiments was not established until (Ma et al., 1992) started to investigate carbon 1s level in diamond in 1992. The spectra features were assigned to high symmetry points by comparing to other results on the diamond band structure. This was the crucial step toward the conclusion that conservation of crystal momentum applies in RXES. This realization has stimulated a considerable amount of work in this field since 1992. However, the energy dependent features in the RXES spectra were seen only for the crystalline, not for amorphous silicon which lacks the long range order (Miyano et al., 1993). From Figure 2.7 we can see that it is not easy to separate the information on the occupied and unoccupied states. Which k points are selected by a certain excitation energy depends on the unoccupied states. How those k points contribute to RXES spectrum depends on the occupied states. The information on the band structure can be extracted through this connection. If the band structure of the unoccupied states is known then the calculated band structure can be checked by RXES experiments by simulating the RXES spectra based on the calculated band structure, as being done on Graphene and InN in chapter III and IV respectively. The similar approach has been recently performed on ZnO by (Preston et al., 2011).

In summary, RXES has unique advantages in the investigation of electronic band structure $E(k)$. (1) It is a local and element selective probe. (2) It has a large probing depth which makes it possible to investigate buried structures and impurities in materials without surface reconstruction issues, hence bulk properties can be investigated. (3) It is symmetry selective, for example, if N 1s in InN is investigated then p-type states will be probed. (4) No problem with magnetic or electric field from sample charging as in ARPES, hence it can even be used to probe insulators.

2.2.5 Angular dependence and experimental geometry

This part has been theoretically and experimentally performed on (Preston et al., 2011) wurtzite ZnO, which is also applied in our work in this thesis on both for graphene and InN. However, the approach on how to compare between experimental and calculated data are slightly different as will be explained in chapter IV and V.

The dipole selection rules in Eq. (2.7) leads to the angular dependence of the RXES cross section (will be written as $M_{\alpha\beta}$ from now on). Strictly speaking, if we consider the K edge spectra where the transition occurs from s-core states, only the matrix elements which have the p-orbital contribution valence and conduction bands will be included in the two dipole-moment matrix elements. The indices α and β in Eq. (2.7) indicate the Cartesian components of the momentum operators of the XAS and XES parts of the process respectively. These components are determined by the polarization of the incoming (e_i) and outgoing (e_o) beams. Different independent cross sections can be determined in the crystal depending on the crystal symmetry. Here, we introduce two matrix elements p^{XAS} and p^{XES} for the XAS and XES momentum operators respectively. The angular dependent of the cross sections is determined by $|e_i \cdot e_{\alpha}^{XAS}|^2 |p^{XES} \cdot e_o|^2$. For example, a hexagonal crystal, such as wurtzite ZnO and InN, there are four independent components, $M11$, $M33$, $M13$, and $M31$, where 3 refers to the c axis of the crystal and 1 to a direction perpendicular to the c axis respectively.

Generally, from the theory point of view we describe the polarization directions relative to the crystalline symmetry axes versus the experimental geometry. Therefore, we have to determine the fraction of the independent components of the cross-section matrix M that enter measured cross section. In other words, the projections of the incoming and outgoing polarization unit vectors on the relevant crystal axes are required for the calculation. The cross-section matrix can now be written as:

$$M_{io} = |e_i \cdot e_{\alpha}^{XAS}|^2 M_{\alpha,\beta} |e_o \cdot e_{\beta}^{XES}|^2, \quad (2.8)$$

where e^{XAS} and e^{XES} are the unit vectors along the XAS and XES momentum matrix element respectively.

There can be many ways to change the experimental conditions: change the position of the spectrometer, alter the photon polarizations, rotate the sample, and choose different cleavage planes of the same sample. Hence, it is crucial to consider three different sets of coordinates, the laboratory frame coordinates (x', y', z') , the coordinates that are fixed to the sample with a specific cleavage plane (x, y, z) , and the coordinates which correspond to the natural symmetry axis of the crystal $(1, 2, 3)$. As an example from the previous work by (Preston et al., 2011).

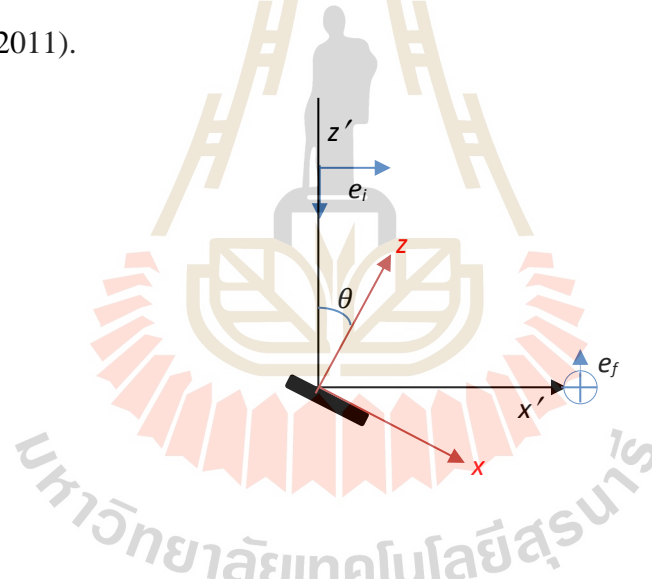


Figure 2.8. The experimental geometry. The laboratory coordinates x', y', z' (black) and the sample coordinates x, y, z (red) are shown. Photons (black arrows) are incident along z and emitted photons are collected along x . The angle between the sample normal and the incident beam, θ , is freely changed during the experiment. by (Preston et al., 2011).

From Figure 2.8, the undulators shine an incident light along z' direction, as a result, the polarization is along x' . The emission spectrometer is mounted perpendicular to the incoming photon in the x' direction, however, its polarization is not resolved. Finally, the sample is mounted on a manipulator which can be rotated about y' axis. On the other hand,

the z axis is defined to be normal to the cleavage plane of the sample, the x axis is the intersection of the cleavage plane with the photon and $y = y'$. In other words, the incoming x-ray being used here is always p-polarized. θ , the angle between the incoming beam and the normal to the sample, determines the sample orientation. We then have

$$e_i \cdot e^{XAS} = e_x \cdot e^{XAS} \cos\theta + e_z \cdot e^{XAS} \sin\theta \quad (2.9)$$

$$e_o \cdot e^{XES} = e_x \cdot e^{XES} \sin\theta \cos\phi + e_y \cdot e^{XES} \sin\theta \sin\phi + e_z \cdot e^{XES} \cos\theta \cos\phi \quad (2.10)$$

We also need to average over all possible emitted photon polarization angles in the $z'y'$ plane, ϕ . Since each polarization factor enters modulo squared for input and output, thus, the integration over the $\cos^2\phi$ and $\sin^2\phi$ factors simply gives a constant factor, $1/2$. We then obtain for the total CRXES cross section

$$M = \frac{1}{2} \left[\sin^2\theta \cos^2\theta (M_{xx} + M_{zz}) + \sin^4\theta M_{zx} + \cos^4\theta M_{xz} + \sin^2\theta M_{zy} + \cos^2\theta M_{xy} \right] \quad (2.11)$$

However, here x , y , and z are not yet referred to the crystalline symmetry axes but merely to the sample position in the laboratory. For a general cleavage plane with Miller indices (hkl) , the surface normal is $G_{hkl}/|G_{hkl}|$, which can be expressed in terms of the crystal symmetry axes, $\hat{1}, \hat{2}, \hat{3}$. Let $\hat{x} = \sum_i a_i \hat{x}_i$, $\hat{y} = \sum_i b_i \hat{y}_i$ and $\hat{z} = \sum_i c_i \hat{z}_i$. We can then construct a matrix,

$$R = \begin{pmatrix} |a_1|^2 & |a_2|^2 & |a_3|^2 \\ |b_1|^2 & |b_2|^2 & |b_3|^2 \\ |c_1|^2 & |c_2|^2 & |c_3|^2 \end{pmatrix} \quad (2.12)$$

which allows us to transform from xyz sample coordinates to the crystal axes coordinates

$$M_{ij} = R_{ij} M_{\alpha\beta} R_{\beta j}^T \quad (2.13)$$

Combining these steps, the measured cross section can be written as

$$M \propto (\cos^2\theta, \theta, \sin^2\theta) R M R^T \begin{pmatrix} \sin^2\theta \\ 1 \\ \cos^2\theta \end{pmatrix} \quad (2.14)$$

In the specific case of a hexagonal crystal cleaved along the c plane the R matrix is just a unit matrix, thus, taking into account the symmetries $M_{11} = M_{22} = M_{12} = M_{21}$, we immediately obtain

$$M \propto M_{11}\cos^2\theta(\sin^2\theta+1)+M_{13}\cos^4\theta+M_{31}\sin^2\theta(\sin^2\theta+1)+M_{33}\sin^2\theta\cos^2\theta \quad (2.15)$$

For the M plane ($1\bar{1}00$) cleave, with $[000\bar{1}]$ oriented along x , we obtain

$$M \propto M_{11}(1+\cos^2\theta)\sin^2\theta+M_{13}\sin^4\theta+M_{31}(1+\cos^2\theta)\cos^2\theta+M_{33}\sin^2\theta\cos^2\theta \quad (2.16)$$

while for the M plane with $[11\bar{2}0]$ oriented along x , we obtain

$$M \propto M_{11}+M_{13} \quad (2.17)$$

The above derivations allow us to simulate any measured spectra directly in terms of the calculated cross sections. On the other hand, it is clear that if we consider independent choices of measurement angle and cleavage plane, we obtain n equations from which we can extract the $n(\leq 9)$ unique cross sections experimentally and from there can predict those for other angles or cleavage planes. This is of use in cases where the band structure cannot (yet) be calculated to high accuracy, such as, strongly correlated systems.

CHAPTER III

CALCULATION METHODS

In this chapter, we will discuss about the basic concepts of first-principles calculation based on Density Functional Theory (DFT), the approximations which are used in the calculations, the basis functions, and the two well known codes which are used in this thesis, the Full-Potential Linear Muffin-Tin Orbital Method (FP – LMTO) and the Vienna Ab-initio Simulation Package (VASP). The first method is used in the calculation of RXES spectra of Graphene and InN while the second one is used for the calculation of the Bi(Ti_{0.5}Mg_{0.5})O₃. More detail about the two methods will be discussed further in this chapter.

3.1 First - principles calculation

The self-consistent electronic structure calculation based on the DFT methods are often called “ab initio” or “first-principles” because they do not require empirical inputs or adjustable parameters from experiments. To deal with the large system of N_n nuclei and N_e electrons explicitly, we begin with writing the Hamiltonian a

$$\begin{aligned}
 H = & -\frac{\hbar^2}{2} \sum_I^{N_n} \frac{\nabla_I^2}{M_I} + \frac{1}{2} \sum_I^{N_n} \sum_{I \neq J}^{N_n} \frac{Z_I Z_J e^2}{4\pi\epsilon_0 |R_I - R_J|} - \frac{\hbar^2}{2m} \sum_i^{N_e} \nabla_i^2 \\
 & + \sum_i^{N_e} \sum_{i \neq j}^{N_e} \frac{e^2}{4\pi\epsilon_0 |r_i - r_j|} - \sum_I^{N_n} \sum_i^{N_e} \frac{Z_I e^2}{4\pi\epsilon_0 |r_i - R_I|} \quad , \quad (3.1)
 \end{aligned}$$

where the indices i, j and I, J are used for electrons and nuclei respectively. M_I and R_I denote nuclear masses and positions while m and r_i are for electron masses and positions. Although this many-particle problem is nearly impossible to solve, fortunately, we can use the Born-Oppenheimer Approximation to reduce the complications. By considering that the nuclei do

not move in the time scale of the electrons, this allows us to separate the Hamiltonian into electronic and nuclear parts.

The last term in Eq. (3.1), the Coulomb interaction between the nuclei and the electrons, can be considered as an external potential V_{ext} seen by electrons. Then, the electronic Hamiltonian of the interacting many-body system in the atomic unit ($\hbar = m = e = 1$) can be written as

$$H_{el} = -\frac{1}{2} \sum_i^{N_e} \nabla_i^2 + \frac{1}{2} \sum_{i,j}^{N_e} \frac{1}{|r_i - r_j|} + \sum_i^{N_e} V_{ext}(r_i) \quad (3.2)$$

Now we have the electronic energy for fixed nuclear positions, we can then solve the separately nuclear motion problem. The eigenvalues of the electronic part together with the second term of Eq. (3.1), which is just a constant for fixed positions, now become the effective potential energy landscape for the nuclei. At this point, the positions of the nuclei can be varied and hence the properties of atomic bonding, energy changes under deformation, relaxations of the atoms etc. can be obtained.

3.2 Density Functional Theory (DFT)

Generally, directly solving the many-body Schrödinger equation of a system is very difficult. To get around that, DFT was introduced as a method to determine the ground-state properties of a many-electron system by expressing its total energy as a functional of the electron density which has only three instead of $3N_e$ variables of a many-electron wavefunction. The two theorems of Hohenberg and Kohn (HK) (Hohenberg et al., 1964) are the main keys to solving the problem. The first theorem states that there is a one-to-one mapping relation between the electron density and the external potential which means that the electron density uniquely determines the Hamiltonian and the many-body wave functions. Hence, each property of the many-body system is a functional of the ground state charge density. The second theorem establishes a variational principle for the total energy functional so that the ground state energy can be obtained by minimizing the energy over all

the possible densities. Although the HK theorem proves that the many electron wave function can be substituted by the electron charge density as a basic variable, it does not provide an explicit mathematical solution to the problem. Later in 1965, Kohn and Sham (Kohn et al., 1965) proposed that the kinetic energy can be expressed in terms of independent single particle wave functions. This non-interaction electron system in an effective potential consisting of the external potential and the exchange correlation interaction provides the same density as the actual interacting system, thus, can be considered as equivalent to each other. We now arrive at the set of equations as follows, the **Kohn-Sham (KS) equations**:

$$H_{eff}\psi_i(r) = \left(-\frac{\nabla^2}{2} + V_{eff}(r) \right) \psi_i(r) = \varepsilon_i \psi_i(r) \quad (3.3)$$

$$V_{eff} = V_{ext} + \int d^3 r' \frac{n(r')}{|r-r'|} + V_{xc}[n] \quad (3.4)$$

$$n(r) = \sum_i^{N_e} |\psi_i(r)|^2, \quad (3.5)$$

where $n(r)$ is the electron density, and $V_{xc} = \frac{\delta E_{xc}[n]}{\delta n(r)}$ is the functional derivative of the exchange correlation energy $E_{xc}[n]$ with respect to $n(r)$. Finally, once these equations are solved for $n(r)$ then the total energy can be written as

$$E[n] = \sum_i^{N_e} \varepsilon_i - \frac{1}{2} \int d^3 r d^3 r' \frac{n(r)n(r')}{|r-r'|} - \int d^3 r V_{xc}[n]n(r) + E_{xc}[n]. \quad (3.6)$$

Although the KS-DFT is considered as an exact theory, the actual exchange-correlation functional is not known, therefore, further approximations are still required. To explain the physical meaning of the exchange-correlation energy E_{xc} , let us consider an electron sitting in the electron cloud. The electron does not simply see an average charge density around itself because the other electrons try to avoid this spot for two reasons, the Pauli exclusion principle and electron repulsion. So we may consider this electron as being surrounded by a so-called exchange-correlation hole. Thus the exchange-correlation energy is essentially the interaction of the electron with its surrounding exchange-correlation hole.

At this point we will provide a brief explanation of several exchange-correlation functions including the Local Density Approximation (LDA) and Generalized Gradient Approximation (GGA) techniques to obtain E_{xc} in the ground state. After that we will discuss about the *GW* Approximation (*GWA*) method to study the one-electron excitations of the system.

3.2.1 Local Density Approximation (LDA)

In the local density approximation (LDA), it is assumed that the exchange-correlation energy at each point in space depends solely on the density at that point. LDA is a good approximation for the matters that can be considered as a homogeneous electron gas, the density n is constant. The exchange correlation energy $E_{xc}[n]$ has been calculated in various conditions, e.g. at low density by Wigner (Wigner, 1934) and high density by Gell-Mann and Brueckner (Gell-Mann et al., 1957). The interpolation formulas between these regimes is also made possible. LDA (Perdew et al., 1981) calculation starts from accurately computing the ground state of the homogeneous electron gas and then constructing the exchange-correlation energy per particle, $\epsilon_{xc}(n) = E_{xc}(n)/N$ as a function of electron density $n=N/V$. Then we apply the same expression at each point locally all over the actual inhomogeneous system. Finally, by integration we get

$$E_{xc}^{LDA} = \int d^3r n(r) \epsilon_{xc}(n(r)). \quad (3.6)$$

And the LDA exchange-correlation potential can be written as

$$V_{xc}^{LDA} = \frac{\partial(n\epsilon_{xc})}{\partial n}. \quad (3.7)$$

Although we assume that the density is varying slowly while LDA being constructed, the calculation still works remarkably well even for some realistic systems where the density is not slowly varying. This has been explained by the fulfillment of certain sum rules (Jones et al., 1989). The exchange-correlation energy is an average property of the exchange-correlation hole, as a result, it does not critically depend on the details of the pair-correlation

function. LDA successfully predicts the total energy, lattice constant, equation of state and relaxations of atomic coordinates around defects and at surfaces with less than 5% of error. However, one drawback of LDA is that it fails to give a reliable electronic excitation energy because it is a theory for the ground state total energy only. It tends to predict the smaller gaps in insulators or semiconductors than the experimental values. Another problem is that for the systems that consist of atoms which have localized electrons such as d and f electrons LDA tends to fail to give the accurate results even for ground state properties. For the systems which have surfaces or for molecules and free atoms, the electron density vary too quickly from inside to outside of the systems which means that the electron gas is no longer homogeneous, as a result, LDA also fails for these cases.

3.2.2 Generalized Gradient Approximation (GGA)

Under the assumption that in most materials the electron gas is not homogeneous like in the case of LDA. Thus the E_{xc} should deviate significantly from the LDA results. This deviation can be expressed in terms of the gradient and higher spatial derivatives of the total charge density. So GGA (Perdew et al., 1996) goes a little bit beyond LDA by including the density and also its gradient at each point in space. Therefore the exchange correlation energy can be modified to

$$E_{xc}^{GGA} = \int dr^3 n(r) f(n|\nabla n) \quad (3.8)$$

In various cases, it has been shown that GGA gives a better description of the exchange-correlation hole and gives a more realistic account of energy barriers and adsorption energies for molecules. Although GGA predicts very good results for molecular geometries, ground state total energies and surface energies, it is not clear whether GGA is an improvement over LDA for all ground state properties. In contrast with LDA, GGA typically overestimates lattice constants and underestimates phonon energies.

LDA and GGA are basically designed to study ground state properties: there is no real justification to interpret the KS one-electron eigenvalues (ϵ_i of Eq. (2.4) as excitation energies, i.e. the energy to extract or add an electron to the system. They are usually not applicable for systems with strongly correlated electrons and not completely self-interaction free. Thus in the next section we will discuss Green's function methods as a tool to study both ground state and excited state properties of the many-body problem.

3.3 GW Approximation (GWA)

GW approximation was originally proposed by Hedin (Hedin, 1965) and named after its construction of the electron self-energy from the Green's function (G) and the screened interaction (W). GW approach (Van Schilfgaarde et al., 2006) was introduced to improve LDA and GGA results by overcoming the problem with the incomplete cancellation of artificial self-interaction and the lack of discontinuity of the exchange-correlation potential with respect to the number of electrons, the KS eigenvalues cannot represent the quasi particle band structure measured by direct and inverse photoemission. In GW approach these issues are solved by properly including both dynamical and non-local effects into the approximation.

3.3.1 Green's function

The Green's function is a propagator or amplitude of the probability for a particle to travel from one position, at time t to another position, r' , at time t' . First of all, let us define field operators, $\psi^\dagger(r',t')$ and $\psi(r,t)$ as creation and annihilation operators written in the time dependent position basis. If we have a ground state wave function with N electrons in the system, $|N, 0\rangle$, when these field operators operate on the system we will get $N + 1$ or $N - 1$ electron wavefunctions which are not necessarily in the ground state.

We can write $\langle N,0|\psi(r,t)\psi^\dagger(r',t')|N,0\rangle$ as a propagator $iG^e(rt,r't')$ for an extra electron propagating from (r',t') to (r,t) and $\langle N,0|\psi^\dagger(r',t')\psi(r,t)|N,0\rangle = iG^e(r't',rt)$ as a propagator measuring a missing electron (hole) propagating from (r,t) to (r',t') . Therefore the one-electron Green's function can be written as

$$\begin{aligned} iG(rt,r't') &= \langle N,0|T\psi(r,t)\psi^\dagger(r',t')|N,0\rangle \\ &= \langle N,0|\psi(r,t)\psi^\dagger(r',t')|N,0\rangle \text{ for } t > t' \\ &= -\langle N,0|\psi^\dagger(r',t')\psi(r,t)|N,0\rangle \text{ for } t' > t, \end{aligned} \quad (3.9)$$

where T is the time-ordering operator which rearranges operators from right to left after increasing time and a minus sign is included for every interchange of fermion operators.

The field operator can also be written with the Heisenberg representation $\psi^\dagger(r',t') = e^{iHt'}\psi^\dagger(r')e^{-iHt'}$ and insert the closure relation into Eq. (2.9). Note that the limit of energy for electrons or holes injection is the chemical potential μ . Thus we can rewrite Eq. (2.9) as

$$\begin{aligned} iG(r,r',\tau) &= \sum_n \langle N,0|\psi(r)|N+1,n\rangle \langle N+1,n|\psi^\dagger(r')|N,0\rangle e^{-iE_n\tau}, \tau > 0, E_n \geq \mu \\ &= -\sum_m \langle N,0|\psi(r')^\dagger|N-1,m\rangle \langle N-1,m|\psi(r)|N,0\rangle e^{-iE_m\tau}, \tau < 0, E_m < \mu, \end{aligned} \quad (3.10)$$

where $\tau = t-t'$ and m and n represent quantum number to specify the state which are not the ground state. $E_n = E_n^{N+1} + E_0^N$ and $E_m = E_0^N + E_m^{N-1}$ respectively. Eq. (3.10) can also be Fourier-transformed into the frequency representation as

$$\begin{aligned} iG(r,r',\omega) &= \int_{-\infty}^{\infty} iG(r,r',\tau) e^{i\omega\tau} d\tau \\ &= \sum_n \langle N,0|\psi(r)|N+1,n\rangle \langle N+1,n|\psi^\dagger(r')|N,0\rangle \int_0^{\infty} e^{-i(\omega-E_n+i\eta)\tau}, E_n \geq \mu \\ &= -\sum_m \langle N,0|\psi(r')^\dagger|N-1,m\rangle \langle N-1,m|\psi(r)|N,0\rangle \int_{-\infty}^0 e^{-i(\omega-E_m+i\eta)\tau}, E_m < \mu \end{aligned} \quad (3.11)$$

The infinitesimal η is always positive to ensure that $G(r,r',\omega)$ has the correct analytic properties.

For any excited state, the quasiparticle amplitudes is defined as

$$f_s(r) = \langle N,0|\psi(r)|N+1,s\rangle \text{ for } E_s = E_s^{N+1} - E_0^N, E_s \geq \mu \quad (3.12)$$

$$f_s(r) = \langle N-1, s | \psi(r) | N, 0 \rangle \text{ for } E_s = E_0^N - E_s^{N-1}, E_s < \mu \quad (3.13)$$

After working out the integrals in the Eq. (2.11), we now get

$$G(r, r', \omega) = \sum_s \frac{f_s(r) f_s^*(r')}{\omega - E_s \pm i\eta}, \quad (3.14)$$

where the sum is over both electrons and holes and the \pm signs correspond to electrons and holes respectively.

Now let us review the explicit expression for the single-particle Green's function which was derived by Hedin. We begin from the Heisenberg equation of motion for the field operator.

$$i \frac{\partial \psi(x)}{\partial t} = [\psi(x), H] \quad (3.15)$$

Here, x denotes space, t for time and σ for spin. The Hamiltonian, H , is split into two parts noninteraction (H_0) and interaction parts.

$$H = \int dr \psi^\dagger(x) H_0(x) \psi(x) + \frac{1}{2} \int dr dr' \psi^\dagger(r, t) \psi^\dagger(r', t) v(r, r') \psi(r', t) \psi(r, t) \quad (3.16)$$

Now we can insert H from Eq. (3.16) back into Eq. (3.15) and this is when the second term becomes a problem. This term involves a two-particle Green's function, thus, we need to decouple this part by introducing the mass operator as

$$\int dx'' M(x, x'') G(x'', x) = -i \int dr'' v(r, r'') \langle N | T[\psi^\dagger(r'', t) \psi(r'', t) \psi(r, t) \psi^\dagger(r', t)] | N \rangle \quad (3.17)$$

The equation of motion for the Green's function can now be derived from Eq. (3.15)

$$\left[i \frac{\partial}{\partial t} - H_0(x) \right] G(x, x') - \int dx'' M(x, x'') G(x'', x') = \delta(x - x') \quad (3.18)$$

The average Coulomb interaction, V_H , can also be included in the non-interacting part, and the equation of motion for the Green's function can be rewritten as

$$\left[i \frac{\partial}{\partial t} - H_0(x) - V_H(x) \right] G(x, x') - \int dx'' \Sigma(x, x'') G(x'', x') = \delta(x - x') \quad (3.19)$$

Σ in Eq. (3.19) defines the self-energy. The self-energy in terms of the screened Coulomb interaction was derived by Hedin (Seitz, 1969) via Schwinger's functional derivative method. In this method, the electron-electron interaction itself is screened, thus, the

interaction is reduced. By expressing everything in the screened interaction we may arrive at a better-converging approximate method. Finally, we get the set of equations

$$\Sigma(1,2)=i \int d(34)G(1,3^+)W(1,4)\Lambda(3,2,4). : 1 \equiv (r_1, \sigma_1, t_1) \quad (3.20)$$

$$G(1,2)=G_0(1,2)+ \int d(34) G_0(1,3)\Sigma(3,4)G(4,2)$$

$$W(1,2)=v(1,2)+ \int d(34) v(1,3)P(3,4)W(4,2)$$

$$P(1,2)=-i \int d(34) G(2,3)\Lambda(3,4,1)G(4,2^+)$$

$$\Lambda(1,2,3)=\delta(1-2)\delta(2-3)+ \int d(4567) \frac{\delta \Sigma(1,2)}{\delta G(4,5)} G(4,6)G(7,5)\Lambda(6,7,3),$$

where W , Λ and P are the screened Coulomb potential, the vertex function and the polarization function respectively. The first step in solving this formidable set of equations through GWA is by assuming the vertex function $\Lambda(1,2,3)=\delta(1-2)\delta(2-3)$. We now get

$$\Sigma(1,2)=iG(1,2^+)W(1,2) \quad (3.21)$$

$$W(1,2)=v(1,2)+ \int d(34) v(1,3)P(3,4)W(4,2)$$

$$P(1,2)=-iG(2,1)G(1,2^+)$$

These equations can be solved self-consistently. For more details about GW method, review the articles in ref. (Seitz, 1969; Aryasetiawan et al., 1998).

3.3.2 GW correction to LDA energy

The GWA a perturbation approach that is applied to calculate the excitation energy from KS eigenfunctions and eigenvalues. It is just a one-shot correction to, for example, LDA. In the previous section, quasiparticle excitations were defined in terms of the poles of the Green's function, however, we can also introduce a quasiparticle wavefunction and energy into the picture under this equation

$$\left(-\frac{\nabla^2}{2} + V_{ext}(r) + V_H(r) \right) \phi_i(r) + \int dr' \Sigma(r, r') \varepsilon_i^{GW} \phi_i(r, r') \varepsilon_i^{GW} \phi_i(r), \quad (3.22)$$

which looks very similar to the KS equation that was previously introduced

$$\left(-\frac{\nabla^2}{2} + V_{ext}(r) + V_H(r)\right) \psi_i^{LDA}(r) + V_{xc}^{LDA}(r) \psi_i^{LDA}(r) + \varepsilon_i^{LDA} \psi_i^{LDA}(r) \quad (3.23)$$

From Eq. (3.22) the self-energy (Σ) is a non-local and energy-dependent operator, therefore, not a Hermitian operator. To solve the Eq. (3.22), we can use the perturbation theory by assuming the wavefunctions are the same as those in Eq. (3.23). We can then correct DFT-LDA eigenvalues by using the first-order perturbation treatment.

$$\varepsilon_i^{GW} = \varepsilon_i^{LDA} + \langle \psi_i^{LDA} | (\Sigma(r, r', \varepsilon_i^{GW}) - V_{xc}^{LDA}(r)) | \psi_i^{LDA} \rangle \quad (3.24)$$

The GW eigenvalues can be obtained by applying a Taylor expansion of $\Sigma(r, r', \varepsilon_i^{GW})$ around ε_i^{LDA} to Eq. (2.24). Then we get

$$\varepsilon_i^{GW} = \varepsilon_i^{LDA} + Z_i \langle \psi_i^{LDA} | \Sigma(r, r', \varepsilon_i^{LDA}) - V_{xc}^{LDA}(r) | \psi_i^{LDA} \rangle, \quad (3.25)$$

where $Z_i = \left(1 - \langle \psi_i^{LDA} | \frac{\partial}{\partial \varepsilon} \Sigma(r, r', \varepsilon_i^{LDA}) | \psi_i^{LDA} \rangle\right)^{-1}$ is a quasiparticle renormalization factor.

Finally, we get the energy shift of the one-particle excitations from the **KS** eigenvalues and also their imaginary parts from Eq. (3.25). By Fourier transforming Eq. (3.21) over time, we obtain the self-energy, Σ , as

$$\Sigma(r, r', \varepsilon) = \frac{i}{2\pi} \int d\varepsilon' e^{-i\delta\varepsilon'} G(r, r', \varepsilon - \varepsilon') W(r, r', \varepsilon') \quad (3.26)$$

G can be approximated by the independent particle G_0 , from the so-called one-shot G_0W_0

$$G^0(r, r', \varepsilon) = \sum_i \frac{\psi_i^{LDA} \psi_i^{LDA*}}{\varepsilon - \varepsilon_i^{LDA} \pm i\eta} \quad (3.27)$$

The screened Coulomb interaction W can be estimated as W_0 by using the Random Phase Approximation (RPA).

$$W^0 = v\varepsilon^{-1} = v(1 - vP)^{-1} \quad (3.28)$$

Here, W^0 is a schematic notation. We should always remember that Eq. (3.28) actually represents an integral equation, here v is actually $v(I, 2)$ and W is $W(I, 2)$ etc. We also switch to the frequency or energy domain from time domain here so that P can become a dynamic

polarization $P(r, r', \omega)$. All quantities are expanded in a basis set so that these become matrix equations which can practically be solved. Although the GW approximation offers a great improvement for the KS theory for calculating excitation energies, it is still not always sufficiently accurate. The results depend on other approximations made such as pseudopotentials to describe the interaction between valence and core electrons. Moreover, GW is applied as a perturbation theory, therefore its accuracy depends directly on the starting point. As a result, although the more accurate all-electron band structure methods are used in the calculation the corrections to band gaps still tend to be too small.

3.4 Quasiparticle Self-consistent GW Approximation (QSGW)

Since the GW approximation is usually applied as a perturbation theory, its result depends directly on the accuracy of the starting point. Therefore, the starting point is crucial to the success of the calculation. In the QSGW formalism, the best starting point is obtained by redefining an effective independent particle Hamiltonian $H^0 = H^{LDA} + \Delta V_{xc}$ with a correction to the exchange correlation potentials which must somehow be extracted from the self-energy.

Van Schilfgaarde et al. (van Schilfgaarde et al., 2006) has proposed the solution to this by deriving the self-energy as a functional of G^0 and initially extracting G^0 from $V_{eff} = V_{ext} + V_H + V_{xc}^{LDA}$ and then determining $V_{eff}^{GW} = V_{ext} + V_H + \Sigma(G^0)$. V_{eff}^{GW} is then mapped back to V_{eff} in order to complete the self-consistency circle of the effective potential. This approach is equivalent to the requirement that the eigenvalues of Eq. (2.22) become as close as possible to those of Eq. (3.23) with the $\Delta V_{xc} = V_{xc}^{QSGW} + V_{xc}^{LDA}$ added to the potential. A non-local exchange-correlation potential shown in Eq. (2.29) is extracted from the self-energy,

$$V_{xc}^{QSGW} = \frac{1}{2} \sum_{ij} |\psi_i\rangle R \left[\sum_{ij} (\mathcal{E}_i) + \sum_{ij} (\mathcal{E}_j) \right] \langle \psi_j |, \quad (3.29)$$

where ψ are the one-electron KS eigenstates and R means the real part.

In Eq. (3.25), only the diagonal matrix elements of the self-energy are needed, while in Eq. (3.29) off-diagonal elements are also required. This is important to the success of QSGW because it allows the states in the presence of the new potential to be mixed up. In other words, not only the eigenvalues but also the eigenstates of the H_0 will be adjusted although this leads to the instabilities for high energy states. However, this problem can be fixed by approximating the self-energy by a diagonal approximation above a certain cut-off (E_{cut}).

QSGW has demonstrated a lot of success, for example, in a series of studies by van Schilfgarde and Mark (van Schilfgarde et al., 2006; Kotani et al., 2007). Its results in band gaps has shown excellent agreement for most semiconductors. QSGW gives reasonable results even for strongly correlated materials like transition metal oxides and rare earths although it is not able to explain fully the spectral functions of these complex materials. However, there is still a small systematic error, it tends to slightly overestimate the band gaps when compared to experiments. This is believed to be caused by the under-screening from the RPA. The correction can be easily done by scaling the final ΔV_{xc} by about 80 % as obtained empirically by comparing QSGW with experiment for a wide variety of semiconductors (Aryasetiawan et al., 1998). This correction is referred as the 0.8Σ approximation. In this thesis, we apply this method to InN as will be discussed in Chapter IV.

3.5 Full-Potential Linear Muffin-Tin Orbital Method (FP-LMTO)

There are two major methods to solve the single-particle Schrödinger equation of a periodic system, i) variational method and ii) multiple scattering methods. For the variational method, the system eigenfunctions are expanded in terms of a fixed set of basis functions such as plane wave basis set as implemented in VASP code which is also used in our thesis and will be discussed in the next topic. The method usually uses a pseudopotential

approximation to describe the interaction between valence and core electrons which only uses small number of functions as the basis set. For the multiple scattering method, the potential is usually geometrically approximated by a muffin-tin potential. To gain highly accurate results, the former requires a large number of simple basis functions while the latter requires a high computational effort since the new matrix eigenvalue problem is more complicated. However, the Linear Muffin-Tin Orbital (LMTO) (Methfessel et al., 2000) combines the advantages of both methods by using basis sets derived from the scattering method which leads to very small basis sets, therefore, less time consuming.

In FP-LMTO, the basis sets are defined differently for two main regions. The space consists of two regions, i) “muffin-tin spheres” which surround the atomic sites and ii) the interstitial region between the spheres. Each muffin-tin orbital is constructed from the solution of the Schrödinger equation for its region. All the MTOs are given by the product between a spherical harmonic and a radial function centered on each of the atomic sites. The region outside the sphere, the solution is a decaying Hankel function. This is referred to as the envelope function. Inside the sphere, which the orbital is centered, the solution is replaced by a matching linear combination of the solution of the Schrödinger equation at some chosen energy ϕ and its energy derivative $\dot{\phi}$. The tail of the envelope function is re-expanded in spherical harmonics about any site that the tail intersects another sphere and is matched to a linear combination of ϕ and $\dot{\phi}$. Overall, the function is continuous and differentiable everywhere. It is constructed out of the solutions of the Schrödinger equation for the muffin-tin potential in each region, although the energy might not be correct. The functions can describe the solutions of the eigenstates of energy ε_j in some energy range where the partial waves can still be expanded in the form of Taylor expansion. The eigenstates will then be a superposition of these muffin-tin orbitals. The matrix elements of the Hamiltonian and the overlap matrices are calculated while the periodic boundary conditions are also taken into account by taking Bloch sums over the lattice vectors. To

obtain the eigenvalues and eigenvectors, the matrix is then diagonalized. After that the new charge density can be constructed by integrating over the Brillouin zone and , finally, the KS equations can be solved self-consistently. The integral can be easily calculated over the spheres because we already know how the Hamiltonian acts on the ϕ and $\dot{\phi}$ but the integrals over the interstitial region are more difficult because the shapes are more complicated. Therefore, to make the calculation faster, we must let the spheres slightly overlap so they fill in all the space and thus the interstitial region disappears and no longer a problem. This scheme is so-called atomic sphere approximation (ASA). However, this method is fast but not sufficiently accurate for total energy calculations in structures with low-symmetry.

The Full-Potential Linear Muffin-Tin Orbital (FP-LMTO) was later introduced (Kotani et al., 2010) in order to avoid the restrictions of the muffin-tin shaped potential. In FPLMTO, the muffin-tin is only used to construct the basis sets, but the crystal potential shape is not approximated. Inside each muffin-tin sphere, the Schrödinger equation is solved numerically. Since the potential is very close to spherical the calculation is rather simple. The non-spherical terms are then included later. For the interstitial region, the envelope function is improved from the original LMTO method by replacing the Hankel function by a smoothed Hankel function. Outside the spheres, the potential is flat and the solution of the radial Schrödinger equation is a standard Hankel function with a singularity at the origin. In fact, there is the attractive nuclear potential outside the muffin-tin radius so the correct wavefunction bends over outside the muffin-tin radius instead of having the singularities. Then the smooth Hankel functions were introduced by Methfessel and the others (Bott et al., 1998) as a convolution of Gaussians and standard Hankel functions. Its shape can be controlled by two parameters, the function decay constant (κ) and the smoothing radius (R_{sm}). R_{sm} is used to determine how much the function is bent. There still remains one problem for FP-LMTO method which is the difficulty in calculating the matrix elements of the Hamiltonian over the interstitial region. To overcome this problem all the required

quantities need to have dual representations including wavefunctions, charge density and potential. In FP-LMTO, the muffin-tins and interstitial region are not completely separated, but instead the smooth Hankel functions is applied to smooth out the connection between the two regions. The function inside the sphere is corrected by expanding the smooth function inside the spheres in spherical harmonics times a radial function. The low angular momentum components of this function are replaced by the actual rapidly varying functions obtained from the radial solutions of the Schrödinger equation of the true potential inside the spheres. Finally, we can represent the charge density, $n(\mathbf{r})$, as a combination of a smooth function throughout the unit cell and contributions from inside the muffin-tin spheres as follows:

$$n(\mathbf{r}) = \tilde{n}(\mathbf{r}) + \sum_{R,L} \{n_{R,L}(\mathbf{r}) - \tilde{n}_{R,L}(\mathbf{r})\}, \quad (3.30)$$

where $\tilde{n}(\mathbf{r})$ and $\tilde{n}_{R,L}(\mathbf{r})$ are the smooth charge densities throughout the unit cell and inside the muffin-tin spheres respectively, which are varying slowly. $\tilde{n}_{R,L}(\mathbf{r})$ is a true density inside the muffin-tin sphere which is varying rapidly near the core. This allows us to find the corresponding electrostatic potential rapidly through the Fourier transform method (FFT). This method also gets rid of the disadvantages of previous implementations of FP-LMTO, such as the need for high angular momentum expansions. The awkward shapes of interstitial regions also disappear and the matrix elements are easier to calculate because no cross terms between the smooth and the intra-sphere parts. For these reasons the method is highly accurate and very competitive to the so called linearized augmented plane wave (LAPW) method which is considered as one of the most accurate methods for band structure calculations. More detail on GW and GSGW implementations within FP-LMTO can be found in Ref. (van Schilfgaarde et al., 2006; Kotani et al., 2007).

3.6 Plane wave basis sets and Bloch's theorem

To calculate infinite number of interacting electrons in the electric field of an infinite number of ions. Generally, there are some problems in calculation of the system with infinite number of interacting ions, such as, the wave function has to be calculated for each of the electron for the entire system which will then be extended over the space of solid, therefore the basis set will be infinitely large. However, in the Bloch's theorem, it is assumed that at ϕ K the ions are arranged in a periodic structure and hence the external potential from the electrons will also be periodic which means that the wave functions of the infinite crystal can be expressed in terms of wave functions at reciprocal space vectors of a Bravais lattice. By having periodicity in the crystal we are able to reduce the number of one-electron wave functions needed to be calculated down to only the number of electrons in the unit cell. The Bloch's wave functions can be expressed as

$$\Psi_{n,k}(\mathbf{r}) = u_{n,k}(\mathbf{r}) e^{i\mathbf{k}\cdot\mathbf{r}}. \quad (3.31)$$

$u_{n,k}(\mathbf{r})$ can also be expressed by the expansion of plane waves whose wave vectors are reciprocal lattice vectors of the crystal as follows

$$u_{n,k}(\mathbf{r}) = \sum_{\mathbf{G}} c_{\mathbf{G}nk} e^{i\mathbf{G}\cdot\mathbf{r}}, \quad (3.32)$$

where \mathbf{G} is the reciprocal lattice vector. By plugging Eq. (3.32) back into Eq. (3.31), the electronic wave functions can now be written as

$$\Psi_{n,k}(\mathbf{r}) = \sum_{\mathbf{G}} c_{\mathbf{G}nk} e^{i(\mathbf{G}+\mathbf{k})\cdot\mathbf{r}}. \quad (3.33)$$

The infinite number of electrons for the whole system can then be mapped into the problem of expressing the wave function in the reciprocal space vectors only within the first Brillouin zone. Though Fourier series can be expanded into infinite number of terms, the terms at higher energies have little effect on the results and can be cut out by introducing the energy cutoff. The value of the energy cutoff depends on elements in the system being study. Therefore, only the plane waves with wave vectors smaller than $\mathbf{G} + \mathbf{k}$ will be included.

3.7 **k-point sampling in VASP code**

In first-principles calculations, the wave functions must be calculated for infinite number of k -points in the Brillouin zone. In practice, electronic states are only calculated for a set of representative k -points which are determined by the shape of the Brillouin zone. We can obtain the electronic states at nearby k -points by interpolating between the nearby sampling k -points. By this approximation, the electronic states can be calculated at a finite number of k -points which can finally determine the total energy of the crystal. In the calculation of $\text{Bi}(\text{Ti}_{0.5}\text{Mg}_{0.5})\text{O}_3$ by VASP in chapter V, we use the sampling method proposed by Monkhorst and Pack (Monkhorst et al., 1976).

3.8 **Pseudo potential in VASP code**

Generally, the Schrödinger equation for the homogeneous non-interacting electron gas has the solution which may be expressed as a plane wave function,

$$\Psi_{\mathbf{k}}(\mathbf{r}) = Ae^{i\mathbf{k}\cdot\mathbf{r}}, \quad (3.34)$$

where \mathbf{k} is the wave vector. To describe the rapid oscillating wave functions of core electrons accurately, the wave function has to be expanded with a large basis set of plane waves. However, this may not be necessary since the physical properties of solids solely depend on the valence electrons, therefore, pseudo potential can be used instead of the actual potential. Only the valence electrons are explicitly considered in pseudo potential method. This removes the rapid oscillation near the core region, however the final results are equivalent but much fewer plane waves are required in the calculation. As a result, time consuming and computational cost are much less than the original method. The schematic plot of pseudo and true potentials and wave functions are shown in Figure 3.1.

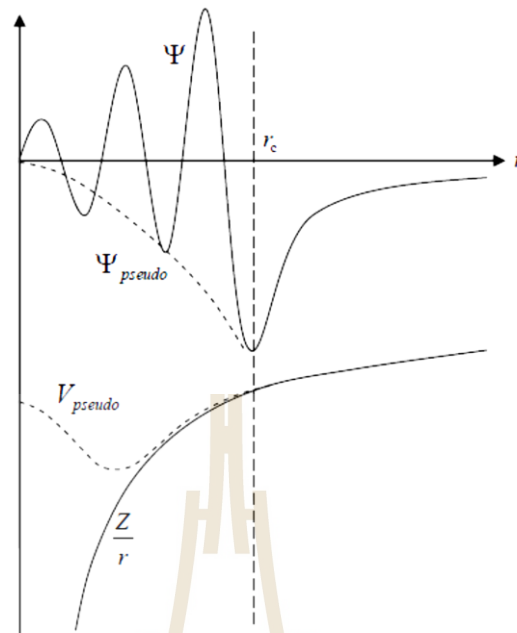


Figure 3.1 A schematic plot between the pseudo potential and pseudo wave function with respect to the distance, r , from the ionic nucleus. The dashed lines represent the corresponding pseudo wave function and pseudo potential inside the core radius.

In pseudo potential, the charge within the core radius must be the same as that of the true potential wave functions, this is known as norm-conservation (Hamann et al., 1979). The pseudo potential must be able to reproduce the proper phase shifts for the scattering at the core level. The pseudo potential must be non-local with projectors for different angular momentum components. In another word, different angular momentum states have different phase shifts. The pseudo potential can be represented using the form (Kleinman et al., 1982) as follows:

$$V = V_{loc} + \sum_{l,m} (V - V_{loc}) \hat{P}_{l,m}, \quad (3.35)$$

where $\hat{P}_{l,m}$ are the projectors which project the electronic wave functions onto the eigenfunctions of different angular momentum states. The choice of V_{loc} is arbitrary and if it is made equal to V_l , then the corresponding set of angular momentum projectors are not required. The computational time required to evaluate the non-local potentials is

proportional to the size of the system. Later, King-Smith (King-Smith et al., 1991) carried out the calculations in real-space and was able to reduce the computational time to the order of the system size squared.

3.9 The Hellmann-Feynman theorem

According to Hellmann-Feynman theorem, if we define as λ a parameter in the Hamiltonian and $\psi(\lambda)$ as an eigenfunction. The derivative of energy with respect to λ can be written as

$$\begin{aligned}\frac{\partial E}{\partial \lambda} &= \frac{\partial}{\partial \lambda} \langle \psi | \hat{H} | \psi \rangle = \left\langle \frac{\partial \psi}{\partial \lambda} | \hat{H} | \psi \right\rangle + \langle \psi | \frac{\partial \hat{H}}{\partial \lambda} | \psi \rangle + \langle \psi | \hat{H} | \frac{\partial \psi}{\partial \lambda} \rangle \\ \frac{\partial E}{\partial \lambda} &= E \left\langle \frac{\partial \psi}{\partial \lambda} | \psi \right\rangle + \langle \psi | \frac{\partial \hat{H}}{\partial \lambda} | \psi \rangle + E \left\langle \psi | \frac{\partial \psi}{\partial \lambda} \right\rangle = E \frac{\partial}{\partial \lambda} \langle \psi | \psi \rangle + \langle \psi | \frac{\partial \hat{H}}{\partial \lambda} | \psi \rangle \\ \frac{\partial E}{\partial \lambda} &= \langle \psi | \frac{\partial \hat{H}}{\partial \lambda} | \psi \rangle\end{aligned}\quad (3.36)$$

This means that we can calculate a derivative of the total energy E of a system with respect to a parameter λ can from derivative of the operator \hat{H} . And if λ is R, we can calculate the forces by applying the Hellmann-Feynman theorem as follows:

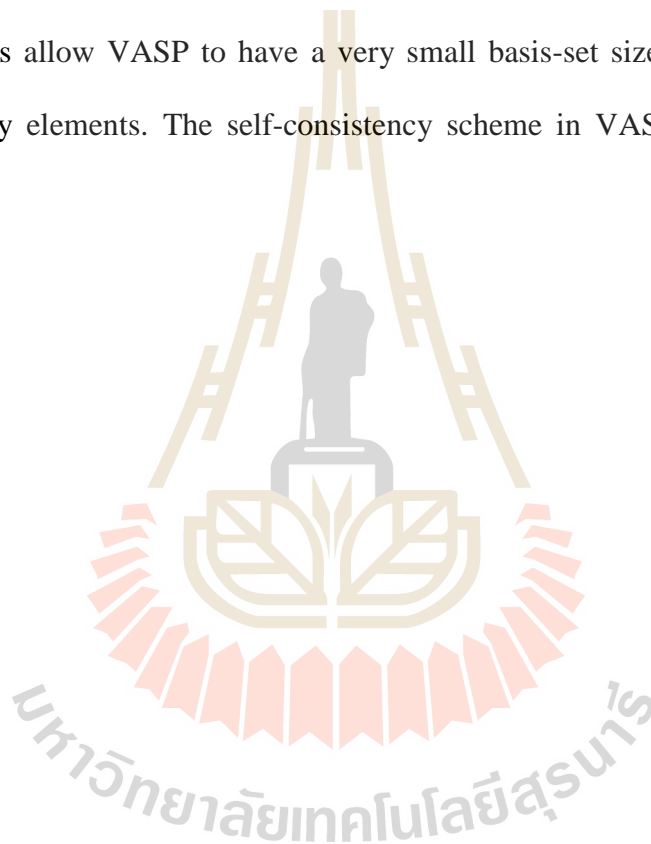
$$\mathbf{F}_i = -\frac{\partial E}{\partial \mathbf{R}_i} = -\int d\mathbf{r} n(\mathbf{r}) \frac{\partial V_{ext}(\mathbf{r})}{\partial \mathbf{R}_i} - \frac{\partial E_{II}}{\partial \mathbf{R}_i} = -\left\langle \psi | \frac{\partial \hat{H}}{\partial \mathbf{R}_i} | \psi \right\rangle - \frac{\partial E_{II}}{\partial \mathbf{R}_i}, \quad (3.37)$$

where E_{II} is the electrostatic nucleus-nucleus (or ion-ion) interaction.

3.10 Electronic ground state calculations implemented in VASP code

As mentioned before, there are several well-known codes that are widely used in first-principles calculation to solve the Kohn-Sham equation which give the electronic ground state energy and electronic wave functions as results. In this thesis we use FP-LMTO (Jarlborg et al., 1976; Jarlborg et al., 1977) and VASP (Kresse et al., 1994; Kresse, G. et al., 1996) codes. The algorithms implemented in VASP codes mostly use efficient iterative matrix-diagonalization schemes such as the conjugate gradient scheme (Teter et al., 1989;

Bylander et al., 1990) and a residual minimization scheme-direct inversion in the iterative subspace (RMM-DIIS) (Pulay, 1980; Wood et al., 1985). To mix the original and new electronic charge density during the self consistency calculation. To mix the original and new potential during the self-consistency calculation VASP uses the Broyden/Pulay mixing scheme (Pulay, 1980; Johnson, 1988). For potentials, the Vanderbilt's ultra-soft pseudo potentials (US-PP) or project augmented wave (PAW) method is used. These implementations allow VASP to have a very small basis-set size even for the transition metals or heavy elements. The self-consistency scheme in VASP code is illustrated in Figure 3.2.



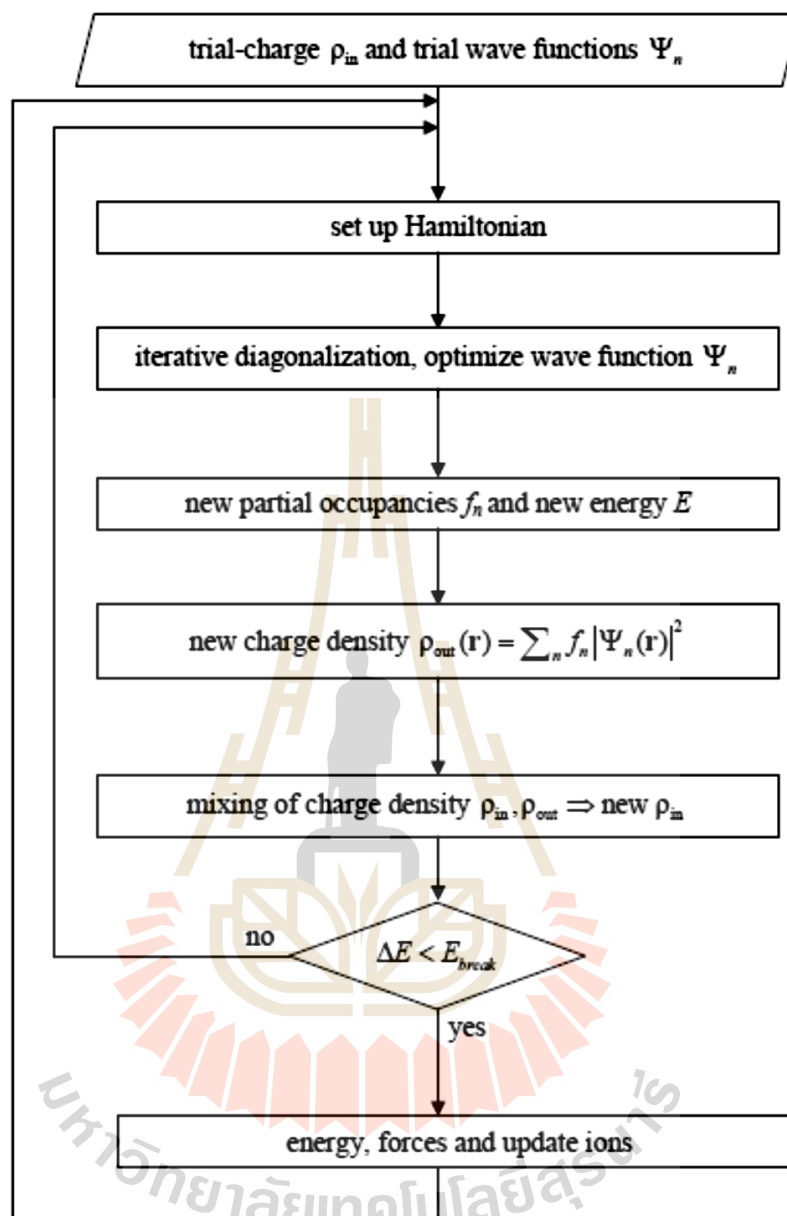


Figure 3.2 The self-consistency scheme used in the VASP codes.

For more details on VASP please check the manual of VASP (Kresse et al., 2014).

CHAPTER IV

RXES OF GRAPHENE

This chapter is based on our published work (Zhang et al., 2012) that co-authored with L. Zhang and the others who provided the experimental data.

4.1 Introduction

The recent discovery of graphene has attracted intense research interest due to three main extraordinary properties including: 1) high carrier mobility (Novoselov et al., 2004), 2) high mechanical strength (Lee et al., 2008), and 3) tuneable band gap (Han et al., 2007). There are tremendous efforts on trying to grow graphene through several methods, for example, micromechanical cleavage of graphite (Novoselov et al., 2004), annealing of a SiC single crystal at high temperature (Berger et al., 2006), and chemical vapour deposition (CVD) epitaxial growth on different metallic surfaces. (Dedkov et al., 2008; Li et al., 2009). However, detailed understanding of the electronic structure for both conduction and valence bands of graphene has not been paid much attention to. This can be the basis to better understand the transport properties of graphene and improve the performance of graphene-based electronic devices in the future.

Powerful x-ray techniques including x-ray-absorption spectroscopy (XAS), x-ray emission spectroscopy (XES), and resonant inelastic x-ray scattering (RIXS) have been employed to investigate carbon allotropes (Ma et al., 1992; Ma et al., 1993; Carlisle et al., 1995; Jinghua et al., 2000). XAS and XES provide angular momentum and site resolved partial density of states (PDOS) through the matrix elements coupling between the core-hole wave function and empty states for XAS, and filled states for XES. In RIXS, one looks at

how the XES spectra are varied as a function of the XAS excitation energy. As mentioned in chapter III, the two processes are viewed as one resonant scattering process with a hole in the valence band and electron in the conduction band without a core hole in the final state. The emission intensity is contributed by the resonant transition between two band states at the same k point (Kotani, Akio et al., 2001) which means that the crystal momentum is conserved. This leads to the band structure mapping which has been applied to various materials: graphite (Skytt et al., 1994; Carlisle et al., 1995; Sokolov et al., 2003), diamond (Ma et al., 1992), C60 (Guo et al., 1995), C70 (Guo et al., 1995), and SiC (Lüning et al., 1997). Since graphene has unique properties from being single layer, it is not yet clear how the core-hole excitonic localization effect from x-ray absorption will influence its RIXS process. Is the intermediate state, which contains an electron in the conduction band and a core hole, affected by the exciton localization effect? Would the translational symmetry be broken? Or is RIXS free from such an effect because in the final state there is no core hole? (Brühwiler et al., 1995; Brühwiler et al., 1996; Carlisle et al., 1996). It is interesting to see if graphene will have similar behaviour as observed in broadband metals.

In this work, we performed the band structure calculations of graphene using the full-potential linearized muffin-tin orbital (FP-LMTO) method (Methfessel et al., 2000) and the k -conserving RXES spectra of graphene based on the Kramers-Heisenberg formulation including the relevant matrix elements (Eisebitt, 2000; Shirley, 2000; Preston et al., 2011). More detail of this method can also be found in Chapter II. To verify our calculation, the calculated RXES spectra is compared to the experimental ones from our collaborator who performed all the necessary measurements, also including XAS and XES. A key note in this work is the comparison between theory and experiment for RXES spectra of graphene which has never been done in other systems. In graphene, the presence or absence of the core hole in the final state of these XAS and XES need to be taken into account and a shift in the alignment of the RXES spectra is required.

4.2 Experimental methods

The experiments were performed, by our collaborators (Zhang et al., 2012), on the undulator beamline 7.0.120 at Advanced Light Source, Lawrence Berkeley National Laboratory. The XAS measurements were performed in total-electron-yield mode from a sample drain current with the resolution at 0.1 eV. The emission spectra were measured with a grazing incident grating spectrometer mounted with its optical axis perpendicular to the incident x-ray beam and in the direction of the polarization vector. The resolution of both the monochromator and spectrometer were set to 0.45 eV for the XES and RIXS measurements. All the emission spectra were acquired in the same time scale and normalized to unity for the strongest inelastic emission feature in each spectrum. Single-layer graphene on an SiO₂ substrate was prepared following the method described in Ref. 6. The microstructure and quality of the graphene films were characterized by Raman spectroscopy (ISA Groupe Horiba) using a 488-nm wavelength laser.

4.3 Computational methods

The band structure of graphene is calculated using the full-potential linearized muffin-tin orbital (FP-LMTO) (Methfessel et al., 2000) method in the local-density approximation. The unit cell consists of 2 Carbon atoms. The single layer of graphene is accomplished by defining the c axis as 5 Bohr radius which is long enough so that the calculation won't be affected when the unit cell is repeated. We use a k-point set of 20 x 20 x 1. The k-conserving parts or coherent RIXS spectra were calculated in the Kramers-Heisenberg formalism (Preston et al., 2011) as described in Chapter II.

4.4 Results and discussions

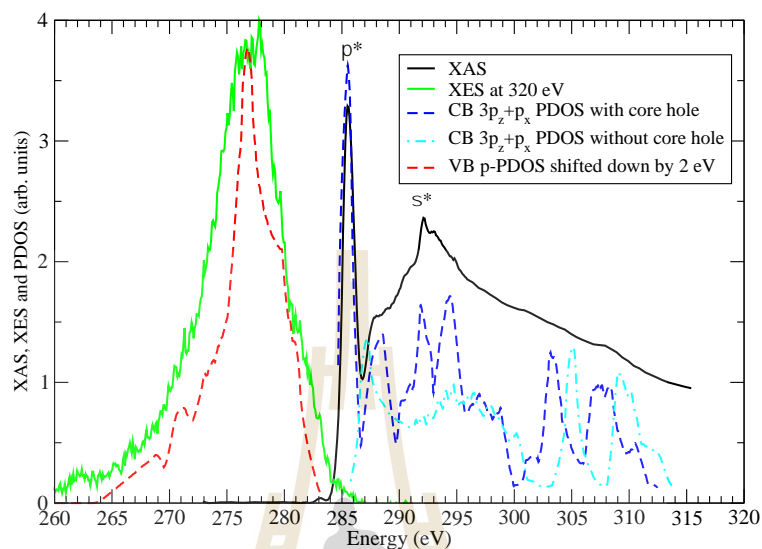


Figure 4.1 XAS and XES spectra compared to theory; see text for details. (Zhang et al., 2012)

In Figure 4.1, we compare the XAS and incoherent XES (measured with 320 eV excitation) with various theoretical models. According to the widely accepted final state rule, the XAS spectrum should reflect the partial density of states in the presence of the core-hole. We therefore carried out calculations in a $2 \times 2 \times 1$ supercell with a core hole included on the central atom. This significantly changes the local density of states compared to the unperturbed graphene and pulls a bound state out of the conduction band. This can be seen in Figure 4.2, which shows the PDOS in the supercell on an atom with core hole and without core hole compared with the perfect crystal to illustrate their alignment. One can see that even the nearest neighbours of the core-hole atom still have some PDOS weight in the bound state, so the core hole not only affects the atom itself but also its neighbours.

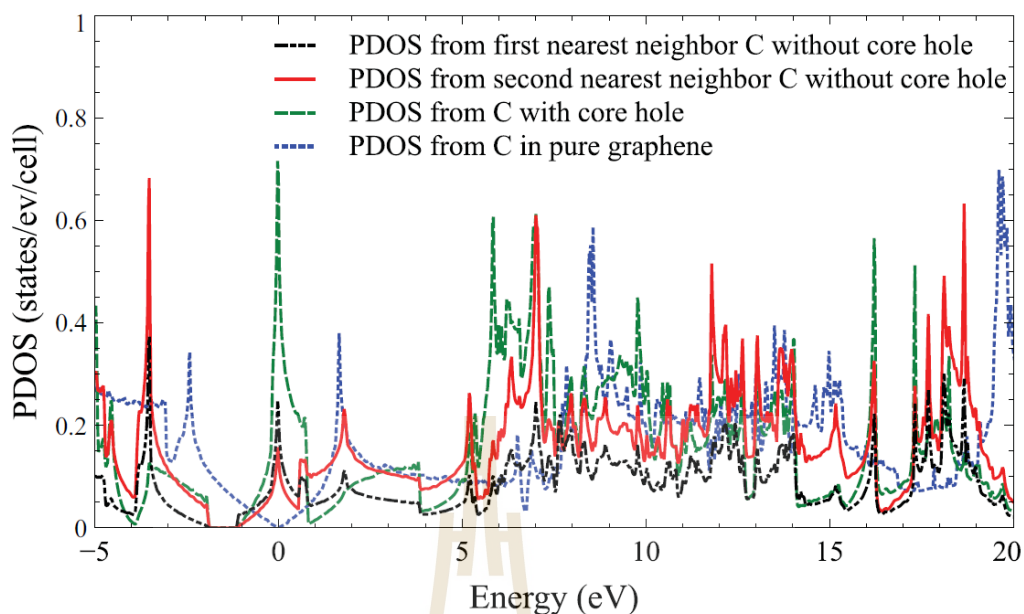


Figure 4.2 Carbon p-like PDOS in graphene; core-hole effect. (Zhang et al., 2012)

Because the incident X-ray beam is at 60° from the normal and is s-polarized, the XAS spectrum can be modeled by $(\frac{3}{4}p_z + \frac{1}{4}p_x)$ PDOS. This conduction band PDOS on the atom including the core-hole is shown by the blue dashed line in Figure 4.1 with the bound state peak (or core-exciton) aligned with the experimental π^* peak. A slight broadening has been applied to the calculated spectrum. The corresponding weighted PDOS from a carbon without the core-hole in perfect crystal graphene is shown as the dash-dotted cyan line. We can see that the theory with core-hole much better accounts for the experimental line shape, in particular the shape of the onset beyond the bound state up to about 290 eV and the location of the σ^* peak. Even peaks up to about 310 eV can be recognized as weak features in the experiment. To further bring theory and experiment in coincidence an increasing broadening with increasing energy and an accumulative background would have to be added but we prefer not to get into modeling these aspects. The important point is that the π^* peak of the unperturbed graphene, which corresponds to a saddle point at M is shifted up from the bound state by about 1.7 eV. Figure 4.3 shows how the density of states is related to the band structure in graphene.

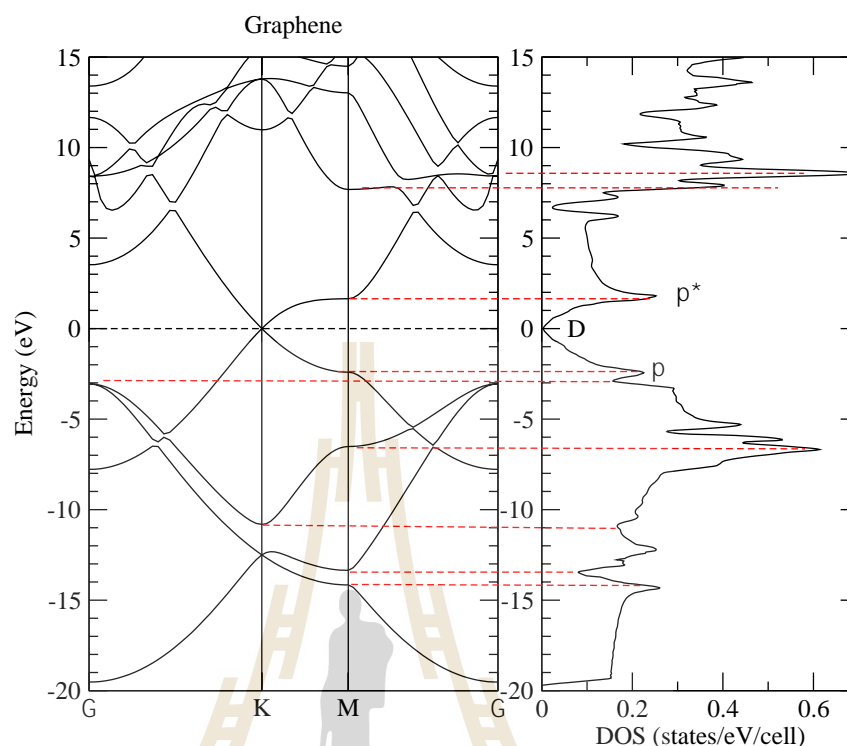


Figure 4.3 Band structure and DOS of graphene (Zhang et al., 2012)

Now returning to the XES in Figure 4.1, according to the final state rule, the latter should be represented by the PDOS without core-hole. Moreover, because no polarization sensing is done in the XES, we can directly compare with the total p-like PDOS without relative weighting of the p_z and p_x . We found that we need to shift down the calculated spectrum by about 1.7 eV in order to align this with the XES spectrum. The explanation for this is that the core-hole, which pulled down the density of states by about 1.7 eV, is not present in the final state of XES and thus to undo this core-hole shift the experimental spectrum should be shifted up by 1.7 eV. We can identify the Dirac point as occurring at 284.7 eV in the XAS spectrum since we know precisely where the Dirac point in the band structure is located relative to the π^* peak of the PDOS without core hole, and this is in fact very close to the position of the π^* bound state with core hole.

Now we are ready to analyze the coherent RXES spectra with the calculations. The RXES spectra are calculated according to the Kramers-Heisenberg formula.

$$\left[\frac{dS}{d\Omega d\omega_2} \right]_{ab} \propto \sum_k \sum_{cv} \left| \frac{\langle ck | p_a | s \rangle \langle s | p_b | vk \rangle}{(E_{ck} - E_s - \omega_1 - i\Gamma/2)} \right|^2 d(\omega_1 - \omega_2 - E_{ck} + E_{vk}) , \quad (4.1)$$

where $|ck\rangle$ represents the conduction band and $|vk\rangle$ the valence band states at k-point k, $|s\rangle$ represents the s-like core-state, p_α represents the momentum operator for the incoming beam and p_β the momentum of the emitted beam polarization, ω_1 and ω_2 are the energies of the X-ray absorbed and emitted respectively. E_{ck} , E_{vk} , represent the energies of the conduction to which the electron is excited, and the energy of the valence band from which it drops back to the core hole, whose energy is E_s . The energy conservation for the difference between X-ray emission and absorption with a vertical interband transition is expressed through the delta function. The resonance of the core-hole to the conduction band transition with the XAS energy can be explained through the denominator in the matrix element factor with Γ representing the core-hole lifetime. The energies in the conduction band are measured relative to the Dirac point as our excitation energies and also measure the RXES relative to the Dirac point. According to the alignments that we have worked out above from the XAS-XES with PDOS, we may consider the spectrum at XAS energy $\omega_1 = 284.7$ eV to correspond to exciting right at the 0 energy, i.e. at the Dirac point but we should then shift the calculated spectrum up by $284.7 - 1.7 = 283$ eV as we did with the incoherent XES because the core hole is not affecting the RXES. If it were, then the periodicity and hence the k-conservation would be broken. The calculated spectra for various excitation energies are shown compared to the experimental spectra with this alignment in Figure 4.4. In other words, the above analysis allows us to determine which calculated spectrum should be aligned with which experimental spectrum and how to align their energy axes. The two differ by a 1.7 eV shift because of the core-hole effect being present in XAS but not in XES or RXES. In this comparison, the incoherent fraction was removed from the experimental spectra according

to the procedure previously mentioned, therefore, they are more precisely the CRXES.

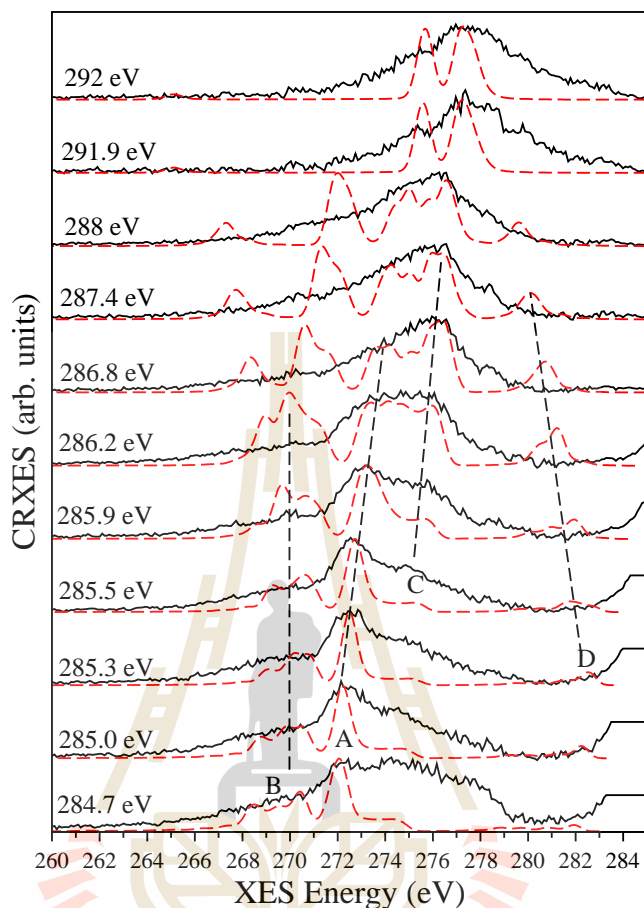


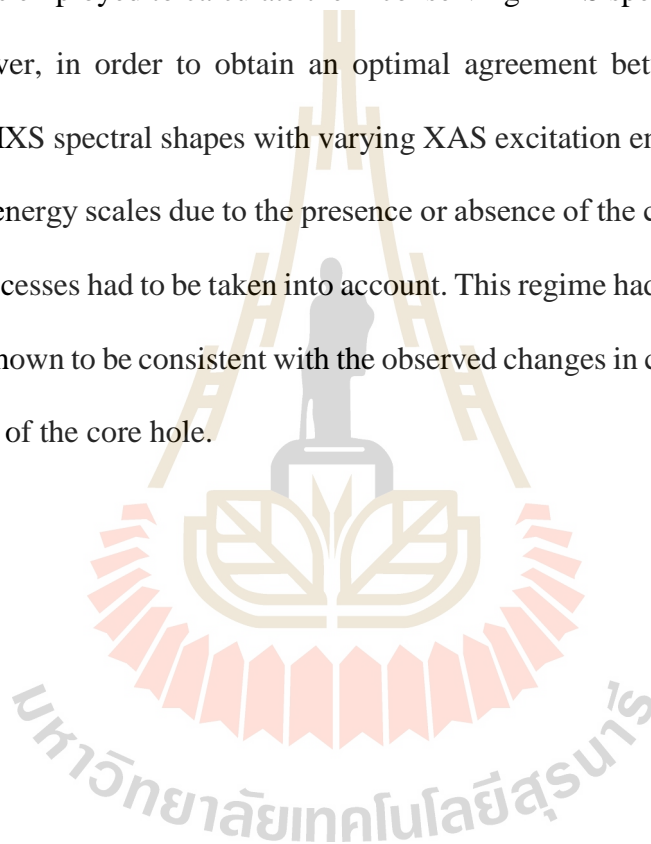
Figure 4.4 Coherent RXES spectra compared to theory (Zhang et al., 2012).

Various features are labeled with letters in the CRXES in Figure 4.4 so it is easier to follow in the discussion. The dashed line are used to guide the eye on how these features disperse with XAS energy. First, we would like to note that at low energy we essentially see emission from the σ bands only because the emitted beam is at right angles from the incoming beam, i.e. 30° from the normal and hence primarily corresponds to in-plane polarization. At low energy we are close to the Dirac point or K-point in the Brillouin zone. The density of states are very low at this point, and hence the spectral weight is low. We note that Figure. 4.4 shows calculated spectra scaled by peak height but the absolute intensity is low for the low XAS energies. So, the feature labeled A corresponds to the σ band close

to K. The fact that we see the features B below it extending down to several eV below it indicates that we pick up contributions from some range of k-points near K in the spectrum. This is related to the core-life time broadening factor in the equation. The fine structure of this peak is not resolved in the experiment but the broad shoulder extending down to 265 eV is clearly visible in all the experimental spectra. As we now increase in XAS energy we can see these features being shifted because we move away from K towards Γ and M. The lower band (feature B) moves down and the upper one (feature A) moves up. At about 285.5 a new feature C appears which disperses upward and grows in intensity. This is because we approach the M-point in the Brillouin zone. At M there is a large density of states due to a saddle point in the band structure (see Figure 4.3). The agreement between theory and experiment in terms of the shape of the spectrum is particularly good in the range 285-288 eV. The feature D in the theory corresponding to the π bands at K is not visible in the experiment because it is too close to the elastic peak and suppressed in the experiment because of the near normal direction of the outgoing beam. At higher energies the relation with the k-points becomes less clear because then the XAS energy intersects the conduction bands at various points including near Γ . The dispersion of the A, B and C features however is quite similar to that observed for graphite by (Carlisle et al., 1995) and the similarity of the overall band structure of graphite and graphene can be seen here. The experimental spectra for 284.7 -285.5 eV as excitation energy, show considerable spectral weight in the range 280-274 eV, which is not accounted for in the calculated CRXES. This may be because of imperfect subtraction of the incoherent part or may indicate sources of carbon different from pure graphene, such as defective states due to the interaction with the substrate. This could be expected to affect π -bonded states in this energy range.

4.5 Conclusion

In summary, in order to investigate the electronic properties and band dispersion of graphene the first-principles calculations were employed to analyse the XAS, XES and RIXS data. The RIXS spectra show distinct dispersive features and are interpreted as being due to the conservation of crystal momentum during the RIXS process. Kramers-Heisenberg calculations was employed to calculate the k-conserving RIXS spectra with highly accurate results. However, in order to obtain an optimal agreement between the simulated and experimental RIXS spectral shapes with varying XAS excitation energies, the shift between XAS and XES energy scales due to the presence or absence of the core hole in the final state of these two processes had to be taken into account. This regime had never been done before. This shift was shown to be consistent with the observed changes in calculated PDOS induced by the presence of the core hole.



CHAPTER V

RXES OF INDIUM NITRIDE

5.1 Introduction

In this chapter we present the results of an implementation of the Kramers-Heisenberg equation on top of a quasiparticle self-consistent- (QS) GW band-structure calculation with full consideration to the effect of dipole selection rules on the incoming and outgoing photons in different polarization and experimental geometries. This enables us to calculate spectra that can be directly compared to experiments. The present work can be considered another confirmation of the calculation methods of the RXES spectra which has been once tested on ZnO (Preston et al., 2011) which was previously reported. The theoretical results are compared to the measured wurtzite InN nitrogen K- edge RXES. We focus on wurtzite InN because of a two reasons. First it has the valence band anisotropy which can be measured by RXES method. Second, it has high electronic mobility among III-V compounds which is the high potential for use in optoelectronic applications while the conflicts of its actual electronic band structure and bandgap value still continue. For example, some groups reported a wide bandgap values of ~ 1.9 eV, according to optical measurements (Foley et al., 1986; Westra et al., 1990; Motlan et al., 2002), while others proposed that InN has a narrower bandgap of ~ 0.8 eV (Davydov et al., 2002; Liu et al., 2011). From ab-initio calculations, different values of band gaps have also been reported (Stampfl et al., 1998; Wei et al., 2003; Ahmed et al., 2005). Consequently, it is crucial to accurately determine its electronic band structure and band gap. However, due to the nature of the calculation, the result is more accurate in the area near the conduction band minimum, therefore it should be an excellent tool to apply with InN so the specific area in the Brillouin

zone, especially near the band gap region which can be compared directly to the RXES experiment, making the material another ideal test case for this calculation method.

5.2 Experimental methods:

We have measured a single-crystalline bulk InN grown by plasma-assisted molecular beam epitaxy (PA-MBE) in this study. The sample was 1 μm thick wurtzite InN(000 $\bar{1}$) films grown on c plane sapphire with a thin (30 nm) InN buffer layer. The N K - edge XAS and RXES spectra of the sample set were measured at undulator beamlines 7.0.1 at the Advanced Light Source (ALS), Lawrence Berkeley National Laboratory. The beamline is equipped with spherical grating monochromator. Emission spectra were recorded using a Nordgren-type grazing-incidence spherical grating spectrometer with the energy resolution set to 0.4 eV at the N K -edge (Nordgren et al., 1989). The energy resolution of the incoming photons was set to 0.4 eV for the resonant emission spectra measurements. At the ALS, the N K -edge XAS energy axes were calibrated using hexagonal boron nitride at 20° incidence (Moscovici et al., 1996). The calibrated photon energies of 406.8 eV, 408.8 eV and 411.8 eV were in turn used to calibrate the elastic peaks of the corresponding emission spectrum. The N K -edge XES was independently calibrated using the 2nd order diffraction L-edge of Co (Thompson et al., 2001). XAS spectra were recorded in two geometries: 20° and 70° incidence for the sample set. All the x-ray measurements appearing in this chapter were performed by our collaborators.

5.3 Computational methods

The band structure of InN is calculated using the full-potential linearized muffin-tin orbital (FP-LMTO) method with the quasiparticle self-consistent GW (QS-GW) approach (Kotani et al., 2007) starting from LDA Hamiltonian as described in Ref. (Preston et al., 2011). It is well known that this QS-GW approach, in this all-electron implementation,

slightly overestimates band gaps of most semiconductors due to the use of the random-phase approximation (RPA) of the polarizability, therefore, in practice a mixture of $0.8 V_{XC}^{QSGW} + 0.2 V_{XC}^{LDA}$ is applied to give the best agreement with the experimental band gaps. We obtain a band gap of 0.71 eV (0.65 – 0.80 from experiments) for InN, not including spin-orbit coupling or the zero-point motion corrections or exciton binding energy corrections. We use k-point mesh of 10x10x10 for LDA and 4x4x3 for QS-GW calculations. The lattice parameters used in our calculation (Vs the experiment) are 3.495(3.540), 1.62(1.61), 0.379(0.380) Angstrom for a, c/a and u respectively. The color band structures are weighted by N-p character and normalized by the maximum intensity. The k-conserving parts or coherent RIXS spectra were calculated in the Kramers-Heisenberg formalism as described in Ref. (Preston et al., 2011).

5.4 Results and discussions

5.4.1 Band structures and partial density of states (PDOS)

In InN, the band structure is obtained from GW approximations. In order to make a theoretical interpretation of the RXES spectra in InN, the band structure weighted by N- K edge character, both in the perpendicular and parallel polarization to the z directions, are generated from the band obtained from using GW approximation.

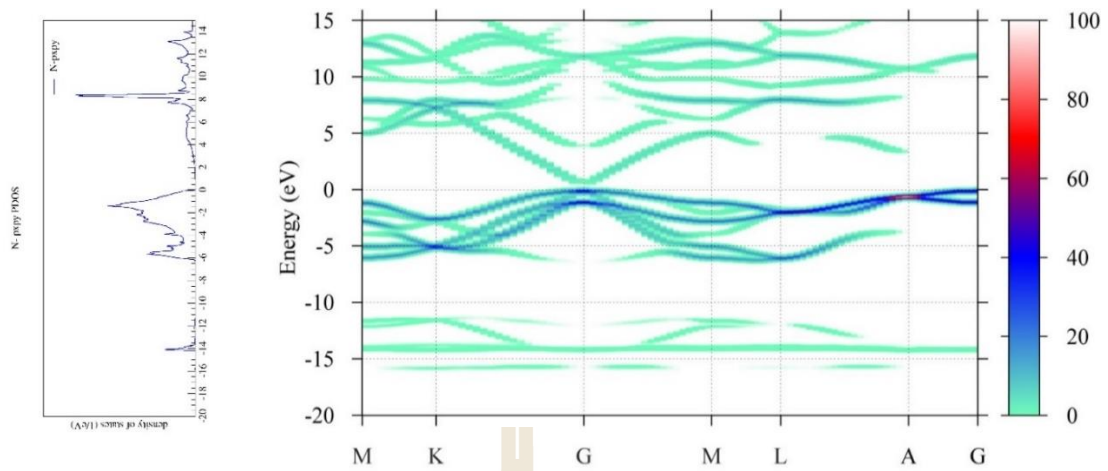


Figure 5.1 (a) N- p_{xy} PDOS and Intensity map of the calculated band structure. The intensity of the band is proportional to the p_{xy} character of the band at the point in the BZ.

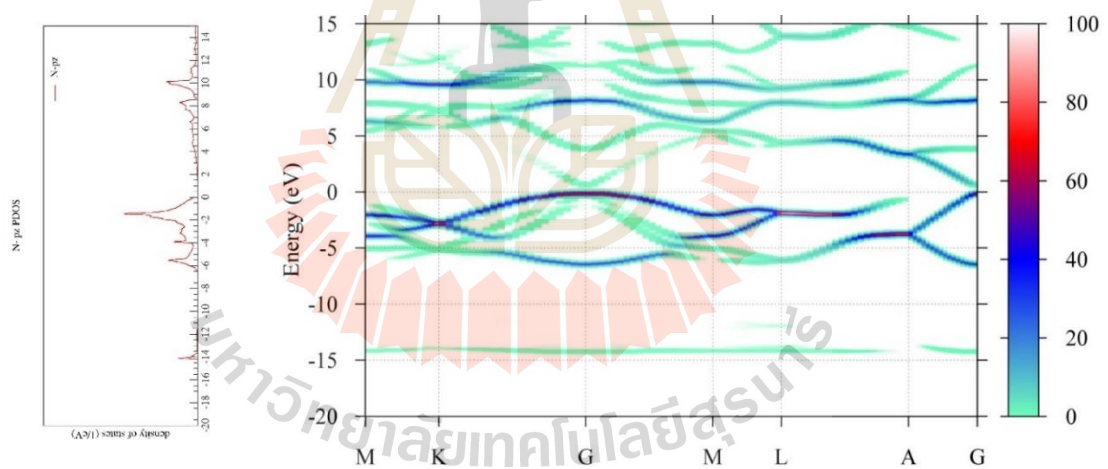


Figure 5.1 (b) N- p_z PDOS and Intensity map of the calculated band structure. The intensity of the band is proportional to the p_z character of the band at the point in the BZ.

InN band structures, weighted by p_{xy} and p_z are shown in Figure 5.1. The band gap energy from our calculation is 0.71 eV which agrees well with previous published results (Wu, 2002; Matsuoka, 2002). The bands and weightings are also in good agreement with previously published results (Piper et al., 2007). If we consider the energy range 0-5 eV

above VBM in the conduction band, this region is dominated by the first and second lowest conduction bands. In particular, the lowest conduction band has low effective mass and strong p_{xy} character near K-G-M (p orbitals lie in the K-G-M plane), p_z character along G-A (p_z orbitals point in G-A direction) and mixed character along M-L-A. For the energy range 5-10 eV, there are a couple interesting points to investigate, one near 8 eV and another near 10 eV, with significantly high DOS. The band near 8 eV is nearly horizontal and has strong p_z character near the gamma point along K-G-M and along G-A. Another band which lies at about 10 eV also has strong p_z character near K and M. Above 10 eV, the conduction becomes even less dispersive at higher energy and it is more difficult to explain the relationship between RXES spectrum and each individual band because there are more conduction bands contributing to the emission process. We now look into the valence band. The top 7 eV of the valence band is dominated by N p- like states. The valence band has strongest p_{xy} character along G-A region contributed by the two highest VB between 0 and -1 eV. P_z character dominates the top VB, and the one near -6 eV along K-G-M and the third and fourth bands along G-A. It has mixed character along M-L-A especially near L corresponding to -2 eV which will give high contribution to RXES spectra.

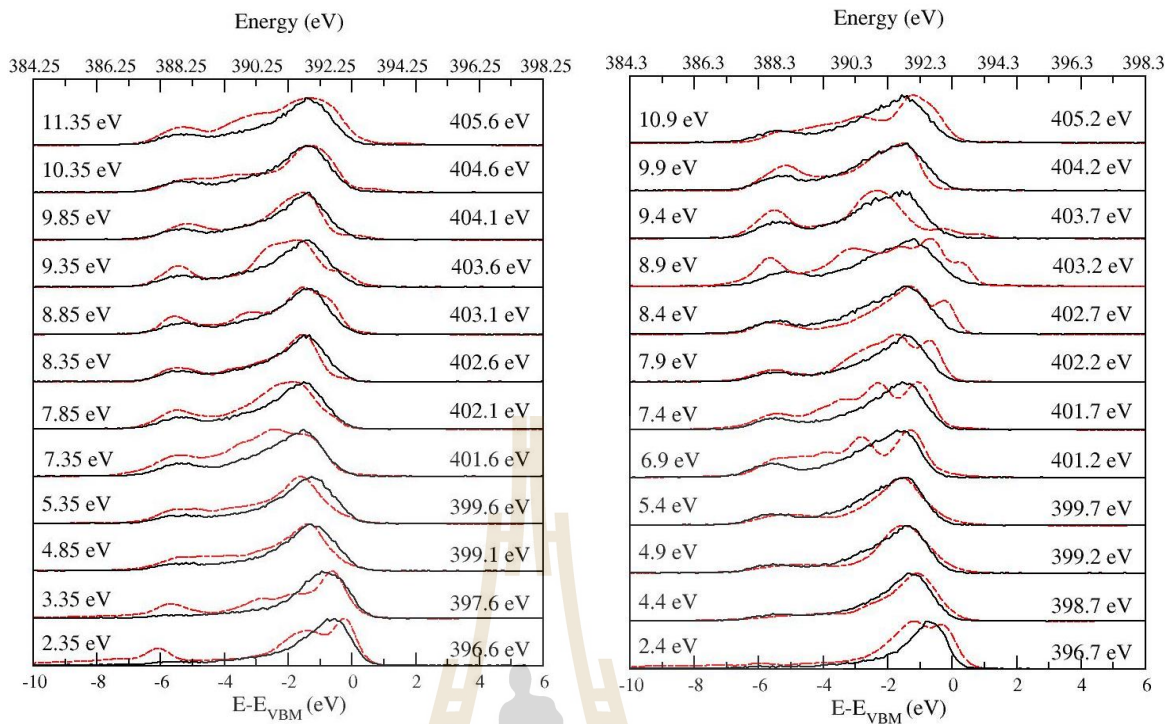


Figure 5.2 Calculated (dash red lines) and measured (solid black lines) InN (0001) CRXES at (a) near normal(20 degree) and (b) near grazing(70 degree) incidence. Each spectrum is labeled with its excitation energy; photon energy is shown on the right, and energy relative to VBM is shown on the left.

5.4.2 CRXES measurement and calculation

Figure 5.2 shows the calculated CRXES, and measured RXES for c plane wurtzite InN at near normal (NN, 20 degree) and near grazing (NG, 70 degree) incidence at different excitation energies. However, in the experiment, the k-conserving resonant contribution is only part of this measured spectra (Ma et al., 1992; Skytt et al., 1994). This contribution is maximally subtracted under the condition that the spectrum should nowhere become negative. Although the spectra are not purely coherent, the coherent part in the spectra still dominate the main peak characters at low excitation energy therefore some reasonable comparisons to our calculation can still be made.

Our calculated spectra show more detailed peak structures and dispersion effect than the experiments. This is due to difficulties in extracting the coherent fraction CRXES from the total XES which contains a significant incoherent fraction. Moreover, the measured RXES are broadened by the emission spectrometer resolution of 0.4 eV. This also happened for the case of WZ ZnO which was previously studied (Preston et al., 2011). However, some good agreement is obtained between our theory and experiment for the low photon energy region of conduction band. The agreement in qualitative trend between the experiments and the calculated spectra is obtained and can be directly related to the band dispersion. For NN measurement, incident photons couple predominantly with the p_{xy} orbitals, therefore in the absorption process we should look mainly at p_{xy} contributed conduction band. If we consider the incident energy between 0-5 eV, coherent emission should come from K-G-M part of the BZ. Above 5 eV, the bands become less dispersive especially near 8 eV that the bands are almost flat, high DOS, which we expect to see a peak with high intensity contributed from wide range of BZ, most part from near K and L in the BZ. For NG incidence, the incident photons couple to the p_z orbitals, therefore the G-A-L part of the BZ gives the most contribution to the emission for lower incident energy, 0-5 eV. For the energy range between 5-10 eV, there are a couple interesting points to investigate, one near 8 eV contributed by point G in K-G-M and A-G part, and another near 10 eV, contributed from K in M-K-G and M in G-M-L part in the BZ with significantly high DOS. For higher energy, above 10 eV, the conduction bands become less and less dispersive and larger parts of the BZ start to contribute to the CRXES. For both NN and NG, it is difficult to isolate specific contributions to the measured spectra after this point.

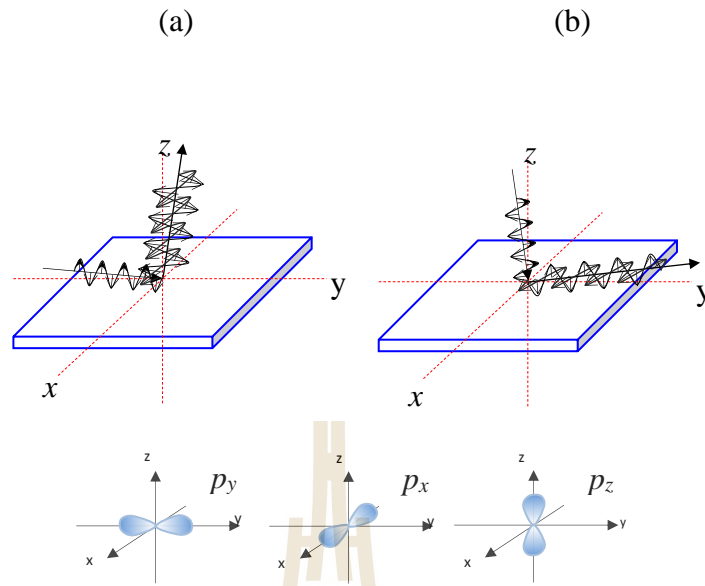


Figure 5.3 (a) The near-grazing incident x-ray is polarized in z' direction which is nearly parallel to z axis of the crystal while the emitted x-ray isn't filtered and hence has its polarization in $x'y'$ plane which is nearly perpendicular to z axis of the crystal. (b) The near normal incident x-ray is polarized in y' direction which is nearly normal to z axis of the crystal, while the emitted x-ray is not filtered, therefore has its polarization in both x' and z' components, which are both nearly perpendicular and parallel to z plane of the crystal.

Now consider the emission, for NG incidence, the emission is contributed significantly by the p_{xy} dominated bands because the emitted photon ray will travel nearly parallel to c axis of the crystal thus its electric field lie in xy plane, same as s-polarized and p-polarized orbitals (as shown in Figure 5.3(a)). Thus to interpret the NG spectra we consider the p_z conduction bands from Figure 5.1(b), as described above and p_{xy} valence band from figure 1a (this is the same as saying M31 dominates). For NN incidence, the emitted photon ray polarization has both z' and x' components, therefore both p_x and p_z also contribute to the emission spectra. As a result, both p_{xy} and p_z weighted valence bands from

Figure 5.1(a) and 5.1(b) contribute to the emission, but only p_{xy} conduction bands from figure 1a contribute to the absorption. In order to interpret the RXES spectra more easily, the color-weighted electronic band structures from Figure 5.1(a) and 5.1(b) are rearranged accordingly, as shown in figure 5.4(a) for near-normal incidence and 5.4(b) for near-grazing incidence. The points in both valence and conduction bands that contribute to the RXES process are marked with the same symbol for each excitation energy.

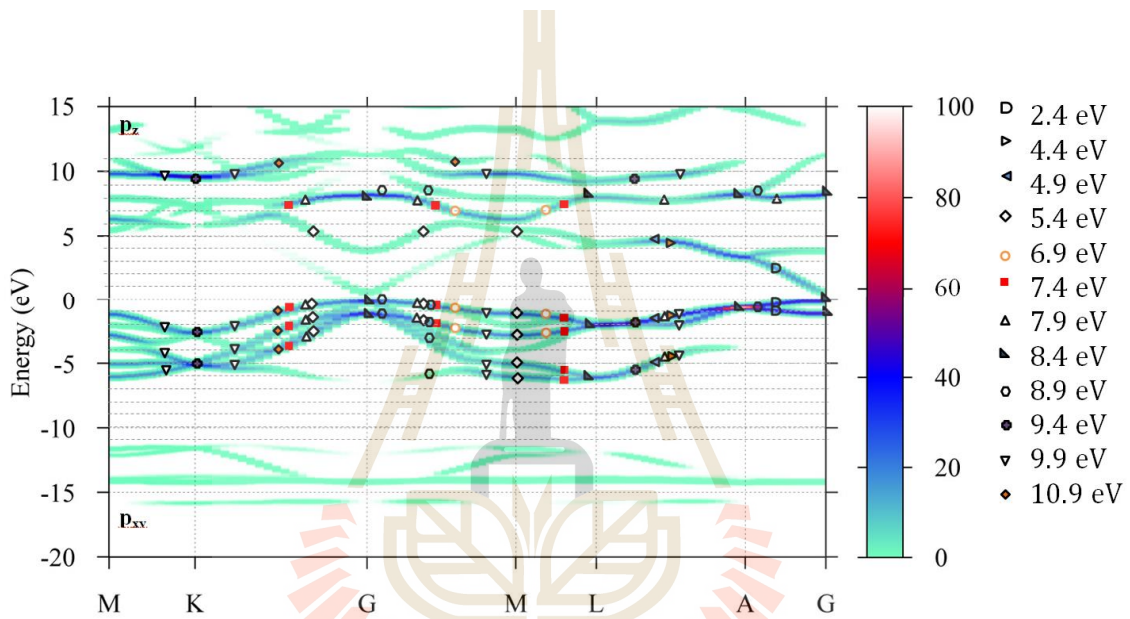


Figure 5.4 (a) Intensity map of the calculated band structures used for the interpretation of RXES near-grazing (NG) spectra. The intensity of the bands is proportional to the p_z and p_{xy} characters for the unoccupied and occupied bands respectively. The symbols presented in the bands mark the points in the bands that electronic transitions take place at each specific excitation energy, absorption processes for the unoccupied bands and emission processes for the occupied bands.

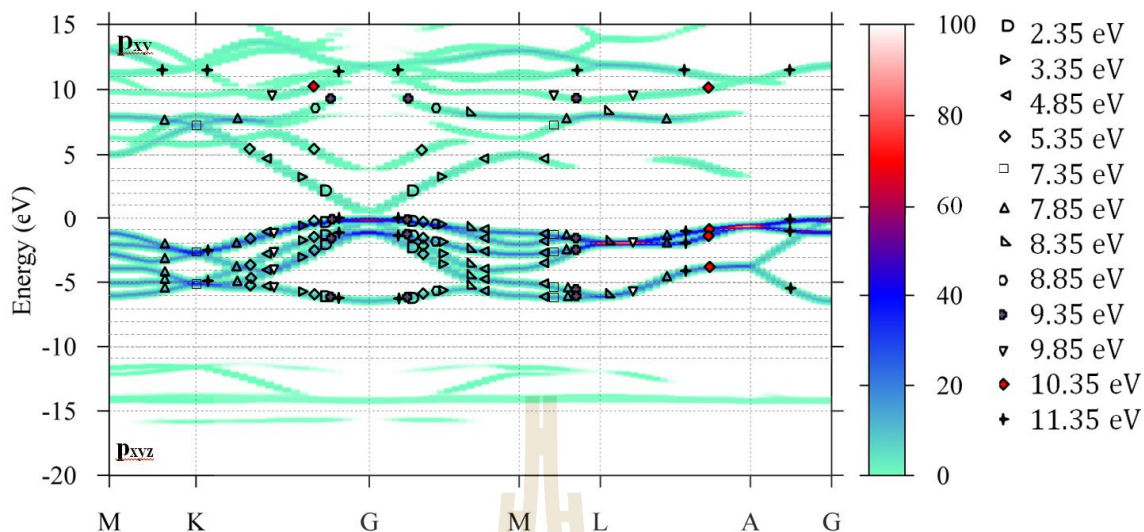


Figure 5.4 (b) Intensity map of the calculated band structures used for the interpretation of RXES near-normal (NN) spectra. The intensity of the bands is proportional to the p_{xy} and $p_{xy} + p_z$ characters for the unoccupied and occupied bands respectively. The symbols presented in the bands mark the points in the bands that electronic transitions take place at each specific excitation energy, absorption processes for the unoccupied bands and emission processes for the occupied bands.

We now describe the trends in Figure 2 starting with the NG spectra. The experimental spectra consists of a strong peak between 0 and -3 eV which gradually develops a higher binding energy tail down to about -5 eV as the incident photon energy increases. These are the so called N 2p bands. Another weak peak near about -6 eV is due to the emission from N 2p states hybridized with In 3d semicore states.

According to the band plots and our analysis of the angular effect as explained above we can explain how the trends of the peaks in the spectra are related to the band dispersive. The first lowest spectrum 2 main peaks between 0 and 2 eV in the calculated spectrum, which are merged into one peak in the experiment, should derive from the upper

two valence bands along G-A . The points in the bands which responsible for the electronic transitions are marked as shown in Figure 4(a). When the photon energy increases these two bands approach each other and merged into one band as we reach point A at the energy of 4 eV. In the second and third (4.4 and 4.9 eV) spectra, the photon energy is high enough to be moving upward along A-L in the conduction band. Along this direction, the upper valence bands disperse to the higher binding energy and this explains the downward shifting of the first peak in the three lowest spectra. The very weak peak between -4 and -6 eV in the first three spectra derives from the p_{xy} character in the valence band near -5 eV along A-L. For the photon energy 5.4 eV there are contributions from the same conduction band in three regions, one near point M, another two near the gamma point along G-M and G-K. This gives rise to broader peaks between 0 and -3 eV derived from the top two valence bands with strong p_{xy} character along G-M and G-K. For the 6.9 and 7.4 eV spectra, we move up to another conduction band near point M in the conduction band. At this points there are 5 valence bands between -6 to 0 eV between G-M-L contributing to the emissions which are responsible for the broad spectrum tailing down to near -6 eV. The two main peaks near -1 and -3 eV arise from two bands near M point as marked with the circle in figure 4a which are dispersing up as we can see that the two main peaks in the spectra are shifting to the higher energy. The broad peak near -3 to -4 eV is stronger in the 7.4 eV spectrum due to more contribution from the bands between G-K. The tails of the spectra between -4 to -6 eV become less broad for 7.4 eV spectrum as corresponding to the two lower valence bands between -5 and -6 become closer as we move from M toward L. At excitation energy 7.9 eV, we still look at the same conduction band but stronger contributions once we move toward G point in the conduction band, as a result, the most upper conduction bands around G point are also closer together. That is why we see the much less broad peak between -1 to -4 eV in the spectrum. In addition, we also have a strong contribution between A-G which results in the additional (first) peak of the spectrum contributed by the two most upper valence band

near 0 eV. At 8.4 eV, there are contributions from many strong points in the conduction band, with high DOS since the band is nearly horizontal. The strongest contribution is near point A with emission from the most upper conduction band near -1 eV. Another strong point is from point G by the emission of the two most upper conduction bands near 0 and -1 eV. The most upper bands disperse up along A to G that is why we see the first peak of the spectrum moving up to the higher energy. The lower valence bands near point G also disperse up rapidly merging with the upper one, therefore we see the peak near -5 eV in the 7.9 spectrum merging into the peak near -1 eV in the 8.4 eV spectrum. We also have some contribution near point L for the valence band near -2 and -6 eV. On the spectrum 8.9 eV, we still see the first peak, near 0 eV, continuing to higher energy since the valence band near point A is dispersing up, however, with the weaker contribution. We have the contribution from near point G which give rise to the peak near 0 and 1 eV. The weak contribution from the conduction band between G and M associates with the broader peaks between -1 to -4 eV from different valence bands in that region, including the one near -6 eV. However these peaks are not sharp because the contributions are equally weak. The experimental spectrum is also spreading, not sharp. On the 9.4, 9.9 and 10.9 eV spectra, we move up onto another conduction band and that is why we see the new trends on the peaks. At 9.4 eV, the conduction band at K dominates and give rise to the peaks near -2.5 and -5 eV in the spectrum. The peak near 2.5 eV can also be seen in the experiment. There are also weaker contributions from several points between M-L and A-L which contributed from the valence bands between -1.5 to -2 eV and -5 to -6 eV. At 9.9 eV the strongest contribution comes from near point K which the valence bands split and disperse up and down. Therefore we see the peak near -2 and -5 become spreading out as the bands split apart. Another strong contribution comes from the wide range of band between G-M-L because the conduction band is nearly horizontal. The valence bands disperse up between -1 to -6 eV. That is why we see the peaks in the spectrum shift toward higher energies. At higher photon energies the

conduction bands become less dispersive and larger parts of the Brillouin zone start to contribute to CRXES therefore it is very difficult to isolate specific contribution to the measured spectra.

For the NN spectra, the situation is a bit more complicated as we must consider both p_{xy} and p_z valence bands for the emission as explained above. As we consider the energy below 5 eV, we are looking at the conduction CBM between K-G-M Vs G-A-L regions for the NG spectra. The most obvious contribution from p_z VB in the NN spectra at low energies, are the stronger peak, when comparing to the NG spectra, near -6 eV dispersing toward lower binding energy while the main peak near 0 eV dispersing toward the higher binding energy as the photon energy increases. This is explained as the contribution from the strong p_z character in the upper VB near 0 eV and the lower VB near -6 eV near the G point as shown in figure 1b. At 7.35 eV we move up to the intersection of CBs at point K which give rise to the strong peak near -3 eV contributed largely from VB near -3 eV with strong p_z character. This peak disperses toward lower binding energy as the energy increases as the band disperses upward. At 8.35 eV we reach point L in the CB and we can see a sharper peak near -1 and -6 eV which are strongly contributed from the VB near -1 and -6 eV. At this point we can clearly see that there is no contribution from G point as seen in the 8.4 eV NG spectrum. Moving up from 8.85 to 9.35 eV in the CB near the G point we can see that the VB near 0 eV disperses upward therefore we can see the small peak near 0 eV disperses to the lower binding energy. The peaks near -3 eV shows that we also have contribution from the VB near point L at -3 eV with p_z character. Above 9.35 eV the spectra have contributions from various points in the BZ but most part is from near L and G points that is why we see the similar shapes of spectra as the ones at low energies. Once we hit 9.85 eV, we again hit the conduction band near point L that is why the spectrum look like the 8.35 eV spectrum with strong contributions from the VBs near -1 and -6 eV. At 11.35 eV, we have contributions from various points in the conduction bands but at least we can see that

we have some contribution from point G and K in the conduction band and the tail between -2 to -6 eV of the spectrum looks similar to the 7.35 eV and the main peak near 0 eV looks similar to the ones at low energies.

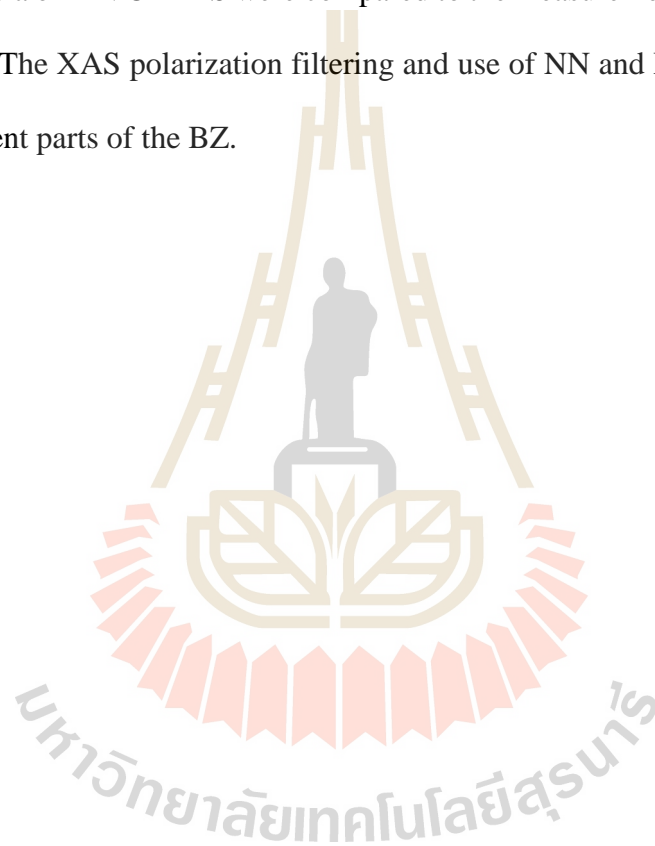
Overall the calculated CRXES agree well with the experiments in term of the trends of the peaks even though the shape of the peaks do not match exactly and the experiments do not show as much dispersive detail as the calculation. This is due to the difficulty in extracting the coherent part of the measured spectra and the difficulty of making pure crystal of InN which may result in a mixed structure between Zincblend and Wurtzite structures while it is only Wurtzite structure in the calculation.

5.4.3 Extracting band-structure information from CRXES

The advantage of CRXES over other methods is that it is able to resolve conduction bands in both energy and k spaces. It enable us to extract information about higher conduction bands in the BZ. For example, by looking at the NG CRXES spectra we can see that the 7.9 eV looks similar to the 2.4 eV spectrum. This means that there must be a conduction band with strong pz character near 7.9 eV around the G point. This assumption can be made with the CRXES spectra independent of the calculated band structure. This technique has advantage over XAS because in coherent emission the valence and conduction band stated are assumed not to be bothered by the presence of a core hole at the time scale of the combined absorption and emission process. Generally in the XAS process the final state rule implies that the whole system is relaxed as the core hole presents. Therefore the state being detected in XAS is more of the representative of the local states around a Z+1 impurity rather than the unperturbed state of material. Therefore it is much more accurate to measure the unperturbed conduction bands relative to the valence bands as in the CRXES.

5.5 Conclusion

We calculated the electronic band structure of InN by using GW calculation and confirmed the electronic band gap to be 0.7 eV. We then calculated CRXES spectra based on Kramer-Heisenberg rule with the experimental geometry and polarization effect in the consideration following the framework that has been previously tested on ZnO. The calculated spectra of InN CRXES were compared to the measurements and good agreements were obtained. The XAS polarization filtering and use of NN and NG incident allows us to focus on different parts of the BZ.



CHAPTER VI

XANES OF $\text{Bi}(\text{Mg}_{0.5}\text{Ti}_{0.5})\text{O}_3$

This chapter is based on our work that has recently been published in a *ferroelectrics* journal (Schwertfager et al., 2016).

6.1 Introduction

$\text{Bi}(\text{Mg}_{0.5}\text{Ti}_{0.5})\text{O}_3$, henceforth BMT, is one of the promising high-temperature Pb-free antiferroelectric materials for future applications because of its antiferroelectric-like displacement of Bi cations and its octahedral tilting characteristics. Because the cation ordering of materials in this class directly affects their antiferroelectric properties, it is important to understand the actual structure of BMT. X-ray diffraction (XRD) experiment by Khalyavin and coworkers (Khalyavin et al., 2006) reveals the crystal structure of BMT. They found that the oxygen cages of Mg and Ti are tilted, and the cations are proposed to move off-center from the center of their oxygen cages by 0.287, 0.086 and 0.086 Å for Bi, Ti, and Mg, respectively. Because it is unclear whether BMT is an ordered or disordered alloy, it is almost impossible to accurately resolve the fine structure (off-centering) of each cation species based on the XRD data. Recently, Suewattana and coworkers (Suewattana et al., 2012) performed first principles calculations starting from the experimental structures in (Khalyavin et al., 2006), and found that these structures are under internal strain and could be relaxed reducing the total energy by ~ 0.7 eV per Bi. The cations are shifted from the center of the oxygen cages by large values, i.e., by 0.505, 0.300 and 0.232 Å, for Bi, Ti, and Mg, respectively. BMT is known to be centrosymmetric. Therefore, the total polarization is expected to vanish. However, the large cation displacements can lead to a large

polarization if the effects are not canceling each other. Among various experimental characterization techniques, x-ray absorption spectroscopy (XAS), which can selectively probe the local structure around each element, is highly powerful and suitable to identify elemental specific local structures. However, to aid experimental identification, especially for the near edge region of the XAS called x-ray absorption near edge spectra (XANES), the first principles calculations of plausible structural models are generally needed to simulate the spectra for comparison with the measured results.

In this thesis, we perform our calculations of Bi, Mg and Ti-edges XANES spectra of BMT for different structural models, in order to aid identification of the actual structure of this material. The models studied include a high symmetric structure (the B-cations reside at the center of their respective octahedral oxygen cages), the experimental proposed structures (based on XRD measurements (Khalyavin et al., 2006) and the calculated structure (based on the energy optimization calculations (Suewattana et al., 2012)).

6.2 Calculation methods

The calculations for XANES spectra of four different BMT structural models corresponding to different cation off-centering magnitudes were performed. The model structures are shown in Figure 6.1. These four models include:

- 1) A high symmetric (ideal) structure

This structure has the B-cations in the middle of the non-tilted cages. The lattice constant is optimized by using first principle calculation based on local density approximation (LDA) as implemented in VASP code. The computational details of the first principles calculations are similar to (Fongkaew et al., 2013). The k-points mesh of 3x3x3 was used. The cut-off energy was set at 500 eV. For the cases that required structural

optimizations, the structure was relaxed until the residue force on each and every atom became less than 0.001 Ry/Å.

2) The experimental proposed structure with *Pbam* space group. And

3) The experimental proposed structure with *Pnmm* space group.

These two structural models are the experimental ones proposed by Khalyavin and coworkers (Khalyavin et al., 2006) based on XRD experiments. One structure is in *Pbam* and another one in *Pnmm* space group with Glazer's tilt systems of $a_{+}^{-}b_{0}^{0}a_{+}^{-}$ and $a_{+}^{-}b_{0}^{0}a_{-}^{-}$ respectively (subscripts “+” and “-” denote cation displacements along a given axis and the superscripts have their usual Glazer's meaning). The main difference between the two models proposed by Khalyavin and coworkers (Khalyavin et al., 2006) is the tilting of the diagonal axis of the oxygen cages, one tilted on the x axis and another on the y axis. These two structures have very similar lattice parameters and during the calculations they were fixed at their respective experimental values of $a = 11.3196$, $b = 5.6423$, and $c = 7.8314$ Å for *Pbam*; and $a = 11.3325$, $b = 5.6501$, and $c = 7.8159$ Å for *Pnmm* structures. Note that these two structures are very similar when they are viewed in a large cluster size.

4) The fully relaxed BMT structure by (Suewattana et al., 2012), calculated by using first principle calculation to relax the experimental proposed *Pbam* structure. The schematic crystal structures of all models are shown in Figure 6.1. First principles (*ab initio*) calculations of the XANES spectra based on the structures of all four models were calculated by FEFF 8.2 codes (Ankudinov et al., 1998; Ankudinov et al., 2002). The codes utilize a full multiple scattering approach based on *ab initio* overlapping muffin-tin potentials. The *ab initio* muffin-tin potentials were obtained by using self-consistent calculations with Hedin – Lundqvist exchange – correlation functions (Hedin, 1969). The self-consistent

calculations were performed in the sphere radius 10 Å (containing approximately 325 atoms) around the absorber cations.

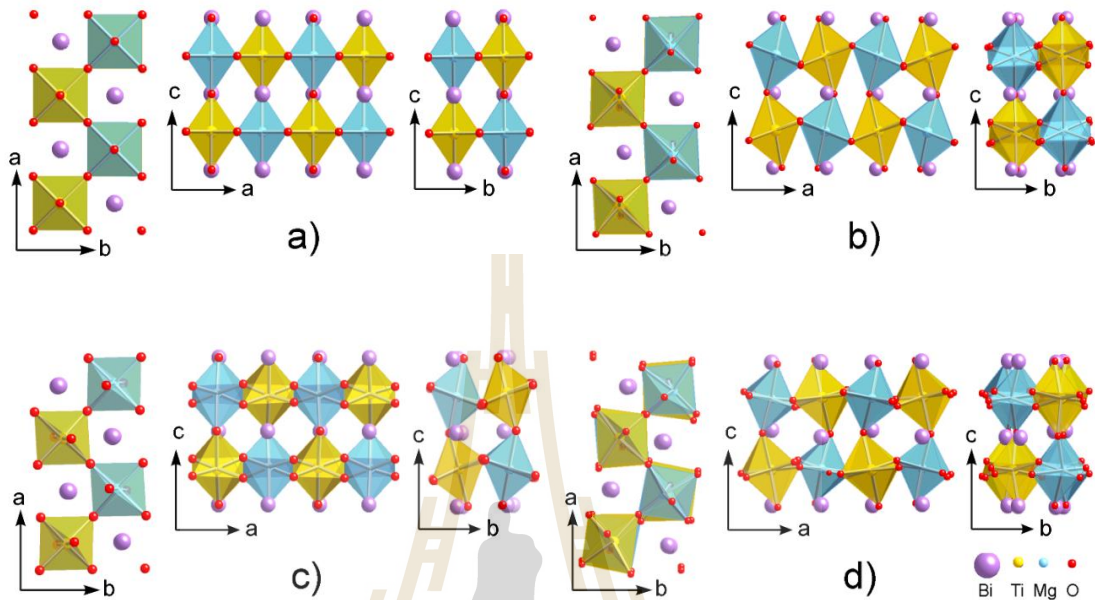


Figure 6.1 Structural models of BMT used in our calculation to calculate XANES spectra. (Schwertfager et al., 2016) a) Ideal cubic perovskite (high symmetric) structure – each cation is resided in the center of its oxygen cage, b) and c) the structural models proposed by (Khalyavin et al., 2006) based on their XRD data with the assumption of *Pbam* and *Pnmm* space group, respectively – the cations slightly shifted off-center, and d) the fully relaxed *Pbam* structure based on first-principles calculation proposed by (Suewattana et al., 2012)

The electronic transitions associated with the XANES measurements must follow the dipole selection rule. An X-ray absorbance can be calculated by the Fermi's golden rule,

$$\mu \propto \sum_f |\langle f | D | i \rangle|^2 \delta(E_i - E_f + \hbar\omega) \quad (6.1)$$

where $\mu(\omega)$ is an x-ray absorbance, $|i\rangle$, $|f\rangle$, E_i , and E_f are the initial and final states and their corresponding energies, respectively, ω and D are the photon frequency and the dipole operator.

In this thesis, we chose to calculate Ti and Mg *K*-edge and Bi *L*₃-edge XANES. The choices are based on the x-ray energy range that is suitable for actual XAS measurement at most synchrotron facilities. At the Synchrotron Light Research Institute (Public Organization), Nakhon Ratchasima, Thailand, the XAS beamline can measure in the energy range of 1,250 – 10,000 eV; making it possible to measure Mg and Ti *K*-edge (Bi *L*₃-edge requires higher photon energy and is needed to be measured elsewhere). As a consequence of the selection rule, *K*-edge XANES corresponds to the dipole transition from $|s\rangle$ to $|p\rangle$ state, and *L*₃-edge corresponds to that of $|p\rangle$ to $|d\rangle$ and $|p\rangle$ to $|s\rangle$ states.

6.3 Results and discussions

XANES technique is a powerful tool to investigate the local structure of the materials by speculating each element separately. Each element's x-ray absorption spectra take place at its characteristic x-ray energy and contain information of its neighboring arrangements. For BMT, there are three cations, Bi, Ti, and Mg. Therefore, the XANES measurement for their respective absorption edges can be used to reveal the local structure of this material. Here we calculated the expected spectra of all three cation absorbers for four BMT structural models. For the spectra of individual cation (Bi, Ti and Mg), the main features related with the off-center shifts of the cation will be discussed.

6.3.1 Bi *L*₃-edge XANES of BMT

The commonly known *L*₃ absorption edge energy of Bi is 13.418 keV. Therefore the Bi-*L*₃ edge XANES spectrum has the edge around this value. The calculated Bi *L*₃-edge XANES spectra of the four model structures of BMT are shown in Figure 6.2. The XANES spectrum of the ideal structure is clearly different from those of other models in general. The high symmetry of the ideal structure leads to the clear and distinct features. There are three broad peaks at three main regions. The two spectra, generated from the

structural models proposed by the experiment (henceforth “experimental models”), have very similar features due to their similarity in the local structure around the Bi absorber. The spectra contain a shoulder A around the edge area followed by the main peak B and broader peaks C, D and E at the energy of 13,430, 13,439, 13,450, 13,473, and 13,516 eV, respectively. The spectrum from the calculated model with fully relaxed structure contains almost all features observed in the experimental spectra with some slight differences. In comparison with the experimental model spectra, the spectrum of the fully relaxed structure shows reduction in shoulder A and stronger peak B with the peak position slightly shifted toward higher energy by about 1 eV. Peak C moves closer to peak B and appears only as a shoulder. Peak D is broader and is shifted to the higher energy; merging with peak E thus appears as a small shoulder. Among the four models, the Bi atom stays at the center of the oxygen cage for the ideal structure model, but shifted off-center by 0.287 Å for the experimental models and by 0.505 Å for the fully relaxed model. If we investigate the main features that varied as the Bi atom moves off-center we can associate the off-center shift with (1) the reduction in shoulder A – the ideal structure spectrum has this shoulder appear almost as a first peak (2) the enhancement and shifting toward higher energy of peak B – the ideal structure spectrum has peak B at about 13,436 eV.

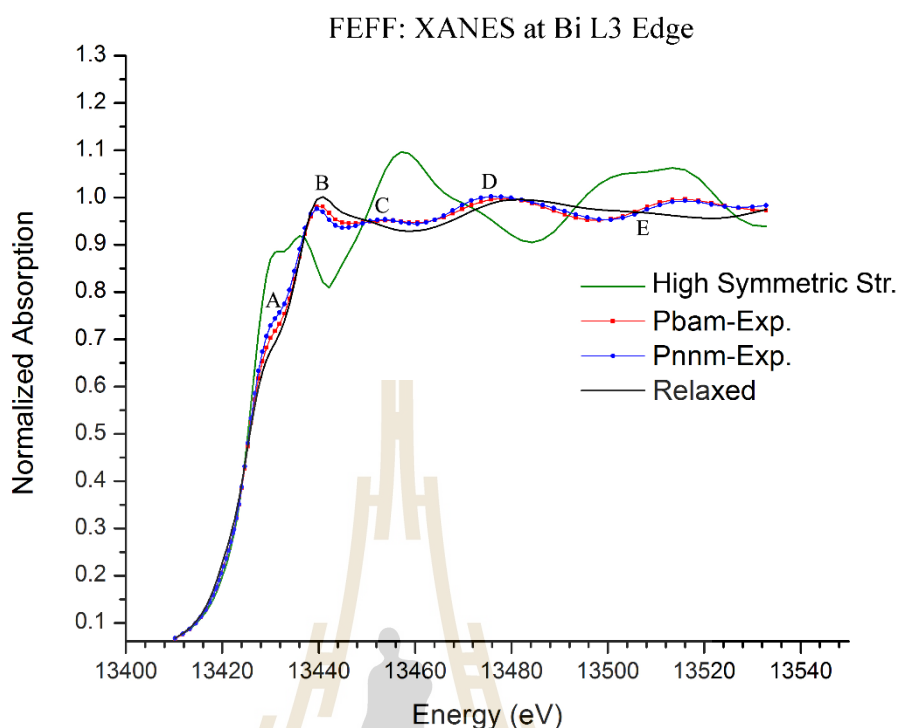


Figure 6.2 Bi L_3 -edge XANES spectra of four different structural models of BMT. (Schwertfager et al., 2016)

6.3.2 Ti K -edge XANES of BMT

The commonly known K absorption edge energy of Ti is at 4,965 eV. Therefore the Ti K -edge XANES of BMT has the absorption edge around this value. The calculated Ti K -edge XANES spectra of the four model structures of BMT are shown in Figure 6.3. All spectra can be characterized with a few common features. At 4,971 eV, there is a pre-edge peak A followed by a shoulder/small peak B at 4,981 eV and main peaks C and D at 4,988 and 4,990 eV. At higher energy, there are broad peaks E and F at 5,004 and 5,043 eV, respectively. Among four models, the Ti atom stays at the center of the oxygen cage for the ideal structure model, shifted off-center by only a small amount of 0.086 Å for the experimental models and by a large amount of 0.300 Å for the fully relaxed model. From Figure 6.3, it is clearly seen that for the fully relaxed structure the pre-edge peak A is

significantly enhanced. For the experimental model spectral, the peak only appears as a small bump while for the ideal structure peak A vanishes. These indicate that the magnitude of the pre-edge peak A goes with the off-centering of Ti. The increase in the pre-edge peak A as the Ti shifts off-center is consistent with the finding of Vdrinskii and co-workers (Vedrinskii et al., 1998). Vdrinskii and co-workers calculated Ti *K*-edge XANES of various perovskite $ATiO_3$ and suggested that the pre-edge feature in Ti *K*-edge XANES spectrum can be used to identify Ti off-center shift. Beside the pre-edge peak A, the main peaks C and D are also affected by the off-center shift of Ti. When there is no off-center shift (the ideal structure spectrum) peak C is the largest and peak D appears to be a shoulder. When off-center shift takes place (the other three spectra) peak C is reduced to be a shoulder and peak D becomes dominant. However, the switching of the C and D peaks does not appear to go proportionally with the magnitude of the off-centering as the off-center shift for the case of experimental models are much smaller than the fully relaxed model be the C and D features are almost the same for these cases. We may conclude Peak B also appears to enhance and peak E appears to reduce as a consequence of off-center shift of Ti. However, the magnitude of the enhancement and reduction does not directly related with the amount of the shift of Ti. As we can see from the spectra, the fully relaxed model has the Ti shifted off-center the most but the enhancement in peak B and reduction in peak E (compared to that of the ideal structure spectrum) are smaller than the experimental model spectra.

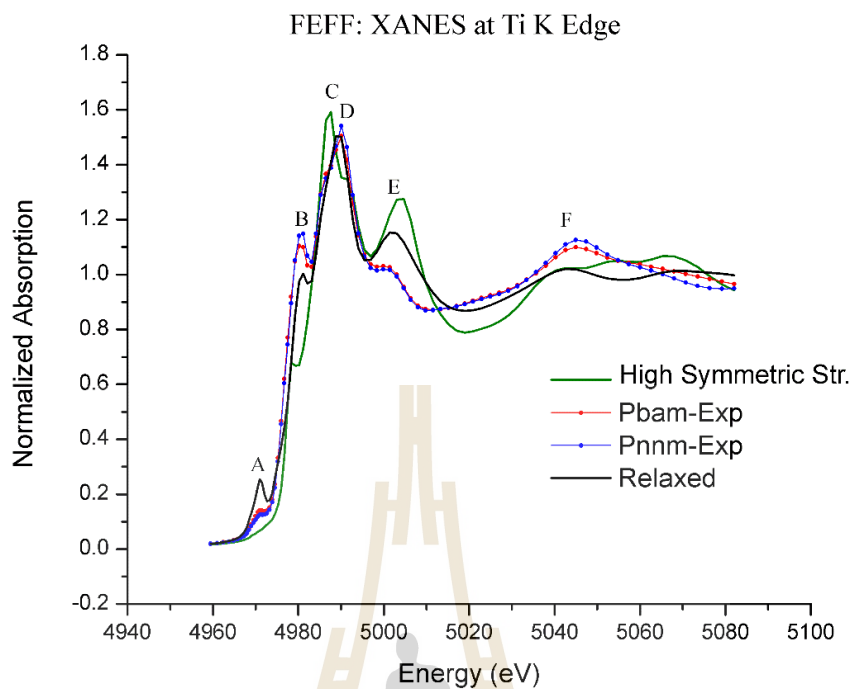


Figure 6.3 Ti *K*-edge XANES spectra of four different structural models of BMT. (Schwertfager et al., 2016)

6.3.3 Mg *K*-edge XANES of BMT

The commonly known *K* absorption edge energy of Mg is at 1,305 eV. Therefore the Mg *K*-edge XANES of BMT has the absorption edge around this value. The calculated Mg *K*-edge XANES spectra of the four model structures of BMT are shown in Figure 4. All spectra can be characterized with a few common features. At 1,307 and 1,309 eV, there are pre-edge shoulders A and B followed by the main peak C at 1,314 eV and smaller peaks D and E at 1,320 and 1,324 eV. At higher energy, there is a broad peak F at 1,350 eV. Among the four models, the Mg atom stays at the center of the oxygen cage for the ideal structure model, shifted off-center by only a small amount of 0.086 Å for the experimental models and by a large amount of 0.232 Å for the fully relaxed model. From Figure 4, it is apparent that the pre-edge shoulder A is related to the off-center magnitude of Mg. The pre-edge shoulder A disappears in the ideal structure where there is no off-

centering. It is getting stronger in the experimental spectral and is strongest in the relaxed structure as the Mg off-centering shift increases. Main peak C and peak D also change with respect to the off-center shift of Mg. As Mg shifts off-center (starting from at the center in the ideal model to slightly shifted off-center in the experimental model to the most off-center shift in the fully relaxed model) peak C is getting broader and shifted toward the lower energy while peak D is reduced. Note that, instead of viewing the main peak C to shift toward the lower energy, one can view the shift as the shift of the absorption edge position down to the lower photon energy as Mg shifts off-center. A small hump at E is also the result of the off-center shift of Mg. However, the magnitude of the enhancement and reduction does not directly relate to the amount of the shift of Mg. Finally the peak F, only occurs in the relaxed model and appears as a broad shoulder in the experimental model; suggesting that it is associated with the Mg off-center shift.

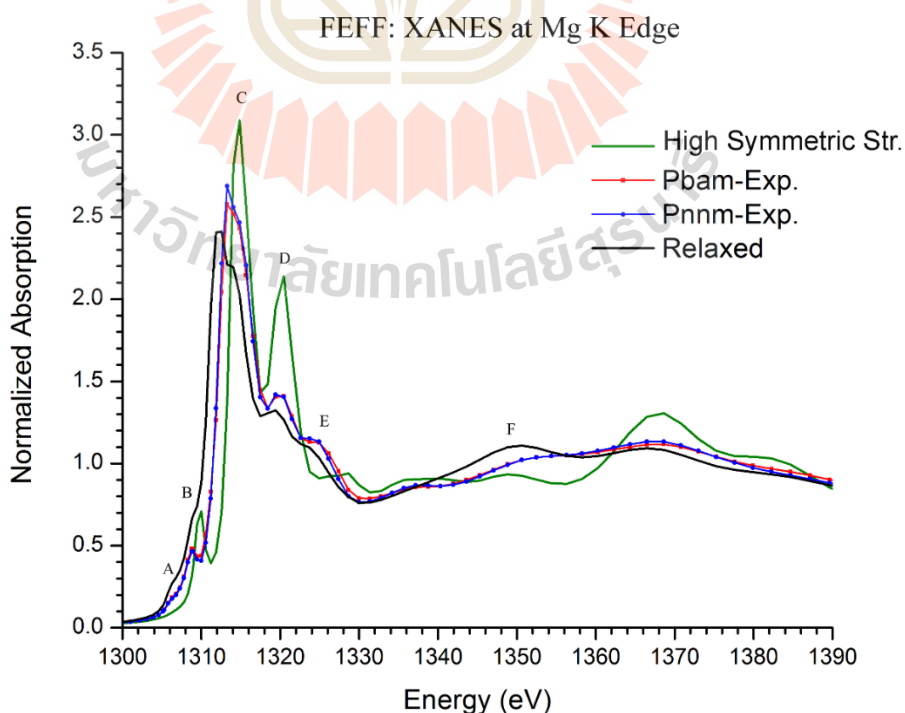


Figure 6.4 Mg *K*-edge XANES spectra of four different structural models of BMT. (Schwertfager et al., 2016)

6.4 Conclusions

The calculations were based on first principles calculations for Bi L_{3-} , Ti $K-$ and Mg $K-$ edges XANES spectra of $\text{Bi}(\text{Mg}_{0.5}\text{Ti}_{0.5})\text{O}_3$. Four different crystal structure models were proposed in this thesis for the simulation of the XANES spectra including (1) the high symmetric structure where the cations are located perfectly at the center of oxygen cages, to (2) the two models proposed based on XRD measurements that has the cations shifted off-center, and (3) the fully relaxed structure model based on first principles calculations that found the cations significantly shifted off-center. Because different models have different magnitudes of cation off-center shifts, the identification of the features in the XANES spectra that relates with the off-center shift can be identified as follows:

1) For Bi L_{3-} edge XANES, the reduction in the first shoulder (A) at 13,430 eV and the enhancement and shifting toward higher energy of the main peak (B) at 13,439 eV are the main features associated with the off-center shift of Bi.

2) For Ti $K-$ edge XANES, the off-center shift of Ti leads to the increase in the pre-edge peak (A) at 4,971 eV.

3) For Mg $K-$ edge XANES, the off-center shift of Mg leads to the shift of the edge energy down to the lower photon energy.

These observed features would be able to aid future experimental identification of the cation local structures in this material.

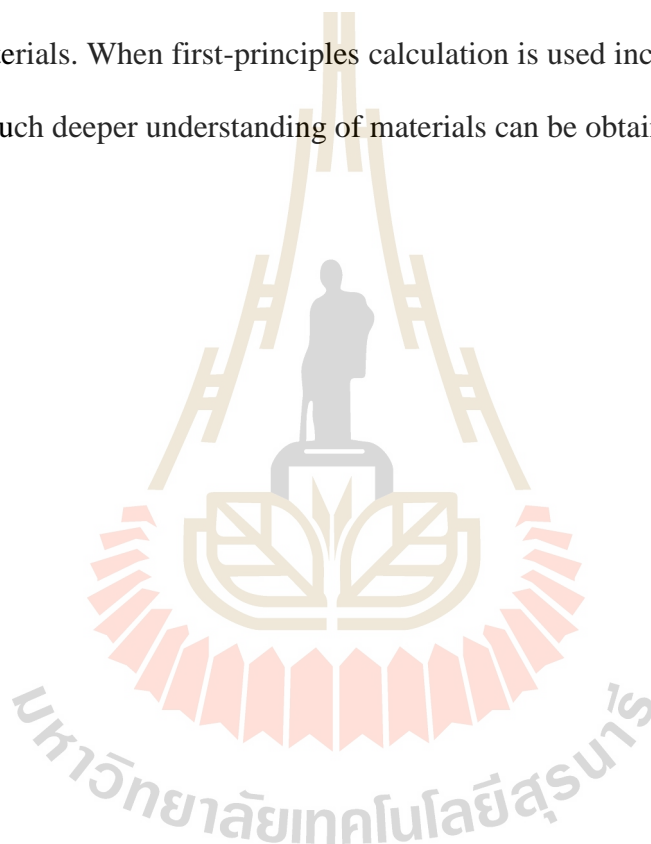
CHAPTER VII

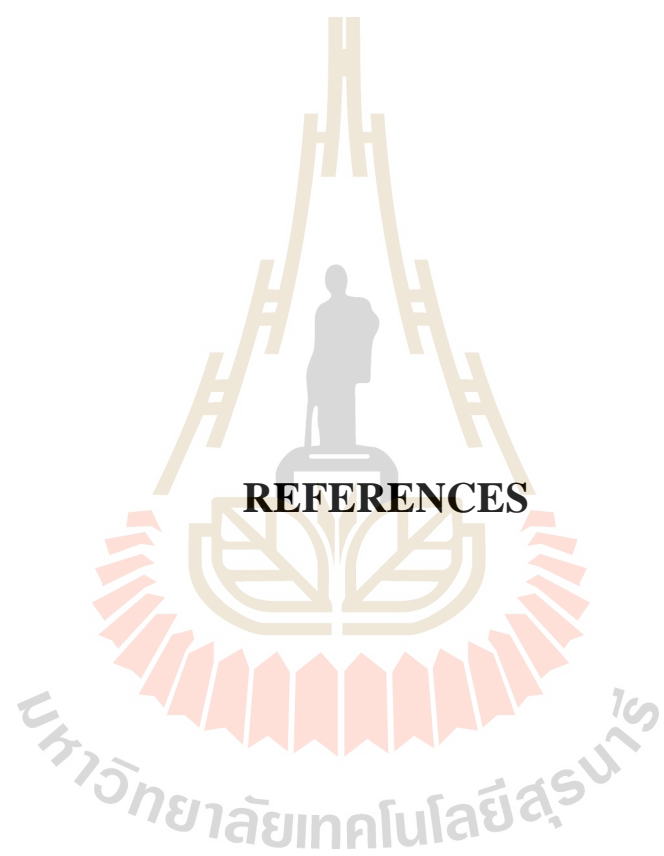
CONCLUSION

This thesis focuses on the use of first-principles calculations to cooperate with existing x-ray measurement methods to study electronic band structures and physical structure of materials. We have chosen two x-ray techniques for the measurements, RXES and XANES, in which their background theories were explained in chapter II. In chapter III, we performed the first-principles calculation implemented in FP-LMTO code to calculate the electronic band structure of graphene with GW approximation. The RXES spectra were calculated based on Kramer Heisenberg rule and then compared to experimental spectra in order to verify our calculation. The core-hole effect was taken into account when aligning between the calculated and experimental spectra. Great agreement between the calculated and experimental results. In chapter IV, we used first-principles calculation implemented in FP-LMTO code to study the electronic band structure of InN with GW approximation, similar to what we have done preciously with graphene. However, in this study we focused on how RXES could be used to study different bands in the electronic structure, such as p_x and p_y or p_z , by adjusting the angle of incident. The RXES spectra were also calculated to compare with the experimental ones. With the help with our first-principles calculation, better understanding of how the experimental spectra relating to the electronic band structure of InN was obtained. In chapter V, we used first-principles calculation implemented in VASP code to identify the actual structure of BMT and suggest the way to verify its actual structure by using XANES measurement. We calculated the XANES spectra for different possible structures of BMT using FEFF code. The off-centering features of the cations in BMT for

XANES spectra were identified and may be used in the future to identify the actual structure of this material. All the experimental results appeared in this thesis were obtained by our collaborators and we only worked on the calculation parts.

In summary, first-principles calculation is a very powerful method to be used to study the electronic band structure and physical structure of materials. The RXES technique is suitable to study electronic band structure, while XANES is good for the study of local structure of materials. When first-principles calculation is used incorporated with the X-ray techniques, a much deeper understanding of materials can be obtained.





REFERENCES

REFERENCES

- Ahmed, R., Akbarzadeh, H. and Fazal e, A. (2005). A first principle study of band structure of III-nitride compounds. **Physica B: Condensed Matter** 370: 52.
- Ankudinov, A. L., Bouldin, C. E., Rehr, J. J., Sims, J. and Hung, H. (2002). Parallel calculation of electron multiple scattering using Lanczos algorithms. **Physical Review B** 65.
- Ankudinov, A. L., Ravel, B., Rehr, J. J. and Conradson, S. D. (1998). Real-space multiple-scattering calculation and interpretation of x-ray-absorption near-edge structure. **Physical Review B** 58: 7565.
- Aryasetiawan, F. and Gunnarsson, O. (1998). The GW method. **Reports on Progress in Physics** 61: 237.
- Beeby, J. L. (1967). The Density of Electrons in a Perfect or Imperfect Lattice. **Proceedings of the Royal Society of London. Series A, Mathematical and Physical Sciences** 302: 113.
- Berger, C., Song, Z., Li, X., Wu, X., Brown, N., Naud, C., Mayou, D., Li, T., Hass, J., Marchenkov, A. N., Conrad, E. H., First, P. N. and de Heer, W. A. (2006). Electronic Confinement and Coherence in Patterned Epitaxial Graphene. **Science** 312: 1191.
- Bott, E., Methfessel, M., Krabs, W. and Schmidt, P. C. (1998). Nonsingular Hankel functions as a new basis for electronic structure calculations. **Journal of Mathematical Physics** 39: 3393.
- Brühwiler, P. A., Kuiper, P., Eriksson, O., Ahuja, R. and Svensson, S. (1996). Core Hole Effects in Resonant Inelastic X-Ray Scattering of Graphite. **Physical Review Letters** 76: 1761.

- Brühwiler, P. A., Maxwell, A. J., Puglia, C., Nilsson, A., Andersson, S. and Mårtensson, N. (1995). Absorption of Graphite. **Physical Review Letters** 74: 614.
- Bylander, D. M., Kleinman, L. and Lee, S. (1990). Self-consistent calculations of the energy bands and bonding properties of B₁₂C₃. **Physical Review B** 42: 1394.
- Carlisle, J. A., Shirley, E. L., Hudson, E. A., Terminello, L. J., Callcott, T. A., Jia, J. J., Ederer, D. L., Perera, R. C. C. and Himpsel, F. J. (1995). Probing the Graphite Band Structure with Resonant Soft-X-Ray Fluorescence. **Physical Review Letters** 74: 1234.
- Carlisle, J. A., Shirley, E. L., Hudson, E. A., Terminello, L. J., Callcott, T. A., Jia, J. J., Ederer, D. L., Perera, R. C. C. and Himpsel, F. J. (1996). Carlisle \textit{et al.} Reply. **Physical Review Letters** 76: 1762.
- Cowan, R. D. (1981). **The Theory of Atomic Structure and Spectra**. California. University of California Press Books.
- Davydov, V. Y., Klochikhin, A. A., Emtsev, V. V., Ivanov, S. V., Vekshin, V. V., Bechstedt, F., Furthmüller, J., Harima, H., Mudryi, A. V., Hashimoto, A., Yamamoto, A., Aderhold, J., Graul, J. and Haller, E. E. (2002). Band gap of InN and In-rich In_xGa_{1-x}N alloys (0.36 < x < 1). **physica status solidi (b)** 230: R4.
- Davydov, V. Y., Klochikhin, A. A., Seisyan, R. P., Emtsev, V. V., Ivanov, S. V., Bechstedt, F., Furthmüller, J., Harima, H., Mudryi, A. V., Aderhold, J., Semchinova, O. and Graul, J. (2002). Absorption and Emission of Hexagonal InN. Evidence of Narrow Fundamental Band Gap. **physica status solidi (b)** 229: r1.
- Dedkov, Y. S., Fonin, M., Rüdiger, U. and Laubschat, C. (2008). Rashba Effect in the Graphene/Ni(111) System. **Physical Review Letters** 100: 107602.
- Foley, C. P. and Tansley, T. L. (1986). Pseudopotential band structure of indium nitride. **Physical Review B** 33: 1430.

- Fongkaew, I., T-Thienprasert, J., Singh, D. J., Du, M. H. and Limpijumnong, S. (2013). First principles calculations of Hydrogen—Titanium vacancy complexes in SrTiO₃. **Ceramics International** 39, Supplement 1: S273.
- Gell-Mann, M. and Brueckner, K. A. (1957). Correlation Energy of an Electron Gas at High Density. **Physical Review** 106: 364.
- Guo, J. and Nordgren, J. (2000). Resonant C K α X-ray emission of some carbon allotropes and organic compounds. **Journal of Electron Spectroscopy and Related Phenomena** 110–111: 105.
- Guo, J., Skytt, P., Wassdahl, N., Nordgren, J., Luo, Y., Vahtras, O. and Ågren, H. (1995). Resonant and non-resonant X-ray scattering from C₇₀. **Chemical Physics Letters** 235: 152.
- Guo, J. H., Glans, P., Skytt, P., Wassdahl, N., Nordgren, J., Luo, Y., Ågren, H., Ma, Y., Warwick, T., Heimann, P., Rotenberg, E. and Denlinger, J. D. (1995). Resonant excitation x-ray fluorescence from C₆₀. **Physical Review B** 52: 10681.
- Hamann, D. R., Schlüter, M. and Chiang, C. (1979). Norm-Conserving Pseudopotentials. **Physical Review Letters** 43: 1494.
- Han, M. Y., Özyilmaz, B., Zhang, Y. and Kim, P. (2007). Energy Band-Gap Engineering of Graphene Nanoribbons. **Physical Review Letters** 98: 206805.
- Hedin, L. (1965). New Method for Calculating the One-Particle Green's Function with Application to the Electron-Gas Problem. **Physical Review** 139: A796.
- Hedin L, L. S. (1969). **Solid State Physics** 23. ed. Ehrenreich, H., Seitz, F. and Turnbull, D. New York: Academic.
- Hohenberg, P. and Kohn, W. (1964). Inhomogeneous Electron Gas. **Phys. Rev.** 136: B864.
- Als-Nielsen, D. M. (2001). **Elements of Modern X-ray Physics**. Chichester. Wiley.

- Wu, W. W., Yu, K. M., Ager, J. W., Haller, E. E., Hai Lu, Schaff, W. J., Saito, Y. and Nanishi, Y. (2002). Unusual properties of the fundamental band gap of InN **Applied Physics Letters** 80.
- Jarlborg, T. and Arbmán, G. (1976). The LMTO band method applied to V 3 Ga. **Journal of Physics F: Metal Physics** 6: 189.
- Jarlborg, T. and Arbmán, G. (1977). The electronic structure of some A15 compounds by semiself-consistent band calculations. **Journal of Physics F: Metal Physics** 7: 1635.
- Johnson, D. D. (1988). Modified Broyden's method for accelerating convergence in self-consistent calculations. **Physical Review B** 38: 12807.
- Jones, R. O. and Gunnarsson, O. (1989). The density functional formalism, its applications and prospects. **Reviews of Modern Physics** 61: 689.
- José, M. S., Emilio, A., Julian, D. G., Alberto, G., Javier, J., Pablo, O. and Daniel, S.-P. (2002). The SIESTA method for ab initio order- N materials simulation. **Journal of Physics: Condensed Matter** 14: 2745.
- Khalyavin, D. D., Salak, A. N., Vyshatko, N. P., Lopes, A. B., Olekhnovich, N. M., Pushkarev, A. V., Maroz, I. I. and Radyush, Y. V. (2006). Crystal Structure of Metastable Perovskite $\text{Bi}(\text{Mg}_{1/2}\text{Ti}_{1/2})\text{O}_3$: Bi-Based Structural Analogue of Antiferroelectric PbZrO_3 . **Chemistry of Materials** 18: 5104.
- King-Smith, R. D., Payne, M. C. and Lin, J. S. (1991). Real-space implementation of nonlocal pseudopotentials for first-principles total-energy calculations. **Physical Review B** 44: 13063.
- Kleinman, L. and Bylander, D. M. (1982). Efficacious Form for Model Pseudopotentials. **Physical Review Letters** 48: 1425.
- Kohn, W. and Sham, L. J. (1965). Self-Consistent Equations Including Exchange and Correlation Effects. **Physical Review** 140: A1133.

- Kotani, A. and Shin, S. (2001). Resonant inelastic x-ray scattering spectra for electrons in solids. **Reviews of Modern Physics** 73: 203.
- Kotani, T. and van Schilfgaarde, M. (2010). Fusion of the LAPW and LMTO methods: The augmented plane wave plus muffin-tin orbital method. **Physical Review B** 81: 125117.
- Kotani, T., van Schilfgaarde, M. and Faleev, S. V. (2007). Quasiparticle self-consistent GW method: A basis for the independent-particle approximation. **Physical Review B** 76: 165106.
- Kresse, G. and Furthmüller, J. (1996). Efficient iterative schemes for ab initio total-energy calculations using a plane-wave basis set. **Physical Review B** 54: 11169.
- Kresse, G. and Hafner, J. (1994). *Ab initio* molecular-dynamics simulation of the liquid-metal amorphous-semiconductor transition in germanium. **Physical Review B** 49: 14251.
- Kresse, G. and Hafner, J. (1994). Norm-conserving and ultrasoft pseudopotentials for first-row and transition elements. **Journal of Physics: Condensed Matter** 6: 8245.
- Kresse, G., Marsman, M. and Furthmüller, J. (2014). VASP the GUIDE.
- Lee, C., Wei, X., Kysar, J. W. and Hone, J. (2008). Measurement of the Elastic Properties and Intrinsic Strength of Monolayer Graphene. **Science** 321: 385.
- Li, X., Cai, W., An, J., Kim, S., Nah, J., Yang, D., Piner, R., Velamakanni, A., Jung, I., Tutuc, E., Banerjee, S. K., Colombo, L. and Ruoff, R. S. (2009). Large-Area Synthesis of High-Quality and Uniform Graphene Films on Copper Foils. **Science** 324: 1312.
- Limpijumnong, S., Smith, M. F. and Zhang, S. B. (2006). Characterization of As-doped, p-type ZnO by x-ray absorption near-edge structure spectroscopy: Theory. **Applied Physics Letters** 89: 222113.

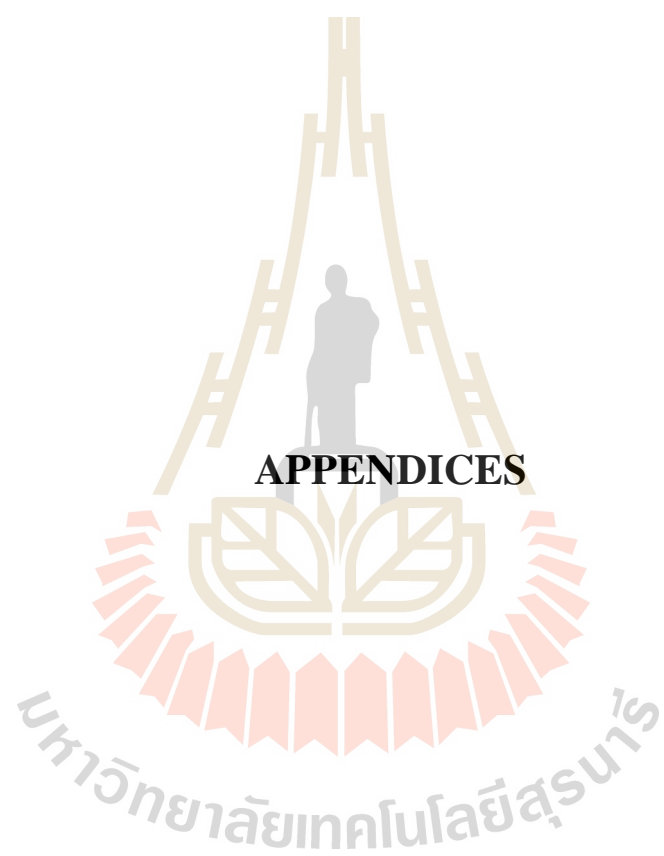
- Liu, C. and Li, J. (2011). The explanation of InN bandgap discrepancy based on experiments and first-principle calculations. **Physics Letters A** 375: 1152.
- Lloyd, P. and Smith, P. V. (1972). Multiple scattering theory in condensed materials. **Advances in Physics** 21: 69.
- Lüning, J., Rubensson, J. E., Ellmers, C., Eisebitt, S. and Eberhardt, W. (1997). Site- and symmetry-projected band structure measured by resonant inelastic soft x-ray scattering. **Physical Review B** 56: 13147.
- M. Methfessel, M. V. S., and Casali, R. A. **Electronic Structure and Physical Properties of Solids: The Use of the LMTO Method**. Springer-Verlag, Berlin.
- Ma, Y., Skytt, P., Wassdahl, N., Glans, P., Guo, J. and Nordgren, J. (1993). Core excitons and vibronic coupling in diamond and graphite. **Physical Review Letters** 71: 3725.
- Ma, Y., Wassdahl, N., Skytt, P., Guo, J., Nordgren, J., Johnson, P. D., Rubensson, J. E., Boske, T., Eberhardt, W. and Kevan, S. D. (1992). Soft-x-ray resonant inelastic scattering at the C \textit{K} edge of diamond. **Physical Review Letters** 69: 2598.
- Methfessel, M., van Schilfgaarde, M. and Casali, R. A. (2000). A Full-Potential LMTO Method Based on Smooth Hankel Functions. **Electronic Structure and Physical Properties of Solids: The Uses of the LMTO Method Lectures of a Workshop Held at Mont Saint Odile, France, October 2–5,1998**. Dreyssé, H. Berlin, Heidelberg, Springer Berlin Heidelberg: 114.
- Miyano, K. E., Ederer, D. L., Callcott, T. A., O'Brien, W. L., Jia, J. J., Zhou, L., Dong, Q. Y., Ma, Y., Woicik, J. C. and Mueller, D. R. (1993). Band-structure effects in the excitation-energy dependence of Si resonant x-ray-emission spectra. **Physical Review B** 48: 1918.
- Monkhorst, H. J. and Pack, J. D. (1976). Special points for Brillouin-zone integrations. **Physical Review B** 13: 5188.

- Moscovici, J., Loupiau, G., Parent, P. and Tourillon, G. (1996). Polarization-dependent boron and nitrogen K NEXAFS of hexagonal BN. **Journal of Physics and Chemistry of Solids** 57: 1159.
- Motlan, Goldys, E. M. and Tansley, T. L. (2002). Optical and electrical properties of InN grown by radio-frequency reactive sputtering. **Journal of Crystal Growth** 241: 165.
- Mustre de Leon, J., Rehr, J. J., Zabinsky, S. I. and Albers, R. C. (1991). Ab initio curved-wave x-ray-absorption fine structure. **Physical Review B** 44: 4146.
- Nilsson, A. and Pettersson, L. G. M. (2004). Chemical bonding on surfaces probed by X-ray emission spectroscopy and density functional theory. **Surface Science Reports** 55: 49.
- Nordgren, J., Bray, G., Cramm, S., Nyholm, R., Rubensson, J. E. and Wassdahl, N. (1989). Soft-X-Ray Emission-Spectroscopy Using Monochromatized Synchrotron Radiation. **Review of Scientific Instruments** 60: 1690.
- Novoselov, K. S., Geim, A. K., Morozov, S. V., Jiang, D., Zhang, Y., Dubonos, S. V., Grigorieva, I. V. and Firsov, A. A. (2004). Electric Field Effect in Atomically Thin Carbon Films. **Science** 306: 666.
- Perdew, J. P., Burke, K. and Ernzerhof, M. (1996). Generalized Gradient Approximation Made Simple. **Physical Review Letters** 77: 3865.
- Perdew, J. P. and Zunger, A. (1981). Self-interaction correction to density-functional approximations for many-electron systems. **Physical Review B** 23: 5048.
- Peter Blaha, K. S., Georg Madsen, Dieter Kvasnicka, Joachim Luitz. (2014). User's Guide WIEN2k 14.2, Vienna University of Technology.
- Piper, L. F. J., Colakerol, L., Learmonth, T., Glans, P.-A., Smith, K. E., Fuchs, F., Furthmüller, J., Bechstedt, F., Chen, T.-C., Moustakas, T. D. and Guo, J. H. (2007). Electronic structure of InN studied using soft x-ray emission, soft x-ray absorption, and quasiparticle band structure calculations. **Physical Review B** 76: 245204.

- Preston, A. R. H., DeMasi, A., Piper, L. F. J., Smith, K. E., Lambrecht, W. R. L., Boonchun, A., Cheiwchanchamnangij, T., Arnemann, J., van Schilfgaarde, M. and Ruck, B. J. (2011). First-principles calculation of resonant x-ray emission spectra applied to ZnO. **Physical Review B** 83: 205106.
- Preston, A. R. H., Ruck, B. J., Piper, L. F. J., DeMasi, A., Smith, K. E., Schleife, A., Fuchs, F., Bechstedt, F., Chai, J. and Durbin, S. M. (2008). Band structure of ZnO from resonant x-ray emission spectroscopy. **Physical Review B** 78: 155114.
- Pulay, P. (1980). Convergence acceleration of iterative sequences. the case of scf iteration. **Chemical Physics Letters** 73: 393-398.
- Ravel, B. (2005). A practical introduction to multiple scattering theory. **Journal of Alloys and compounds** 401: 118.
- Rehr, J. J. and Albers, R. C. (1990). Scattering-matrix formulation of curved-wave multiple-scattering theory: Application to x-ray-absorption fine structure. **Physical Review B** 41: 8139.
- Rehr, J. J. and Albers, R. C. (2000). Theoretical approaches to x-ray absorption fine structure. **Reviews of Modern Physics** 72: 621.
- Rubensson, J. E., Mueller, D., Shuker, R., Ederer, D. L., Zhang, C. H., Jia, J. and Callcott, T. A. (1990). Excitation-energy dependence in the L_{2,3} fluorescence spectrum of Si. **Physical Review Letters** 64: 1047.
- Eisebitt, W. E. (2000). Band structure information and resonant inelastic soft X-ray scattering in broad band solids. **Soft X Ray Emission Spectroscopy** 110-111: 335.
- Kelly, S. D., Ravel, B. (2008). Analysis of soils and minerals using X-ray absorption spectroscopy. **Soil Science Society of America**. Madison.
- Schnohr, C. S. and Ridgway, M. C. (2015). **X-Ray Absorption Spectroscopy of Semiconductors**. Berlin Heidelberg. Springer-Verlag.

- Schwertfager, N., Pandech, N., Suewattana, M., T-thienprasert, J. and Limpijumnong, S. (2016). Calculated XANES Spectra of Cation Off-Centering in $\text{Bi}(\text{Mg}_{0.5}\text{Ti}_{0.5})\text{O}_3$. **Ferroelectrics** 490: 159.
- Seitz, F. (1969). **Solid State Physics: Advances in Research and Applications**. Academic Press.
- Shirley, E. L. (2000). Theory and simulation of resonant inelastic X-ray scattering in s-p bonded systems: graphite, hexagonal boron nitride, diamond, and cubic boron nitride. **Journal of Electron Spectroscopy and Related Phenomena** 110–111: 305.
- Skytt, P., Glans, P., Mancini, D. C., Guo, J. H., Wassdahl, N., Nordgren, J. and Ma, Y. (1994). Angle-resolved soft-x-ray fluorescence and absorption study of graphite. **Physical Review B** 50: 10457.
- Sokolov, A. V., Kurmaev, E. Z., Leitch, S., Moewes, A., Kortus, J., Finkelstein, L. D., Skorikov, N. A., Xiao, C. and Hirose, A. (2003). Band dispersion of MgB_2 , graphite and diamond from resonant inelastic scattering. **Journal of Physics: Condensed Matter** 15: 2081.
- Stampfl, C. and Van de Walle, C. G. (1998). Energetics and electronic structure of stacking faults in AlN, GaN, and InN. **Physical Review B** 57: R15052.
- Suewattana, M., Singh, D. J. and Limpijumnong, S. (2012). Erratum: Crystal structure and cation off-centering in $\text{Bi}(\text{Mg}_{0.5}\text{Ti}_{0.5})\text{O}_3$. **Physical Review B** 86: 219903.
- Takashi Matsuoka, H. O., Masashi Nakao, Hiroshi Harima and Eiji Kurimoto. (2002). Optical bandgap energy of wurtzite InN **Applied Physics Letters** 81.
- Teter, M. P., Payne, M. C. and Allan, D. C. (1989). Solution of Schrödinger's equation for large systems. **Physical Review B** 40: 12255.
- Thompson, A. and Vaughan, D., Eds. (2001). **Center for x-ray optics and advanced light source X-ray data handbook**. Berkeley, California.

- van Schilfgaarde, M., Kotani, T. and Faleev, S. (2006). Quasiparticle Self-Consistent GW Theory. **Physical Review Letters** 96: 226402.
- van Schilfgaarde, M., Kotani, T. and Faleev, S. V. (2006). Adequacy of approximations in QSGW theory. **Physical Review B** 74: 245125.
- Vedrinskii, R. V., Kraizman, V. L., Novakovich, A. A., Ph, V. D. and Urazhdin, S. V. (1998). Pre-edge fine structure of the 3d atom K x-ray absorption spectra and quantitative atomic structure determinations for ferroelectric perovskite structure crystals. **Journal of Physics: Condensed Matter** 10: 9561.
- Wei, S.-H., Nie, X., Batyrev, I. G. and Zhang, S. B. (2003). Breakdown of the band-gap-common-cation rule: The origin of the small band gap of InN. **Physical Review B** 67: 165209.
- Westra, K. L. and Brett, M. J. (1990). Near IR optical properties of sputtered InN films. **Thin Solid Films** 192: 227.
- Wigner, E. (1934). On the Interaction of Electrons in Metals. **Physical Review** 46: 1002.
- Wood, D. M. and Zunger, A. (1985). A new method for diagonalising large matrices. **Journal of Physics A: Mathematical and General** 18: 1343.
- Zhang, L., Schwertfager, N., Cheiwchanchamnangij, T., Lin, X., Glans-Suzuki, P. A., Piper, L. F. J., Limpijumnong, S., Luo, Y., Zhu, J. F., Lambrecht, W. R. L. and Guo, J. H. (2012). Electronic band structure of graphene from resonant soft x-ray spectroscopy: The role of core-hole effects. **Physical Review B** 86: 245430.



APPENDICES

APPENDIX A

PUBLICATIONS

1. A Publication in Physical Review B: Impact Factor 3.718

PHYSICAL REVIEW B **86**, 245430 (2012)

Electronic band structure of graphene from resonant soft x-ray spectroscopy: The role of core-hole effects

L. Zhang,^{1,2} N. Schwertfager,^{3,4} T. Cheiwchanchamnangij,³ X. Lin,^{2,5} P.-A. Glans-Suzuki,² L. F. J. Piper,⁶ S. Limpijumnong,⁴

Y. Luo,^{5,7} J. F. Zhu,^{1,4} W. R. L. Lambrecht,^{3,7} and J.-H. Guo^{2,7}

¹*National Synchrotron Radiation Laboratory, University of Science and Technology of China, Hefei 230029, China*

²*Advanced Light Source, Lawrence Berkeley National Laboratory, Berkeley, California 94720, USA*

³*Department of Physics, Case Western Reserve University, Cleveland, Ohio 44106-7079, USA*

⁴*School of Physics, Suranaree University of Technology, Nakhon Ratchasima 30000, Thailand*

⁵*Division of Theoretical Chemistry and Biology, School of Biotechnology, Royal Institute of Technology, S-106 91 Stockholm, Sweden*

⁶*Department of Physics, Applied Physics and Astronomy, Binghamton University, Binghamton, New York 13902, USA*

⁷*Hefei National Laboratory for Physical Science at the Microscale, University of Science and Technology of China, Hefei 230029, China*

(Received 24 July 2012; revised manuscript received 7 November 2012; published 26 December 2012)

The electronic structure and band dispersion of graphene on SiO₂ have been studied by x-ray-absorption spectroscopy (XAS), x-ray-emission spectroscopy (XES), and resonant inelastic x-ray scattering (RIXS). Using first-principles calculations, it is found that the core-hole effect is dramatic in XAS while it has negligible consequences in XES. Strong dispersive features, due to the conservation of crystal momentum, are observed in RIXS spectra. Simulated RIXS spectra based on the Kramers-Heisenberg theory agree well with the experimental results, provided a shift between RIXS and XAS due to the absence or presence of the core hole is taken into account.

DOI: [10.1103/PhysRevB.86.245430](https://doi.org/10.1103/PhysRevB.86.245430) PACS number(s): 73.22.Pr, 71.10.Li, 78.70.Dm, 78.70.En

2. A Publication in Ferroelectrics: Impact Factor 0.53

Calculated XANES Spectra of Cation Off-Centering in $\text{Bi}(\text{Mg}_{0.5}\text{Ti}_{0.5})\text{O}_3$

NUCHALEE SCHWERTFAGER^{1,2,3,*}, NARASAK PANDECH^{1,2,3}
MALLIGA SUEWATTANA⁴, JIRAROJ T-THIENPRASERT⁵,
AND SUKIT LIMPIJUMNONG^{1,2,3}

¹School of Physics and NANOTEC-SUT Center of Excellence on Advanced
Functional Nanomaterials, Suranaree University of Technology, Nakhon
Ratchasima 30000, Thailand

²Synchrotron Light Research Institute, Nakhon Ratchasima 30000, Thailand

³Thailand Center of Excellence in Physics (ThEP Center), Commission on
Higher Education, Bangkok 10400, Thailand

⁴Department of Physics, Faculty of Science, Mahidol University, Bangkok
10400, Thailand

⁵Department of Physics, Kasetsart University, Bangkok 10900, Thailand

The x-ray absorption near edge spectra (XANES) of Bi, Mg and Ti in BMT for different off-centering magnitudes, associated with different structural models, were calculated by using first-principles calculations. The models studied include the high symmetric structure, two experimental proposed structures (based on an x-ray diffraction experiment) and the calculated fully relaxed structure (based on the calculated energy optimization). The features in the XANES spectra that relates with the off-center shift of cations were identified. Our calculated XANES will aid future experimental identifications of the detailed structure of BMT.

Keywords X-ray absorption spectroscopy; off-centering; first principles calculations

มหาวิทยาลัยเทคโนโลยีสุรนารี

APPENDIX B

PRESENTATIONS

1. Oral Presentations:

- “*Why N Cannot Lead to P-Type Conductivity in ZnO?*”, Suranaree University of Technology, Thailand (*Awarded the Best Speaker of the Seminar Class of 2009*)
- “*First Principles Calculation of Resonant X-Ray Emission Spectra of Graphite*”, The 7th Annual Conference of the Thai Physics Society, Ayutthaya, Thailand
- “*Calculated x-ray absorption spectra of cation-off centering in $Bi(Ti_{1/2}Mg_{1/2})O_3$* ”, 8th ASEAN Meeting on Ferroelectric, Pattaya, Thailand

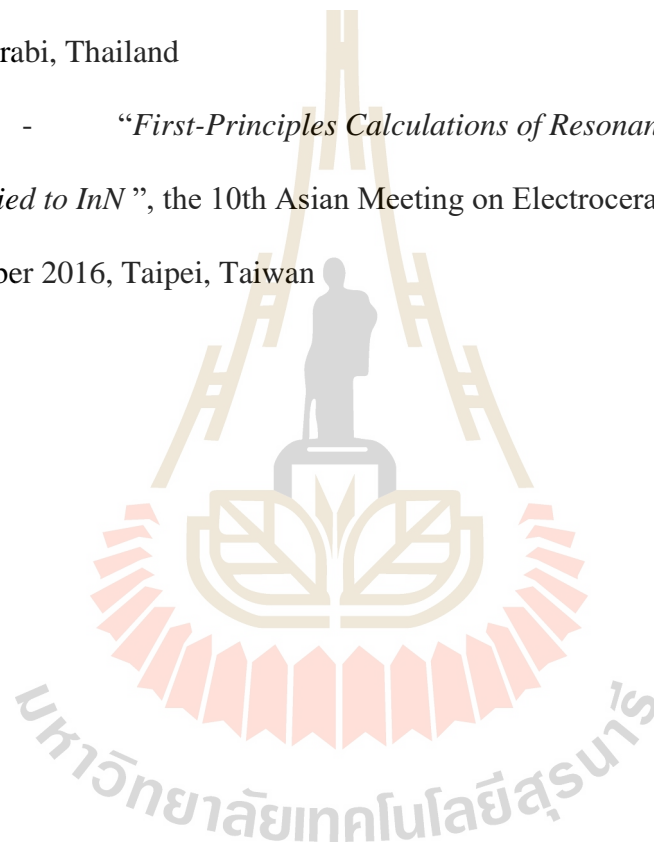
2. Poster Presentations:

- “*Electronic band-structure of InN by quasiparticle self-consistent GW approach*”, Siam Physics Congress, Chiangmai, Thailand
- “*Calculated XANES spectra of cation off-centering in $Bi(Ti_{1/2}Mg_{1/2})O_3$: First-Principles Calculation*”, The 3rd Academic Conference on Natural Science for Natural Science for Master and PhD students from ASEAN Countries, Pnom Pehn, Cambodia

- “*Calculated XANES Spectra of Cation Off-Centering in $\text{Bi}(\text{Mg}_{0.5}\text{Ti}_{0.5})\text{O}_3$* ”, 9th Asian Meeting on Ferroelectricity (AMF-9) and the 9th Asian Meeting on Electroceramics (AMEC-9), 26 - 30 October 2014, Shanghai, China

- “*The Role of Core Hole Effects on Calculated Resonant Inelastic X-Ray Scattering Spectra of Graphene*”, Siam Physics Congress, 20 – 22 May 2015, Krabi, Thailand

- “*First-Principles Calculations of Resonant X-Ray Emission Spectra Applied to InN* ”, the 10th Asian Meeting on Electroceramics (AMEC 10), 3 – 8 December 2016, Taipei, Taiwan



CURRICULUM VITAE

Name: Nuchalee Schwertfager

Date of Birth: 12 October 1982

Place of Birth: Bangkok, Thailand

Education:

- Jun 2009 – Mar 2017 *Ph.D. in Physics*, GPA: 3.93/4.00

Suranaree University of Technology, Thailand (Royal Golden Jubilee Scholarship)

- Jun 2004 – Mar 2005 *Grad. Dip. of Teaching Profession*

in **Mathematics and Sciences**, Srinakharinwirot University, Thailand

- Jun 2000 – Mar 2004 *B.Sc. (1st Honors) in Physics*, GPA: 3.63/4.00

Srinakharinwirot University, Thailand

Publications:

- L Zhang, N Schwertfager, T Cheiwchanchamnangij, X Lin, et al., Electronic band structure of graphene from resonant soft x-ray spectroscopy: The role of core - hole effects, *Physical Review B* 86 (24), 245430, 2012

- N Schwertfager, N. Pandech, M Suewattana, S T-Thienprasert and S Limpijumnong, Calculated XANES Spectra of Cation Off-Centering in $\text{Bi}(\text{Mg}_{0.5}\text{Ti}_{0.5})\text{O}_3$, *Ferroelectrics* (490), 159-166, 2016

Research Fellowship:

- Apr – Oct 2011 Department of Physics, Case Western Reserve University, Ohio, USA

Awards and Honors:

- Representative of Thailand to join a Nobel Laureates Meeting in Physics, 7 – 14 July 2012, Lindau, Germany

REFERENCES

- Ahmed, R., Akbarzadeh, H. and Fazal e, A. (2005). A first principle study of band structure of III-nitride compounds. **Physica B: Condensed Matter** 370: 52.
- Ankudinov, A. L., Bouldin, C. E., Rehr, J. J., Sims, J. and Hung, H. (2002). Parallel calculation of electron multiple scattering using Lanczos algorithms. **Physical Review B** 65.
- Ankudinov, A. L., Ravel, B., Rehr, J. J. and Conradson, S. D. (1998). Real-space multiple-scattering calculation and interpretation of x-ray-absorption near-edge structure. **Physical Review B** 58: 7565.
- Aryasetiawan, F. and Gunnarsson, O. (1998). The GW method. **Reports on Progress in Physics** 61: 237.
- Beeby, J. L. (1967). The Density of Electrons in a Perfect or Imperfect Lattice. **Proceedings of the Royal Society of London. Series A, Mathematical and Physical Sciences** 302: 113.
- Berger, C., Song, Z., Li, X., Wu, X., Brown, N., Naud, C., Mayou, D., Li, T., Hass, J., Marchenkov, A. N., Conrad, E. H., First, P. N. and de Heer, W. A. (2006). Electronic Confinement and Coherence in Patterned Epitaxial Graphene. **Science** 312: 1191.
- Bott, E., Methfessel, M., Krabs, W. and Schmidt, P. C. (1998). Nonsingular Hankel functions as a new basis for electronic structure calculations. **Journal of Mathematical Physics** 39: 3393.

- Brühwiler, P. A., Kuiper, P., Eriksson, O., Ahuja, R. and Svensson, S. (1996). Core Hole Effects in Resonant Inelastic X-Ray Scattering of Graphite. **Physical Review Letters** 76: 1761.
- Brühwiler, P. A., Maxwell, A. J., Puglia, C., Nilsson, A., Andersson, S. and Mårtensson, N. (1995). Absorption of Graphite. **Physical Review Letters** 74: 614.
- Bylander, D. M., Kleinman, L. and Lee, S. (1990). Self-consistent calculations of the energy bands and bonding properties of $B_{12}C_3$. **Physical Review B** 42: 1394.
- Carlisle, J. A., Shirley, E. L., Hudson, E. A., Terminello, L. J., Callcott, T. A., Jia, J. J., Ederer, D. L., Perera, R. C. C. and Himpsel, F. J. (1995). Probing the Graphite Band Structure with Resonant Soft-X-Ray Fluorescence. **Physical Review Letters** 74: 1234.
- Carlisle, J. A., Shirley, E. L., Hudson, E. A., Terminello, L. J., Callcott, T. A., Jia, J. J., Ederer, D. L., Perera, R. C. C. and Himpsel, F. J. (1996). Carlisle \textit{et al.} Reply. **Physical Review Letters** 76: 1762.
- Cowan, R. D. (1981). **The Theory of Atomic Structure and Spectra**. California. University of California Press Books.
- Davydov, V. Y., Klochikhin, A. A., Emtsev, V. V., Ivanov, S. V., Vekshin, V. V., Bechstedt, F., Furthmüller, J., Harima, H., Mudryi, A. V., Hashimoto, A., Yamamoto, A., Aderhold, J., Graul, J. and Haller, E. E. (2002). Band gap of InN and In-rich $In_xGa_{1-x}N$ alloys ($0.36 < x < 1$). **physica status solidi (b)** 230: R4.
- Davydov, V. Y., Klochikhin, A. A., Seisyan, R. P., Emtsev, V. V., Ivanov, S. V., Bechstedt, F., Furthmüller, J., Harima, H., Mudryi, A. V., Aderhold, J., Semchinova, O. and Graul, J. (2002). Absorption and Emission of Hexagonal InN. Evidence of Narrow Fundamental Band Gap. **physica status solidi (b)** 229: r1.

- Dedkov, Y. S., Fonin, M., Rüdiger, U. and Laubschat, C. (2008). Rashba Effect in the Graphene/Ni(111) System. **Physical Review Letters** 100: 107602.
- Foley, C. P. and Tansley, T. L. (1986). Pseudopotential band structure of indium nitride. **Physical Review B** 33: 1430.
- Fongkaew, I., T-Thienprasert, J., Singh, D. J., Du, M. H. and Limpijumnong, S. (2013). First principles calculations of Hydrogen—Titanium vacancy complexes in SrTiO₃. **Ceramics International** 39, Supplement 1: S273.
- Gell-Mann, M. and Brueckner, K. A. (1957). Correlation Energy of an Electron Gas at High Density. **Physical Review** 106: 364.
- Guo, J. and Nordgren, J. (2000). Resonant C K α X-ray emission of some carbon allotropes and organic compounds. **Journal of Electron Spectroscopy and Related Phenomena** 110–111: 105.
- Guo, J., Skytt, P., Wassdahl, N., Nordgren, J., Luo, Y., Vahtras, O. and Ågren, H. (1995). Resonant and non-resonant X-ray scattering from C₇₀. **Chemical Physics Letters** 235: 152.
- Guo, J. H., Glans, P., Skytt, P., Wassdahl, N., Nordgren, J., Luo, Y., Ågren, H., Ma, Y., Warwick, T., Heimann, P., Rotenberg, E. and Denlinger, J. D. (1995). Resonant excitation x-ray fluorescence from C₆₀. **Physical Review B** 52: 10681.
- Hamann, D. R., Schlüter, M. and Chiang, C. (1979). Norm-Conserving Pseudopotentials. **Physical Review Letters** 43: 1494.
- Han, M. Y., Özyilmaz, B., Zhang, Y. and Kim, P. (2007). Energy Band-Gap Engineering of Graphene Nanoribbons. **Physical Review Letters** 98: 206805.
- Hedin, L. (1965). New Method for Calculating the One-Particle Green's Function with Application to the Electron-Gas Problem. **Physical Review** 139: A796.

- Hedin L, L. S. (1969). **Solid State Physics** 23. ed. Ehrenreich, H., Seitz, F. and Turnbull, D. New York: Academic.
- Hohenberg, P. and Kohn, W. (1964). Inhomogeneous Electron Gas. **Phys. Rev.** 136: B864.
- J. Als-Nielsen, D. M. (2001). **Elements of Modern X-ray Physics**. Chichester. Wiley.
- J. Wu, W. W., K. M. Yu, J. W. Ager III, E. E. Haller, Hai Lu, William J. Schaff, Yoshiki Saito and Yasushi Nanishi (2002). Unusual properties of the fundamental band gap of InN **Applied Physics Letters** 80.
- Jarlborg, T. and Arbman, G. (1976). The LMTO band method applied to V 3 Ga. **Journal of Physics F: Metal Physics** 6: 189.
- Jarlborg, T. and Arbman, G. (1977). The electronic structure of some A15 compounds by semiself-consistent band calculations. **Journal of Physics F: Metal Physics** 7: 1635.
- Johnson, D. D. (1988). Modified Broyden's method for accelerating convergence in self-consistent calculations. **Physical Review B** 38: 12807.
- Jones, R. O. and Gunnarsson, O. (1989). The density functional formalism, its applications and prospects. **Reviews of Modern Physics** 61: 689.
- José, M. S., Emilio, A., Julian, D. G., Alberto, G., Javier, J., Pablo, O. and Daniel, S.-P. (2002). The SIESTA method for ab initio order- N materials simulation. **Journal of Physics: Condensed Matter** 14: 2745.
- Khalyavin, D. D., Salak, A. N., Vyshatko, N. P., Lopes, A. B., Olekhovich, N. M., Pushkarev, A. V., Maroz, I. I. and Radyush, Y. V. (2006). Crystal Structure of Metastable Perovskite $\text{Bi}(\text{Mg}_{1/2}\text{Ti}_{1/2})\text{O}_3$: Bi-Based Structural Analogue of Antiferroelectric PbZrO_3 . **Chemistry of Materials** 18: 5104.

- King-Smith, R. D., Payne, M. C. and Lin, J. S. (1991). Real-space implementation of nonlocal pseudopotentials for first-principles total-energy calculations. **Physical Review B** 44: 13063.
- Kleinman, L. and Bylander, D. M. (1982). Efficacious Form for Model Pseudopotentials. **Physical Review Letters** 48: 1425.
- Kohn, W. and Sham, L. J. (1965). Self-Consistent Equations Including Exchange and Correlation Effects. **Phys. Rev.** 140: A1133.
- Kotani, A. and Shin, S. (2001). Resonant inelastic x-ray scattering spectra for electrons in solids. **Reviews of Modern Physics** 73: 203.
- Kotani, T. and van Schilfgaarde, M. (2010). Fusion of the LAPW and LMTO methods: The augmented plane wave plus muffin-tin orbital method. **Physical Review B** 81: 125117.
- Kotani, T., van Schilfgaarde, M. and Faleev, S. V. (2007). Quasiparticle self-consistent GW method: A basis for the independent-particle approximation. **Physical Review B** 76: 165106.
- Kresse, G. and Furthmüller, J. (1996). Efficient iterative schemes for $\textit{ab initio}$ total-energy calculations using a plane-wave basis set. **Physical Review B** 54: 11169.
- Kresse, G. and Hafner, J. (1994). *Ab initio* molecular-dynamics simulation of the liquid-metal amorphous-semiconductor transition in germanium. **Physical Review B** 49: 14251.
- Kresse, G. and Hafner, J. (1994). Norm-conserving and ultrasoft pseudopotentials for first-row and transition elements. **Journal of Physics: Condensed Matter** 6: 8245.
- Kresse, G., Marsman, M. and Furthmüller, J. (2014). VASP the GUIDE.

- Lee, C., Wei, X., Kysar, J. W. and Hone, J. (2008). Measurement of the Elastic Properties and Intrinsic Strength of Monolayer Graphene. **Science** 321: 385.
- Li, X., Cai, W., An, J., Kim, S., Nah, J., Yang, D., Piner, R., Velamakanni, A., Jung, I., Tutuc, E., Banerjee, S. K., Colombo, L. and Ruoff, R. S. (2009). Large-Area Synthesis of High-Quality and Uniform Graphene Films on Copper Foils. **Science** 324: 1312.
- Limpijumnong, S., Smith, M. F. and Zhang, S. B. (2006). Characterization of As-doped, p-type ZnO by x-ray absorption near-edge structure spectroscopy: Theory. **Applied Physics Letters** 89: 222113.
- Liu, C. and Li, J. (2011). The explanation of InN bandgap discrepancy based on experiments and first-principle calculations. **Physics Letters A** 375: 1152.
- Lloyd, P. and Smith, P. V. (1972). Multiple scattering theory in condensed materials. **Advances in Physics** 21: 69.
- Lüning, J., Rubensson, J. E., Ellmers, C., Eisebitt, S. and Eberhardt, W. (1997). Site- and symmetry-projected band structure measured by resonant inelastic soft x-ray scattering. **Physical Review B** 56: 13147.
- M. Methfessel, M. V. S., and R. A. Casali. **Electronic Structure and Physical Properties of Solids: The Use of the LMTO Method**. Springer-Verlag, Berlin.
- Ma, Y., Skytt, P., Wassdahl, N., Glans, P., Guo, J. and Nordgren, J. (1993). Core excitons and vibronic coupling in diamond and graphite. **Physical Review Letters** 71: 3725.
- Ma, Y., Wassdahl, N., Skytt, P., Guo, J., Nordgren, J., Johnson, P. D., Rubensson, J. E., Boske, T., Eberhardt, W. and Kevan, S. D. (1992). Soft-x-ray resonant inelastic scattering at the C \textit{K} edge of diamond. **Physical Review Letters** 69: 2598.

- Methfessel, M., van Schilfgaarde, M. and Casali, R. A. (2000). A Full-Potential LMTO Method Based on Smooth Hankel Functions. **Electronic Structure and Physical Properties of Solids: The Uses of the LMTO Method Lectures of a Workshop Held at Mont Saint Odile, France, October 2–5,1998**. Dreyssé, H. Berlin, Heidelberg, Springer Berlin Heidelberg: 114.
- Miyano, K. E., Ederer, D. L., Callcott, T. A., O'Brien, W. L., Jia, J. J., Zhou, L., Dong, Q. Y., Ma, Y., Woicik, J. C. and Mueller, D. R. (1993). Band-structure effects in the excitation-energy dependence of Si resonant x-ray-emission spectra. **Physical Review B** 48: 1918.
- Monkhorst, H. J. and Pack, J. D. (1976). Special points for Brillouin-zone integrations. **Physical Review B** 13: 5188.
- Moscovici, J., Loupiaz, G., Parent, P. and Tourillon, G. (1996). Polarization-dependent boron and nitrogen K NEXAFS of hexagonal BN. **Journal of Physics and Chemistry of Solids** 57: 1159.
- Motlan, Goldys, E. M. and Tansley, T. L. (2002). Optical and electrical properties of InN grown by radio-frequency reactive sputtering. **Journal of Crystal Growth** 241: 165.
- Mustre de Leon, J., Rehr, J. J., Zabinsky, S. I. and Albers, R. C. (1991). Ab initio curved-wave x-ray-absorption fine structure. **Physical Review B** 44: 4146.
- Nilsson, A. and Pettersson, L. G. M. (2004). Chemical bonding on surfaces probed by X-ray emission spectroscopy and density functional theory. **Surface Science Reports** 55: 49.

- Nordgren, J., Bray, G., Cramm, S., Nyholm, R., Rubensson, J. E. and Wassdahl, N. (1989). Soft-X-Ray Emission-Spectroscopy Using Monochromatized Synchrotron Radiation. **Review of Scientific Instruments** 60: 1690.
- Novoselov, K. S., Geim, A. K., Morozov, S. V., Jiang, D., Zhang, Y., Dubonos, S. V., Grigorieva, I. V. and Firsov, A. A. (2004). Electric Field Effect in Atomically Thin Carbon Films. **Science** 306: 666.
- Perdew, J. P., Burke, K. and Ernzerhof, M. (1996). Generalized Gradient Approximation Made Simple. **Physical Review Letters** 77: 3865.
- Perdew, J. P. and Zunger, A. (1981). Self-interaction correction to density-functional approximations for many-electron systems. **Physical Review B** 23: 5048.
- Peter Blaha, K. S., Georg Madsen, Dieter Kvasnicka, Joachim Luitz. (2014). User's Guide WIEN2k 14.2, Vienna University of Technology.
- Piper, L. F. J., Colakerol, L., Learmonth, T., Glans, P.-A., Smith, K. E., Fuchs, F., Furthmüller, J., Bechstedt, F., Chen, T.-C., Moustakas, T. D. and Guo, J. H. (2007). Electronic structure of InN studied using soft x-ray emission, soft x-ray absorption, and quasiparticle band structure calculations. **Physical Review B** 76: 245204.
- Preston, A. R. H., DeMasi, A., Piper, L. F. J., Smith, K. E., Lambrecht, W. R. L., Boonchun, A., Cheiwchanchamnangij, T., Arnemann, J., van Schilfgaarde, M. and Ruck, B. J. (2011). First-principles calculation of resonant x-ray emission spectra applied to ZnO. **Physical Review B** 83: 205106.
- Preston, A. R. H., Ruck, B. J., Piper, L. F. J., DeMasi, A., Smith, K. E., Schleife, A., Fuchs, F., Bechstedt, F., Chai, J. and Durbin, S. M. (2008). Band structure of ZnO from resonant x-ray emission spectroscopy. **Physical Review B** 78: 155114.

- Pulay, P. (1980). Convergence acceleration of iterative sequences. the case of scf iteration. **Chemical Physics Letters** 73: 393-398.
- Ravel, B. (2005). A practical introduction to multiple scattering theory. **Journal of Alloys and compounds** 401: 118.
- Rehr, J. J. and Albers, R. C. (1990). Scattering-matrix formulation of curved-wave multiple-scattering theory: Application to x-ray-absorption fine structure. **Physical Review B** 41: 8139.
- Rehr, J. J. and Albers, R. C. (2000). Theoretical approaches to x-ray absorption fine structure. **Reviews of Modern Physics** 72: 621.
- Rubensson, J. E., Mueller, D., Shuker, R., Ederer, D. L., Zhang, C. H., Jia, J. and Callcott, T. A. (1990). Excitation-energy dependence in the $L_{2,3}$ fluorescence spectrum of Si. **Physical Review Letters** 64: 1047.
- S. Eisebitt, W. E. (2000). Band structure information and resonant inelastic soft X-ray scattering in broad band solids. **Soft X Ray Emission Spectroscopy** 110-111: 335.
- S.D.Kelly, D. H., B. Ravel (2008). Analysis of soils and minerals using X-ray absorption spectroscopy. **Soil Science Society of America**. Madison.
- Schnohr, C. S. and Ridgway, M. C. (2015). **X-Ray Absorption Spectroscopy of Semiconductors**. Berlin Heidelberg. Springer-Verlag.
- Schwertfager, N., Pandech, N., Suewattana, M., T-thienprasert, J. and Limpijumnong, S. (2016). Calculated XANES Spectra of Cation Off-Centering in $\text{Bi}(\text{Mg}_{0.5}\text{Ti}_{0.5})\text{O}_3$. **Ferroelectrics** 490: 159.
- Seitz, F. (1969). **Solid State Physics: Advances in Research and Applications**. Academic Press.

- Shirley, E. L. (2000). Theory and simulation of resonant inelastic X-ray scattering in s-p bonded systems: graphite, hexagonal boron nitride, diamond, and cubic boron nitride. **Journal of Electron Spectroscopy and Related Phenomena** 110–111: 305.
- Skytt, P., Glans, P., Mancini, D. C., Guo, J. H., Wassdahl, N., Nordgren, J. and Ma, Y. (1994). Angle-resolved soft-x-ray fluorescence and absorption study of graphite. **Physical Review B** 50: 10457.
- Sokolov, A. V., Kurmaev, E. Z., Leitch, S., Moewes, A., Kortus, J., Finkelstein, L. D., Skorikov, N. A., Xiao, C. and Hirose, A. (2003). Band dispersion of MgB₂, graphite and diamond from resonant inelastic scattering. **Journal of Physics: Condensed Matter** 15: 2081.
- Stampfl, C. and Van de Walle, C. G. (1998). Energetics and electronic structure of stacking faults in AlN, GaN, and InN. **Physical Review B** 57: R15052.
- Suewattana, M., Singh, D. J. and Limpijumngong, S. (2012). Erratum: Crystal structure and cation off-centering in Bi(Mg_{0.5}Ti_{0.5})O₃. **Physical Review B** 86: 219903.
- Takashi Matsuoka, H. O., Masashi Nakao, Hiroshi Harima and Eiji Kurimoto. (2002). Optical bandgap energy of wurtzite InN **Applied Physics Letters** 81.
- Teter, M. P., Payne, M. C. and Allan, D. C. (1989). Solution of Schrödinger's equation for large systems. **Physical Review B** 40: 12255.
- Thompson, A. and Vaughan, D., Eds. (2001). **Center for x-ray optics and advanced light source X-ray data handbook**. Berkeley, California.
- van Schilfgaarde, M., Kotani, T. and Faleev, S. (2006). Quasiparticle Self-Consistent GW Theory. **Physical Review Letters** 96: 226402.

- van Schilfgaarde, M., Kotani, T. and Faleev, S. V. (2006). Adequacy of approximations in QSGW theory. **Physical Review B** 74: 245125.
- Vedrinskii, R. V., Kraizman, V. L., Novakovich, A. A., Ph, V. D. and Urazhdin, S. V. (1998). Pre-edge fine structure of the 3d atom K x-ray absorption spectra and quantitative atomic structure determinations for ferroelectric perovskite structure crystals. **Journal of Physics: Condensed Matter** 10: 9561.
- Wei, S.-H., Nie, X., Batyrev, I. G. and Zhang, S. B. (2003). Breakdown of the band-gap-common-cation rule: The origin of the small band gap of InN. **Physical Review B** 67: 165209.
- Westra, K. L. and Brett, M. J. (1990). Near IR optical properties of sputtered InN films. **Thin Solid Films** 192: 227.
- Wigner, E. (1934). On the Interaction of Electrons in Metals. **Physical Review** 46: 1002.
- Wood, D. M. and Zunger, A. (1985). A new method for diagonalising large matrices. **Journal of Physics A: Mathematical and General** 18: 1343.
- Zhang, L., Schwertfager, N., Cheiwchanchamnangij, T., Lin, X., Glans-Suzuki, P. A., Piper, L. F. J., Limpijumnong, S., Luo, Y., Zhu, J. F., Lambrecht, W. R. L. and Guo, J. H. (2012). Electronic band structure of graphene from resonant soft x-ray spectroscopy: The role of core-hole effects. **Physical Review B** 86: 245430.